STUDY OF ENGINE KNOCK USING A MONTE CARLO METHOD

By

Kenneth S. Kim

A dissertation submitted in partial fulfillment of

the requirements for the degree of

Doctor of Philosophy

(Mechanical Engineering)

at the

UNIVERSITY OF WISCONSIN – MADISON

2015

Date of final oral examination: 08/17/15

The dissertation is approved by the following members of the Final Oral Committee:

Jaal B. Ghandhi, Professor, Mechanical Engineering
Ricardo Bonazza, Professor, Engineering Physics
Sage Kokjohn, Assistant Professor, Mechanical Engineering
David A. Rothamer, Associate Professor, Mechanical Engineering
William Sethares, Professor, Electrical and Computer Engineering

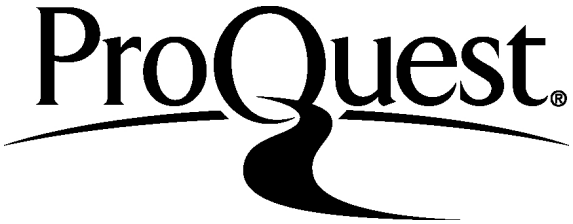

Abstract

A simple yet accurate cyclic variation and coupled knock model were developed to predict the statistical distribution of both knock onset and knock intensity. The factors controlling knock onset and knock intensity in spark ignition engine were investigated. New methods of more accurately determining the knock onset timing and heat release calculation were developed to determine accurate thermodynamic conditions at knock.

Knock onset was accurately determined using median and smoothing filters to avoid biases associated with the Butterworth low- and high-pass filter at a transient pressure increase. The noise calculated before the initial pressure rise was used to dynamically set a threshold value to determine knock onset. The new method showed more accurate determination of knock onset compared to the threshold value exceed (TVE) or signal energy ratio (SER) methods.

The most critical parameter for heat release calculations was found to be the calculation window size that limits the integration of the energy balance. Fixed, adjusted and individual window size of heat release calculation were compared using the in-cylinder pressure predicted by a thermodynamic engine model. The individual end angle determined using a Wiebe function-based method showed the most accurate results for a range of operating conditions.

A simple model to simulate cycle-by-cycle variation that is suitable for use in Monte-Carlo approaches has been developed and validated with a wide range of experimental data. Using the cumulative density function of θ_{ig}, and linear fits of θ_{comb} and m to θ_{ig}, with a random component added, a Monte-Carlo scheme was developed. The universal coefficients to determine the linear fit between Wiebe function parameters at an arbitrary condition were found and reasonable distributions were predicted from the universal cyclic variation model.

Knock onset was predicted using three models: an ignition-integral model using a simple ignition delay correlation, an ignition-integral model using a pre-computed lookup tables of ignition delays, and the direct integration of a detailed chemical kinetic mechanism. All three models were found to compare well with experimentally measured results; the correlation knock-integral model was found to be as accurate as the other methods and was computationally far more efficient. It was proved that the measured knock intensity values does not depend only on the thermodynamic conditions at knock onset that cycles with similar in-cylinder pressure development showed large differences in measured maximum amplitude of pressure oscillation (MAPO) values. A stochastic knock intensity predicting model was developed. The correlation to predict the upper-limit knock intensity was found from volume expansion-based pressure rise calculation. The coupled model showed a reasonable match of knock onset and knock intensity distribution compared to the experimental data.

To my family, whose love and support made this work possible.

Funding for this project was provided by the Wisconsin Small Engine Consortium.

Table of Contents

List of Figures

List of Tables

Nomenclature

Abbreviations

aTDC	after Top Dead Center
AEFD	Average Energy in Frequency Domain
AEPO	Average Energy of Pressure Oscillation
AFR	Air-to-Fuel Ratio
CA10	Crank Angle at 10% MFB
CDF	Cumulative Density Function
CFD	Computational Fluid Dynamics
CO	Carbon-Monoxide
CoV	Coefficient of Variance
EGR	Exhaust Gas Recirculation
EVO	Exhaust Valve Open
GEV	Generalized Extreme Value
HCCI	Homogeneous Charge Compression Ignition
IGN	Ignition Timing
IMEP	Indicated Mean Effective Pressure
IMPO	Integral of Modulus of Pressure Oscillations
ISPO	Integral of Squared Pressure Oscillation
IVC	Intake Valve Closing
LES	Large Eddy Simulation

MAPO	Maximum Amplitude of Pressure Oscillation
MBT	Maximum Brake Torque
MFB	Mass Fraction Burned
NTC	Negative Temperature Coefficient
PDF	Probability Density Function
PRF	Primary Reference Fuel
SEPO	Signal Energy of Pressure Oscillation
SER	Signal Energy Ratio
TDC	Top Dead Center
TVE	Threshold Value Exceeded
WOT	Wide Open Throttle

Chapter 1 Introduction

1.1 Background and Motivation

Knock occurs when the compressed fuel and air mixture ahead of the propagating flame front in an SI engines ignites spontaneously. This autoignition of the mixture is governed by the chemical kinetic rates, which are affected by the time history of the end-gas thermodynamic conditions. The thermodynamic conditions are affected by the existence of cycle-by-cycle variations that arise mostly due to differences in the early flame development. For the most severe knocking combustion, about 40% of the mass of the original charge is burned instantaneously to create a rapid local increase of the pressure [1]. A strong pressure wave is induced by the autoignition and excites resonant acoustic modes in the combustion chamber. The knock phenomenon plays a crucial role in the spark ignition engine by limiting the compression ratio, and thus, the efficiency.

Experimental investigations of knock have been performed by various authors [2, 3], and computational methods of estimating knock in terms of the timing and frequency have been proposed [4-6]. Although these previous studies have provided useful information, there have been few studies performed, to the author's knowledge, to anticipate knock onset and intensity in terms of its probability. Knock occurrence is a stochastic event, and knock onset and intensity at a fixed engine operating condition each have distributions. Estimating the probability distributions of knock is important because just a few occurrences of severe knock could damage the piston, head or engine block.

The statistical distribution of knock at a fixed operating point is mainly caused by the existence of cycle-by-cycle variations. Experimental investigation of the cyclic variation, in terms of the

pressure, combustion, flame front and exhaust-gas related parameters, have been performed by various authors [7-10]. In most investigations, it has been concluded that the early flame development, which is largely affected by the turbulent motion near the spark plug, plays the critical role in overall combustion variability. Cyclic variation models using a turbulent distribution near the spark plug during the initial flame development have been proposed by several authors [11-14]. However, turbulence near the spark plug is hard to predict, and the cycle-to-cycle variation is influenced by many other factors.

Sample probability density functions (PDFs) of knock onset and knock intensity for a fixed operating condition are shown in Figure 1.1. The PDF of the knock onset is close to a normal distribution and knock intensity shows a skewed (possibly log-normal) distribution. The spread of knock onset and knock intensity were 7.5 crank angle degrees, and 15 bar for about 10,000 cycles at the fixed operating condition. This distribution of the knock behavior at the fixed operating condition is largely driven by the cyclic variation. The knock onset and knock intensity for every cycle data plotted in Figure 1.1, however, show no direct correlation, see Figure 1.2. Rather, the relation between knock onset and intensity appears to be a random process, and the width of the knock intensity at any given knock onset is at least 10 [bar].

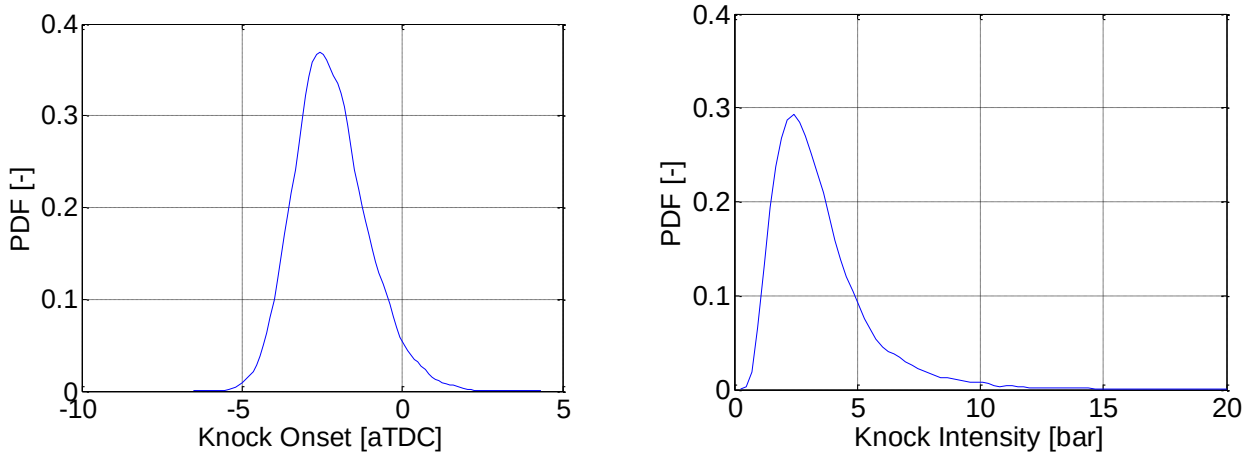

Figure 1.1 PDFs of the knock onset and knock intensity at 1900 RPM, 95% load, AFR13 and ignition timing -35 aTDC

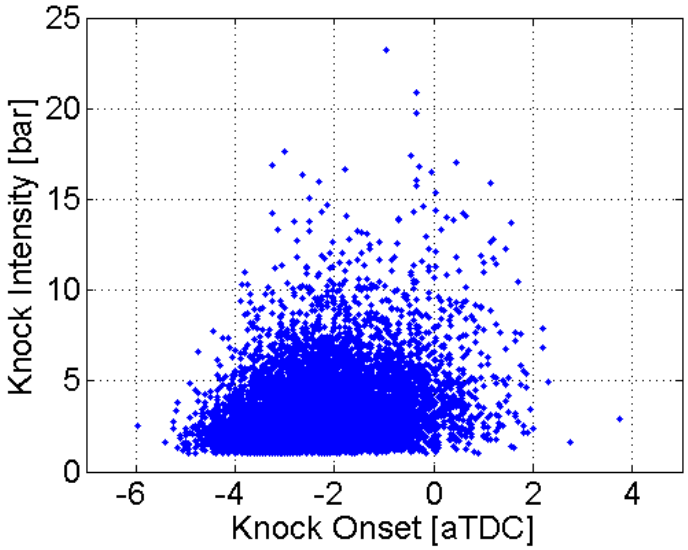

Figure 1.2 Knock onset and knock intensity correlation at 1900 RPM, 95% load, AFR13 and ignition timing -35 aTDC

Predicting knock intensity and its distribution is a challenging subject mostly because of the fact that knowing the thermodynamic conditions at knock onset is not sufficient to predict knock intensity. Figure 1.3 shows in-cylinder pressure and high- and low-pass filtered pressure, P_{HP} and

P_{LP}, respectively, of three cycles that showed very similar pressure trace from intake valve close (IVC) timing to knock onset. It is a reasonable assumption that the end gas thermodynamic conditions at knock onset for these three cycles should be similar. However, the maximum P_{HP} for the cycles varied from 2 to 17 bar. This implies that a single cycle knock intensity cannot be predicted successfully by just determining the end gas thermodynamic conditions at knock onset.

This example strongly suggests that approaches to model the knock based on the ensemble averaged in-cylinder pressure are not sufficient to fully understand knock phenomena. Detailed knock studies using computational fluid dynamics (CFD) calculations require large computational resources to provide an accurate prediction of the spatial distribution of the thermodynamic conditions for each time step, and are therefore CFD is not a feasible method to predict statistical knock distributions.

(a)

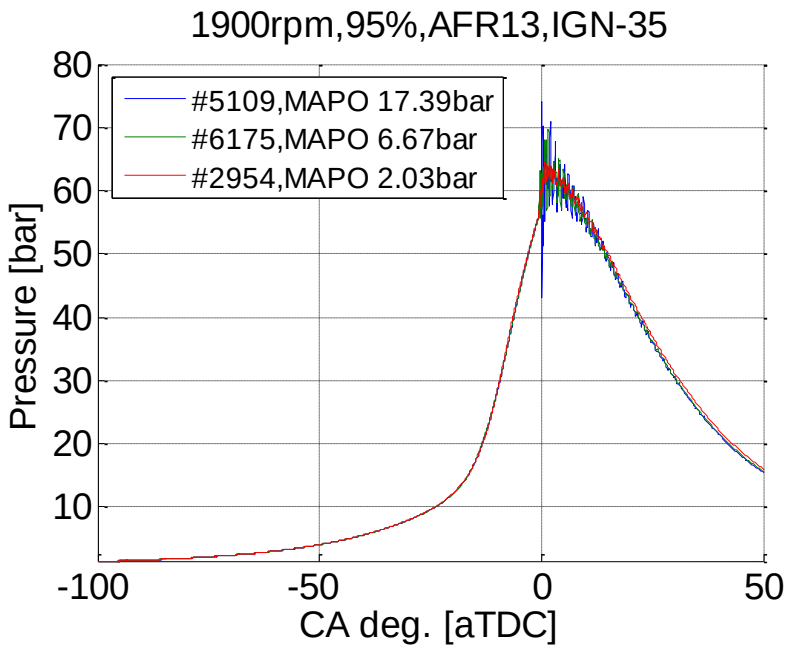

(b)

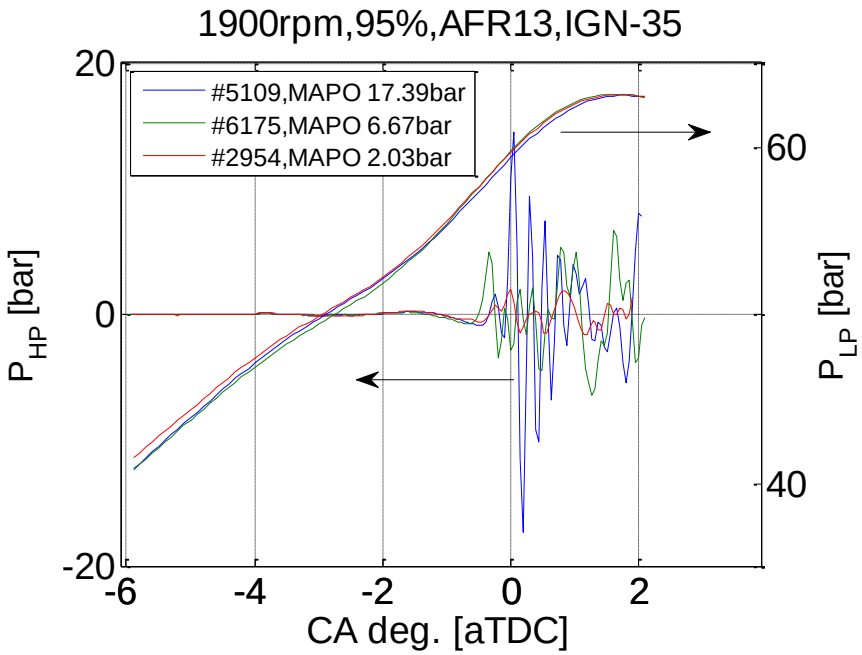

Figure 1.3 Knock intensity comparison between three cycles with similar pressure development at 1900RPM, 95% load, AFR13 and ignition timing -35 aTDC

1.2 Research Objective

The goal of this research is to develop a relatively simple method of characterizing the distribution of combustion profiles at a given condition, i.e., one that includes cyclic variability, and to develop a coupled knock model to predict the distribution of knock onset and knock intensity. This will be accomplished by:

1) Developing a simplified cyclic variation model that incorporates cycle-by-cycle differences in the overall mass burn rate and combustion phasing. The mass burn profile will be predicted for a large number of cycles using a Monte-Carlo simulation. Examination of the relation between the engine operating conditions and the cyclic variation will be made to predict the mass burn fraction of individual cycles at arbitrary conditions.

2) Understanding the factors controlling knock onset and determining the simplest accurate model for its prediction.

3) Understanding the factors affecting knock intensity and developing the simplest accurate model for its prediction.

4) Assessing the performance of the coupled models for predicting the distribution of knock.

This thesis is divided into eight chapters. Chapter 2 reviews studies that have been previously performed on knock and cyclic variation. Chapter 3 describes the experimental setup. Chapter 4 presents knock metrics used in this research. Chapter 5 presents the heat release calculation and thermodynamic engine model. Chapter 6 presents the cyclic variation model using the Wiebe function and a Monte-Carlo approach. Chapter 7 presents the results of the knock distribution model coupled with the cyclic variation model and the method described in Chapters 4 and 5. Finally, the conclusions and future recommendations are summarized in Chapter 8.

Chapter 2 Literature Review

2.1 Engine Knock

There are many different methods to measure knock onset and knock intensity, and these definitions and the correlation between different knock metrics are compared in the following sections. Methods for predicting knock onset and knock intensity are also discussed. Most of the simple, correlation-based approaches are not successful at predicting the severity of knock, but approaches based on mass burn fraction, volume expansion rate and acoustic-based methods show better agreement but are still lacking. Modeling studies, both simple and using full-CFD, show a good agreement in predicting knock onset.

2.1.1 Knock metrics

The strong pressure waves induced by autoignition excite resonant acoustic modes within the combustion chamber. The resonant frequencies of a closed cylindrical combustion chamber can be obtained analytically by solving the general wave equation, and are given by Draper [15].

$$f_{m,n} = c\frac{\alpha_{m,n}}{\pi B} \tag{2.1}$$

where c is the speed of sound, $\alpha_{m,n}$ is the vibration mode constant calculated by the use of Bessel's equations, and B is the cylinder bore diameter. A closed combustion chamber with a bore diameter 65 mm, and uniform temperature of 2500 K, and a constant γ of 1.4 yield resonant frequencies at 8.7, 14.4, 18.1, 19.9 and 25.2 kHz as listed in Table 2-1. Schematic diagrams of pressure pulsations of 1st, 2nd and 3rd circumferential mode and 1st radial mode are shown in Figure 2.1. The majority of the acoustic wave energy is typically contained in the first circumferential mode [16]. However,

the severity of the autoignition is a result of added wave energy contained in the multiple oscillation modes. It is important to note that the oscillation modes are a characteristic footprint of the combustion chamber, and not the knocking combustion [17].

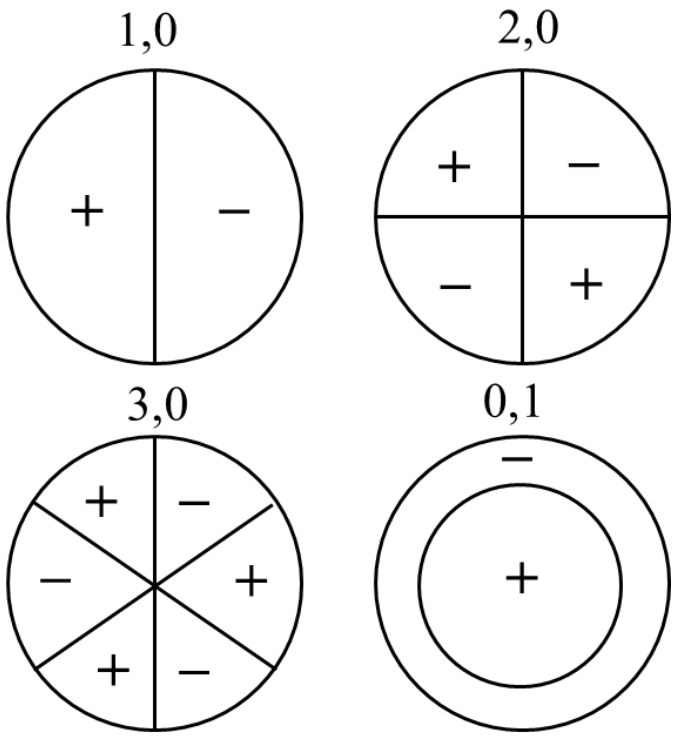

Figure 2.1 Calculated vibration modes for circular cylinder

Table 2-1 Acoustic modes of a cylindrical combustion chamber with T=2500K, Bore=65mm

(m,n)	(1,0)	(2,0)	(3,0)	(0,1)
Oscillation mode	1st circum.	2nd circum.	3rd circum.	1st radial
$\alpha_{m,n}$	1.841	3.054	4.201	3.832
$f_{m,n}$ [kHz]	8.7	14.4	19.9	18.1

There are two important knock properties: knock onset and knock intensity. The knock onset represents the timing of the knock occurrence and the knock intensity is related to the magnitude or severity of the knock event. The most widely used knock metrics are the threshold value

exceeded (TVE) for knock onset, and the maximum amplitude pressure oscillation (MAPO) for knock intensity. These methods use high- or band-pass filtered cylinder pressure data. The time when the filtered pressure exceeds a predetermined threshold is used to determine the knock onset, and the maximum amplitude of the filtered data is used to quantify knock intensity. Figure 2.2 shows a typical knocking cycle pressure trace and the high-pass filtered cylinder pressure (obtained using a 3 [kHz] cutoff frequency). A threshold value of 1 [bar] was used to define the knock onset and the value of knock intensity was determined from the maximum amplitude of the high-pass filtered pressure data. The TVE method is intuitive and simple; however, it detects knock onset late by a few crank angle degrees because the pressure rise must exceed the threshold value, or it does not detect knock for a weak pressure oscillation that does not exceed the threshold value. To avoid late detection, Lee et al. suggested subtracting a constant number from the TVE to determine knock onset [18]. The TVE method can also be biased by the high-pass filter. In Figure 2.2, a dip around -2.5 CA deg., before the initial pressure increase, is seen. The pressure should be close to zero, if the high-pass filter performance is ideal. For certain cycles with large knock intensity, the dip can exceed the threshold value. The TVE method of determining knock onset can also be biased due to the various characteristics of knocking combustion. Figure 2.3 shows high-pass filtered heat release for two different knocking cycles. It is clear that the TVE method for the bottom case is sensing knock onset later than the accurate knock onset. In conclusion, a simple TVE method cannot provide an accurate and trustworthy result of knock onset.

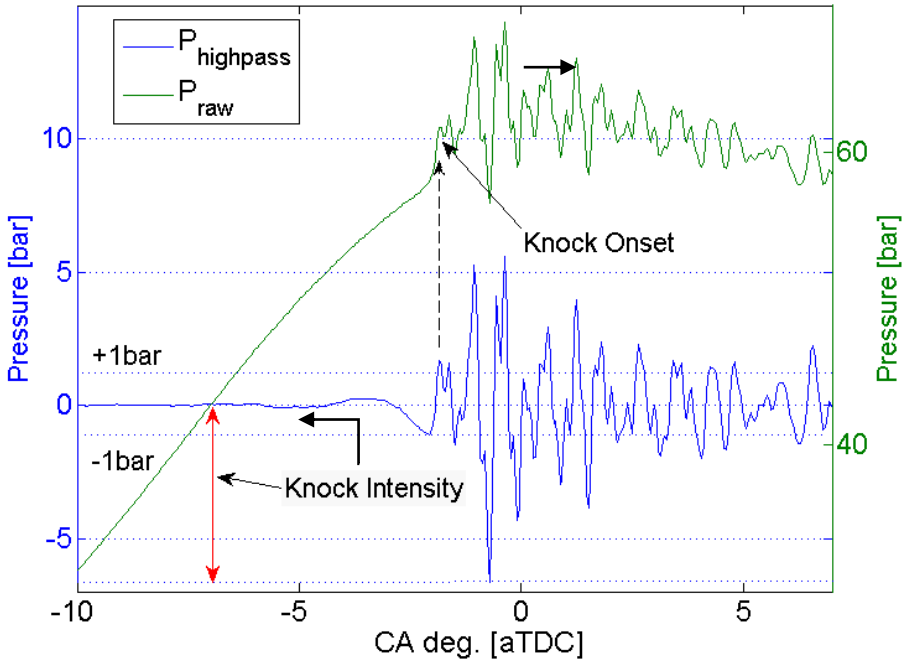

Figure 2.2 Raw and high-pass filtered in-cylinder pressure of the knocking cycle at 1900 RPM, 95% load, AFR13 and ignition timing -35 aTDC

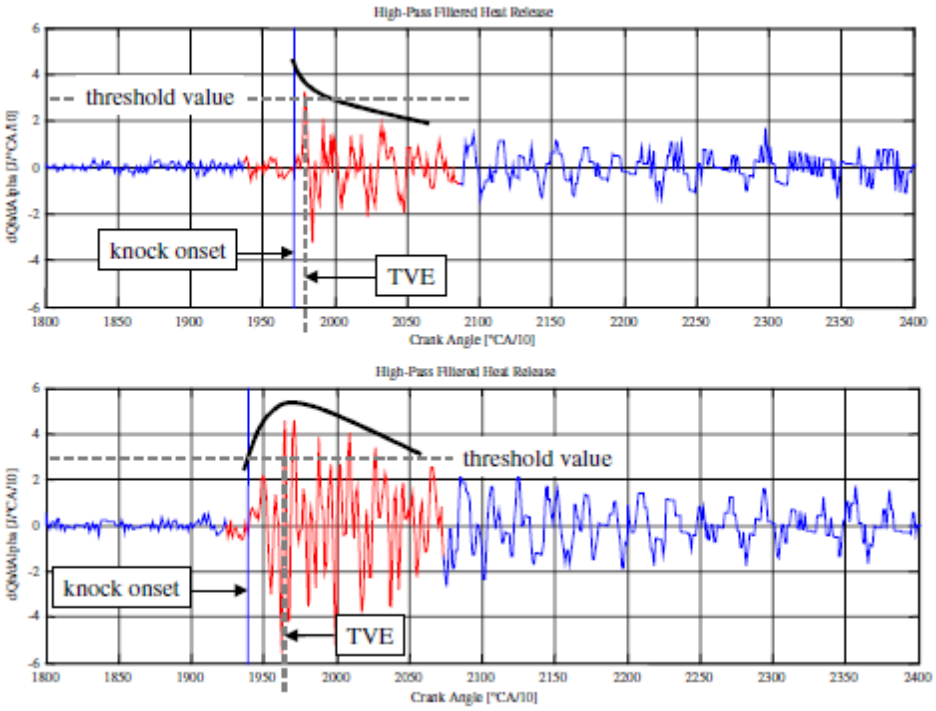

Figure 2.3 Different signal characteristics for two knocking high-pass filtered heat release rate [19]

2.1.1.1 Engine Knock Measurement

To understand and predict knock, accurate measurement of a knock event is important. Many approaches have been investigated to detect knock. The accuracy of knock onset, except when using an optical approach, will be limited because the measurement relies on a secondary effect triggered by the rapid autoignition of the hot-spot instead of measuring the end-gas combustion directly. The optical measurement of knock, however, is limited in use because of the low durability of the measurement system. Other knock detection methods can be grouped by the type of data used to analyze the knock as listed below:

1. In-cylinder pressure
2. Engine block vibration
3. Ion-current signal
4. Rate of heat transfer

The in-cylinder pressure-based knock detection method is most widely used due to its relatively high accuracy and durability. To ensure the reliability of capturing a pressure oscillation, the pressure transducer should be installed near the wall and be flush mounted to avoid cavity resonance [20]. The use of engine block vibration signal to detect knock occurrences is commonly used in commercial vehicles by using a knock sensor to determine the strength of the vibration derived from the engine knock. The vibration data collected from an accelerometer are used as input data to control the ignition timing to avoid knock. However, the engine block vibration data contains noise caused by piston slap and valve train events, which requires further analysis and filtering of the vibration signal to distinguish the impact solely caused by the autoignition [21]. The use of an ion-current sensor also provides a real-time response of a combustion event, however, it requires interpretation of the signal to distinguish abnormal combustion from normal combustion.

The use of heat transfer data is rarely used to detect knock due to its inaccuracy of measuring real time heat transfer rate and low detecting ability of a weak knock.

The most widely used method in knock to detect knock is using a pressure transducer. A pressure transducer has a high natural frequency and can record simultaneous in-cylinder pressure oscillation, which travels at the speed of sound. The collected in-cylinder pressure can be used to provide combustion characteristics such as heat release rate, IMEP, peak pressure and pressure rise rate. To ensure accurate pressure data during knocking conditions, sensor position, mounting and the type of a sensor are important factors [22]. The position of the pressure transducer should be far from the center of the combustion chamber, however, not close to the quench zone to measure the maximum pressure oscillations and the sensor should be flush-mounted to avoid cavity resonance. Figure 2.4 shows the locations of multiple pressure transducers and the measured pressure traces during knocking. It is seen in the Figure 2.4 that the initial pressure rise was measured by the pressure transducer at position #4, which is regarded as the location closest to the hot-spot. The maximum pressure oscillation was measured on the other side of the chamber about 2 crank angle degrees later, at the transducer #5. The possibility exists that using a single pressure transducer, installed at position #4, would not measure the maximum pressure oscillation that occurred during knocking. Instead, the maximum pressure would be the pressure wave reflected by the cylinder wall close to position #5 at 197 crank angle degree. It is also shown in the figure that the amplitude of the pressure oscillation measured by the pressure measuring spark plug (position #6) is smaller than the other transducers. This implies the fact that the pressure oscillation at the center of the combustion chamber would be minimal for most circumferential modes of oscillation.

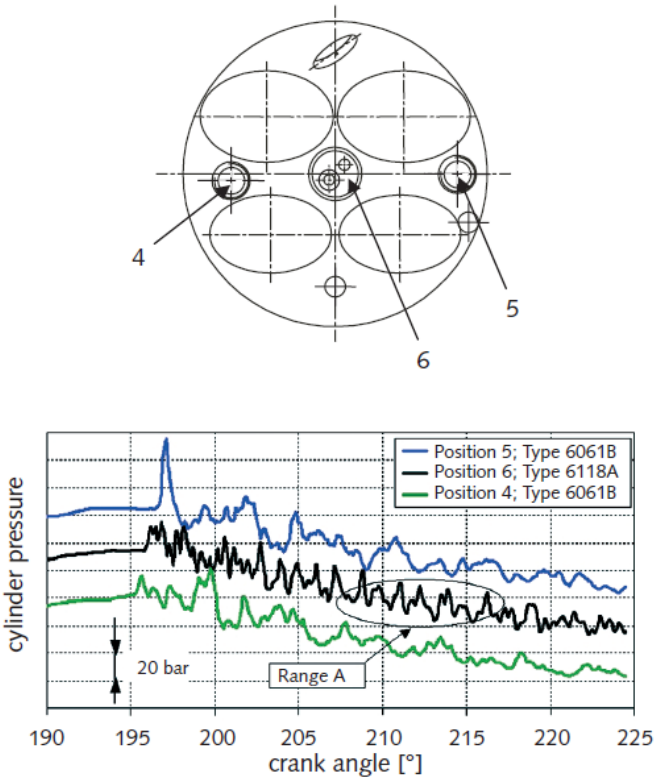

Figure 2.4 In-cylinder pressure measured at different positions [22]

Multiple pressure transducers can be used to measure the spatial distribution of the pressure oscillations and the location of the initial hot-spot [17, 23]. Heittinger and Kulzer used 6 pressure transducers to measure the initial pressure oscillations during knocking conditions to identify knock onset and the knocking zones by triangulation [23]. Figure 2.5 shows the spatial locations of the knocking zone for a number of cycles. Based on the analysis of the pressure data, several cycles were determined to have multiple hot-spots instead of a single knocking zone.

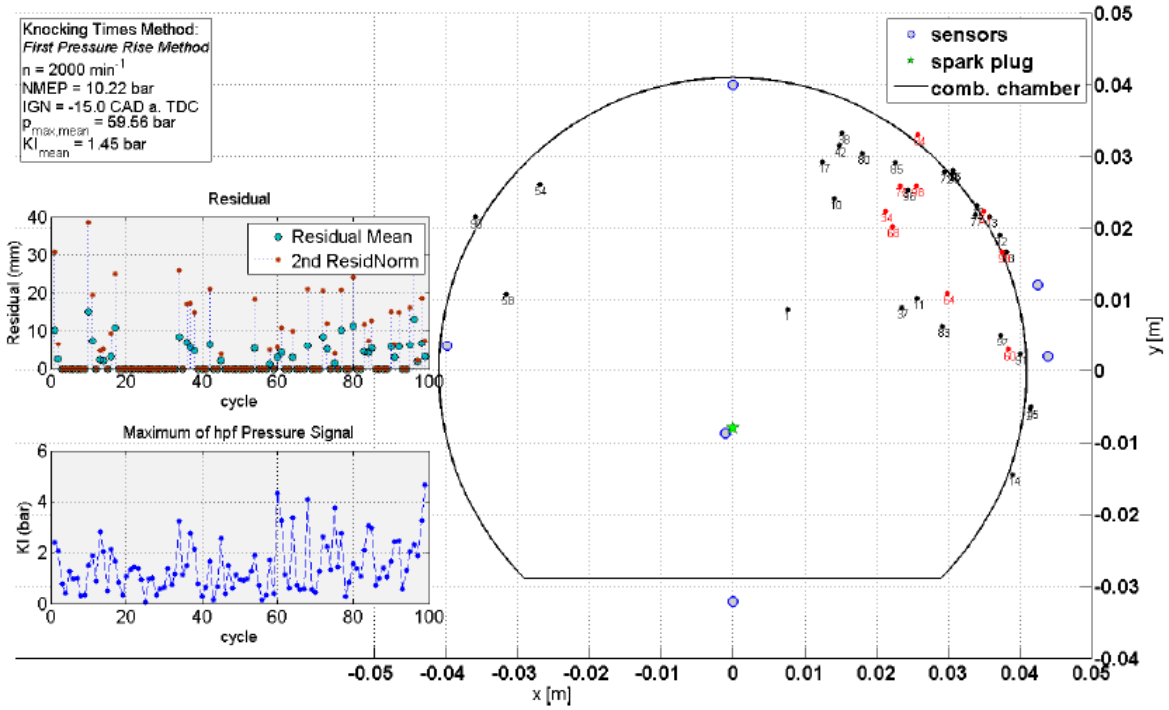

Figure 2.5 Knock location detected using multiple pressure transducer data [23]

Using a single pressure transducer to measure pressure oscillation can be inaccurate and biased by the fact that the location of the hot-spot can be randomly distributed. This randomness is the result of a cycle-by-cycle variation, which determines the thermodynamic condition at knock onset, for example, the amount of unburned fuel, pressure and temperature of the end-gas. The accuracy of the measured pressure oscillation will be limited because the distance between transducer and the location of a hot-spot will be randomly distributed. The possibility of multiple hot-spots during knock is another factor that cannot be determined by using a single pressure transducer.

2.1.1.2 Knock Intensity Metrics

Table 2-2 shows suggested knock intensity metrics and their definitions, sorted into a few general categories [24]. The knock intensity can be calculated on data either in the time or frequency domain; all frequency-domain calculations are performed on the power spectral density. The rapid changes due to the knock can be detected by analyzing either filtered in-cylinder pressure, P_{filt}, and its derivatives, or the heat release rate, $\frac{dQ}{d\theta}$, and its derivatives. Finally, knock intensity metrics can be based on a single value, for example a maximum or minimum value of a quantity, or an averaged or integrated value. Borg and Alkidas classified knock intensity metrics based on the use of pressure data differently as: MAPO, energy-, integral-, and derivative-based approaches [25].

Table 2-2 Comparison of knock intensity metrics

Time Domain	Pressure	Single Value	MAPO	$\text{MAPO} = \max\{P_{filt}\}$	(2.2)
			Ringing Intensity	$\approx \frac{1}{2\gamma}\frac{\left(\beta\frac{dP}{dt}\right)^2}{P_{max}}\sqrt{\gamma R T_{max}}$	(2.3)
			-	$\max\left(\frac{dP}{d\theta}\right), \max\left(\frac{d^2P}{d\theta^2}\right), \max\left(\frac{d^3P}{d\theta^3}\right)$	(2.4)
		Average Value	IMPO	$\sum\lvert P_{filt}\rvert$	(2.5)
			SEPO	$\int_{\theta_0}^{\theta_0+\Delta\theta} P_{filt}^2 d\theta$	(2.6)
			AEPO	$\frac{1}{\Delta\theta}SEPO = \frac{1}{\Delta\theta}\int_{\theta_0}^{\theta_0+\Delta\theta} P_{filt}^2 d\theta$	(2.7)
	Heat release	Single Value	-	$\max\left\{\left(\frac{dQ}{d\theta}\right)_{filt}\right\}, \min\left(\frac{d^2Q}{d\theta^2}\right)$	(2.8)
		Average Value	SEHRO	$\int_{\theta_0}^{\theta_0+\Delta\theta}\left(\frac{dQ}{d\theta}\right)_{filt}^2 d\theta$	(2.9)
			AEHRO	$\frac{1}{\Delta\theta}SEHRO = \frac{1}{\Delta\theta}\int_{\theta_0}^{\theta_0+\Delta\theta}\left(\frac{dQ}{d\theta}\right)_{filt}^2 d\theta$	(2.10)
Frequency Domain	Pressure	Single Value	-	-	
		Average Value	AEFD	$\text{AEFD}_{f_1-f_2} = \int_{f_1}^{f_2}\wp(f)df$	(2.11)
	Heat release	Single Value	-	-	
		Average Value	AEHR	$\text{AEHR}_{f_1-f_2} = \int_{f_1}^{f_2} dQ(f)df$	(2.12)

Energy-based knock quantification methods capture the signal energy contained in the oscillating pressure waves analogous to the relationship between voltage and power. The simplest energy-based approach is the signal energy of pressure oscillation (SEPO) shown in equation (2.6), which integrates the square of high- or band-pass filtered pressure amplitude. The SEPO method

is sometimes called the integral of squared pressure oscillation (ISPO). The size of crank angle window $\Delta\Theta$ is typically 5 to 20 crank angle degrees [19].

A more complicated energy-based approach is the ringing intensity that was suggested by Eng [16]. The ringing intensity, stated in equation (2.3), is based on the acoustic power transmitted by a pressure wave assuming that the amplitude of the pressure waves induced by autoignition will be directly related to the maximum rate of pressure rise rate though a scale factor β, which was determined as 0.05 [ms]. Figure 2.6 shows a comparison between the ringing intensity and maximum pressure rise rate for an engine operated with pure HCCI combustion. The dashed lines stand for the maximum rate of pressure rise limit for naturally aspirated conditions, 1200 *kPa/deg*, and for boosted conditions 2000 *kPa/deg*. The data showed that a ringing intensity of 6 MW/m^2, which had different maximum rate of pressure rise limit for both naturally aspirated and supercharged cases, gave a similar (subjective) noise level. The effectiveness of ringing intensity to characterize the noise level in HCCI combustion has been verified by several researchers [26-28].

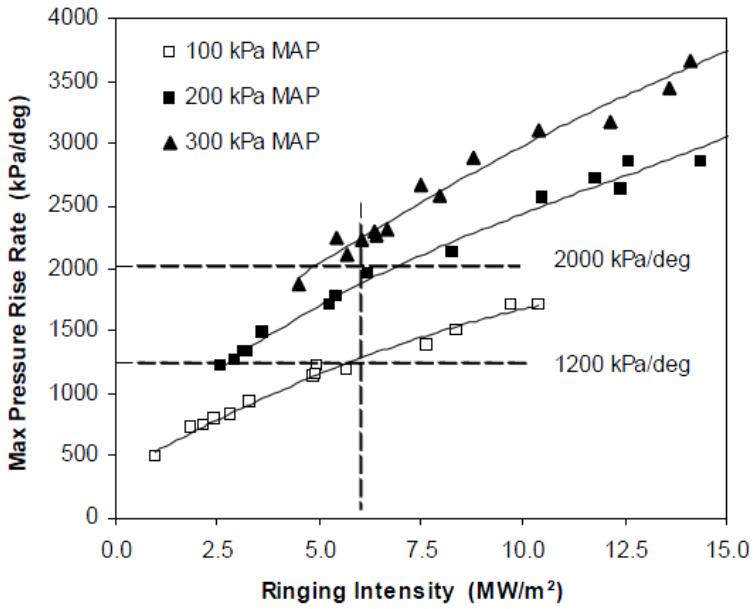

Figure 2.6 Maximum rate of pressure rise plotted as a function of ringing intensity [16]

Derivative-based methods are based on the derivatives of the pressure or heat release data, and use of the maximum or minimum value of first, second and third derivatives have all been proposed in the literature [29, 30]. Use of derivatives is dependent on the quality of the collected in-cylinder pressure signal, and can also be affected by the filtering frequencies.

The correlation coefficient (which is also known as R^2 or residual sum of squares) between MAPO, integral-, energy- and derivative-based metrics are listed in Table 2-3 [25]. It is shown that the energy-based knock intensity metric SEPO and the ringing intensity show a good agreement. Energy-based metrics in time (SEPO) and frequency domain (AEFD) match perfectly, as expected from Parseval's theorem. Derivative-based knock intensity metrics show good agreement with MAPO knock intensity for second and third derivatives of the pressure signal, while derivatives of the low-pass filtered pressure and heat release rate data show weak correlations. However, derivative-based knock intensity metrics are not reliable because they are dependent on the filtering frequency.

Table 2-3 Comparison of knock intensity correlation coefficients [25]

Methods	*Engine speed*			
	1200	*2000*	*3000*	*4000*
SEPO vs. Ringing Intensity	0.92	0.93	0.99	0.95
SEPO vs. AEFD	1.00	1.00	1.00	1.00
Ringing Intensity vs. AEFD	0.91	0.93	1.00	0.95
SEPO vs. MAPO	0.89	0.86	0.90	0.96
IMPO vs. SEPO	0.95	0.92	0.77	0.91
IMPO vs. MAPO	0.96	0.92	0.93	0.90
max|dP/dt| vs. MAPO	0.92	0.96	0.99	0.97
max|d^2P/dt^2| vs. MAPO	0.96	0.98	0.99	1.00
max|d^3P/dt^3| vs. MAPO	0.94	0.96	0.99	0.98
min(d^3P/dt^3) vs. MAPO	-0.94	-0.95	-0.97	-0.99
max|dP_l/dt| vs. MAPO	0.69	0.71	0.48	0.62
min(d^2Q_{HR}/dt^2) vs. MAPO	0.59	0.84	0.84	0.84

Shahlari and Ghandhi suggested that integrated energy-based methods provide more bias-free estimates of the knock intensity compared to the time-domain single-value metrics, *e.g.* MAPO, which could be biased due to destructive and constructive interference of the harmonic waves [24]. The average energy of pressure oscillation (AEPO), stated in equation 2.7, quantifies time-averaged integrated energy during pressure oscillation. A comparison between MAPO and AEPO is shown in Figure 2.7 for 10,000 cycles. The two values are shown to have a general quadratic relationship, but with a significant amount of scatter.

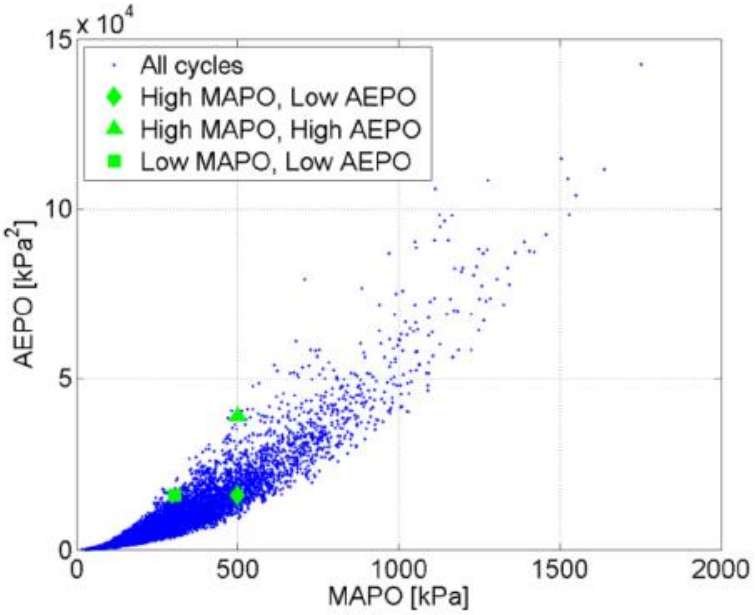

Figure 2.7 Comparison of MAPO vs. AEPO [24]

2.1.1.3 Knock onset metrics

To avoid the biased results of TVE determined knock onset, a signal energy ratio (SER), which is the ratio of the signal energy of knock to the noise signal energy, was suggested by Shahlari and Ghandhi [24]. A signal energy ratio (SER) is defined as

$$\mathrm{SER} \equiv \frac{SEPO_{fwd}^2}{SEPO_{bwd}^{\frac{1}{2}}} = \frac{\left(\int_{\theta_0}^{\theta_0+\Delta\theta} P_{filt}^2 d\theta\right)^2}{\left(\int_{\theta_0-\Delta\theta}^{\theta_0} P_{filt}^2 d\theta\right)^{1/2}} \tag{2.13}$$

where ΔΘ was optimized as 5 crank angle degrees. $SEPO_{fwd}$ is the SEPO for the next 5º CA, and $SEPO_{bwd}$ is the SEPO for the previous 5º CA at the given crank angle degree. Figure 2.8 shows a comparison of the knock onset determined by the TVE and SER methods. The time where the calculated SER is at the maximum is defined as the knock onset by the SER method. The SER knock onset was several crank angles advanced from the TVE knock onset.

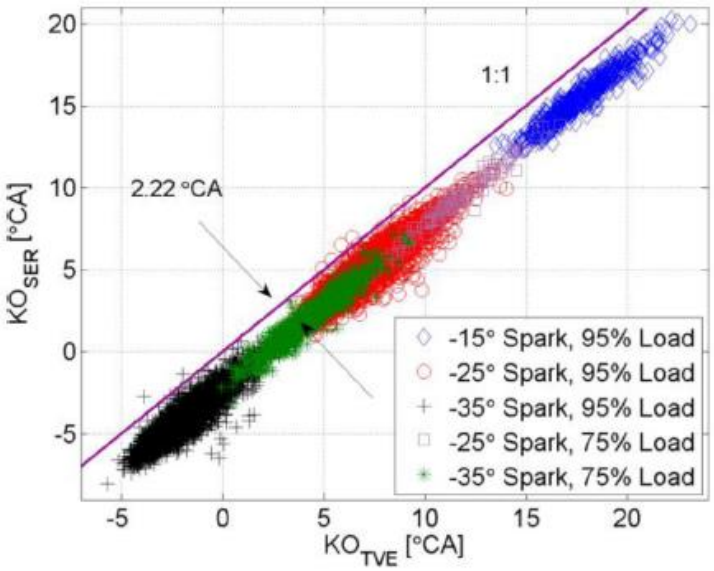

Figure 2.8 Comparison of the knock onset detection between SER and TVE [24]

2.1.2 Knock Intensity Correlation

The knock intensity is a measure of the strength of the pressure waves after the autoignition and, therefore, is one of the most important parameters in a knock study. There have been many studies conducted to correlate the knock intensity to other engine combustion parameters with the intent to provide a method for prediction. The knock intensity prediction methods can be categorized as unburned mass-based, end-gas volume expansion-based and chemical kinetic-based approaches.

Table 2-4 Knock intensity correlations

Chemical kinetics	Najt et al.[31]	$\text{Knock intensity} \approx \mathrm{A}\frac{\mathrm{d}}{\mathrm{d}\theta}[\mathrm{CO_2}] = \mathrm{A}[\mathrm{CO}][\mathrm{H_2O}]^{0.5}[\mathrm{O_2}]^{0.25}\exp(\frac{-4000}{\mathrm{RT}})$	(2.14)
	Cowart et al. [32]	$\text{Knock intensity} \approx \mathrm{A}\left\lvert\frac{\mathrm{d[CO]}}{\mathrm{dt}}\right\rvert_{@1100K}$	(2.15)
	Bradley et al. [33]	$\text{Knock intensity} \approx \dot{q}_a = A\rho\mu_f\Delta H exp(-E/RT)$	(2.16)
Mass burn fraction	Ando et al. [30]	$TdQ_{50\text{-}10}$	(2.17)
	Chun [34]	Unburned $\mathrm{MFB_{@KO}}$	(2.18)
	Borg & Alkidas [35]	x_A (MFB difference between normal and knocking combustion)	(2.19)
	Karim & Gao [36]	$\text{Knock Criterion} = \frac{\text{Energy of end} - \text{gas reaction / Volume}_{\text{end-gas,KO}}}{\text{Energy of combustion/ Volume}_{\text{KO}}}$	(2.20)
	Richard et al. [37]	$\text{Knock intensity} = K_1 X_{u@KO}(CR-1)\sqrt{1-\frac{KO}{K_2}}N_{eng}$	(2.21)
Volume expansion	Hurle et al. [38] Bradley & Kalghatgi [33]	$\mathrm{p(t)} = \frac{\rho}{4\pi \mathrm{d}}\left\lvert\frac{\mathrm{d}}{\mathrm{dt}}\left(\frac{\mathrm{dV}}{\mathrm{dt}}\right)\right\rvert_{\mathrm{t}-\mathrm{t_a}}$	(2.22)
	Yelvington & Green [39]	$\beta = \frac{L_c(\gamma-1)}{\gamma p}\frac{\dot{q}}{u_{sound}} \leq 1$	(2.23)

2.1.2.1 Early Knock Intensity Correlations

Most of these early approaches to quantify the severity of knock were trying to understand knock intensity and its characteristics for a range of operating condition, fuel and knocking combustion, instead of predicting the knock intensity with a good agreement. Some studies showed acceptable correlation with a very small number of data points, but gave an essentially random distribution with an expanded operating range.

Ando et al. investigated the use of various interval and gradient indexes derived from the heat release analysis to correlate the severity of the autoignition [30]. The maximum heat release rate timing before the autoignition was determined to define the time intervals $TdQ_{10\text{-}50}$, $TdQ_{50\text{-}90}$, $TdQ_{90\text{-}50}$, $TdQ_{50\text{-}10}$ as shown in Figure 2.9. Gradient indices, based on heat release analysis, $max(d^2Q/d\Theta_2)$ and $min(d^2Q/d\Theta_2)$ were also investigated. By plotting the interval and gradient indices of 40 cycles in ascending order with different ignition timing cases (shown in Figure 2.10), the authors found that $TdQ_{50\text{-}10}$ and $min(d^2Q/d\Theta_2)$ showed the most distinguished results for different ignition timing (IGN) cases, while the other indices showed no differences. They concluded that those two variables were a good means of predicting the cylinder pressure oscillation.

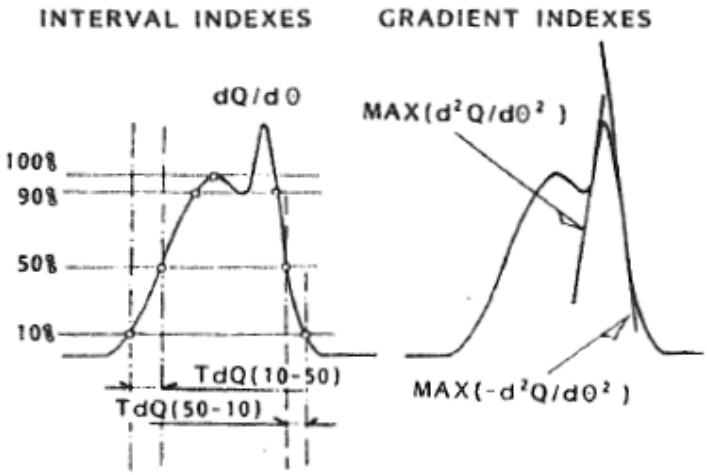

Figure 2.9 Definition of the indexes to express the profile of effective heat release rate [30]

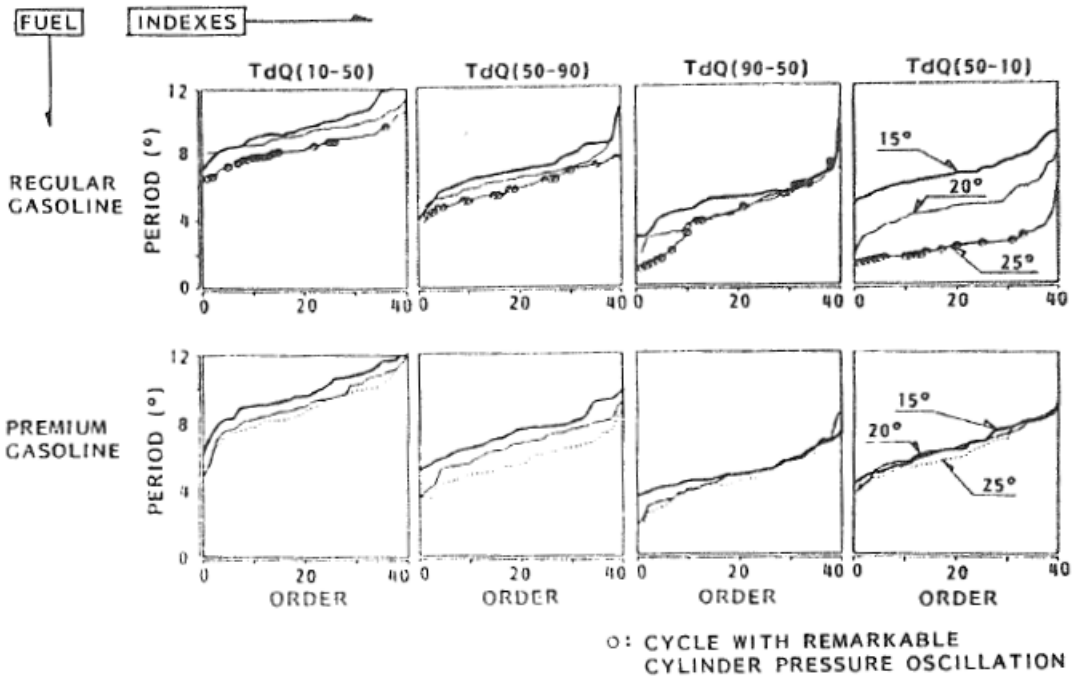

Figure 2.10 Effect of fuel property on interval indices [30]

Karim and Gao suggested a knock criterion that is the ratio of autoignition and normal combustion energy per unit volume, stated in equation (2.20) [36]. This dimensionless knock criteria compares the cumulative energy released by autoignition of the end-gas to the total energy released. It was tested for range of operating conditions and concluded as a possible indicator for quantifying both knock onset and knock intensity with a threshold value of 1.45. It was argued by the authors that knock onset corresponds with the timing of the peak value of the knock criteria and knock intensity corresponds with the peak value. Figure 2.11 shows the knock criterion versus crank angle for different ignition timings. It is determined by this criteria that an ignition timing of 12º bTDC was a borderline case and intense knocking was detected as the ignition timing advances. This approach was followed by Khalil et al. to use knock criteria as an indicator of knock occurrence to develop a knock preventive technique [40]. However, this method was not

verified by comparing both knock onset and knock intensity with other knock metrics. It only shows a general trend of knock onset and knock intensity for a change of operating conditions.

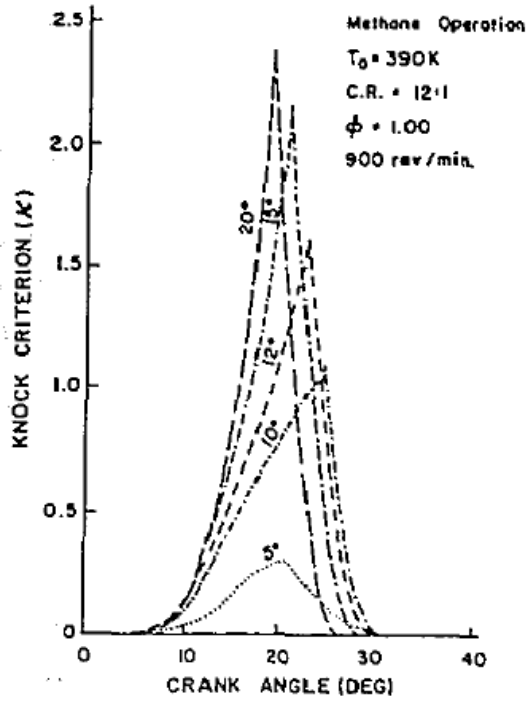

Figure 2.11 Variation of calculated knock criterion for a stoichiometric methane and air mixture [36]

Syrimis et al. investigated knock intensity correlation by measuring the heat transfer rate under knocking conditions [41]. A rapid rise of the heat transfer rate is expected due to the autoignition. The knock severity index found from Ando et al. [30] $min(d^2Q/d\Theta_2)$ and P_{rms} (Root Mean Square amplitude of pressure fluctuation) were compared to the heat flux as shown in Figure 2.12. It was concluded that P_{rms} shows a better correlation with the peak heat flux than $min(d^2Q/d\Theta_2)$, especially at heavy knock cases with near stoichiometric air-to-fuel (AFR) ratio. However, the correlation was not significant as shown in Figure 2.12.

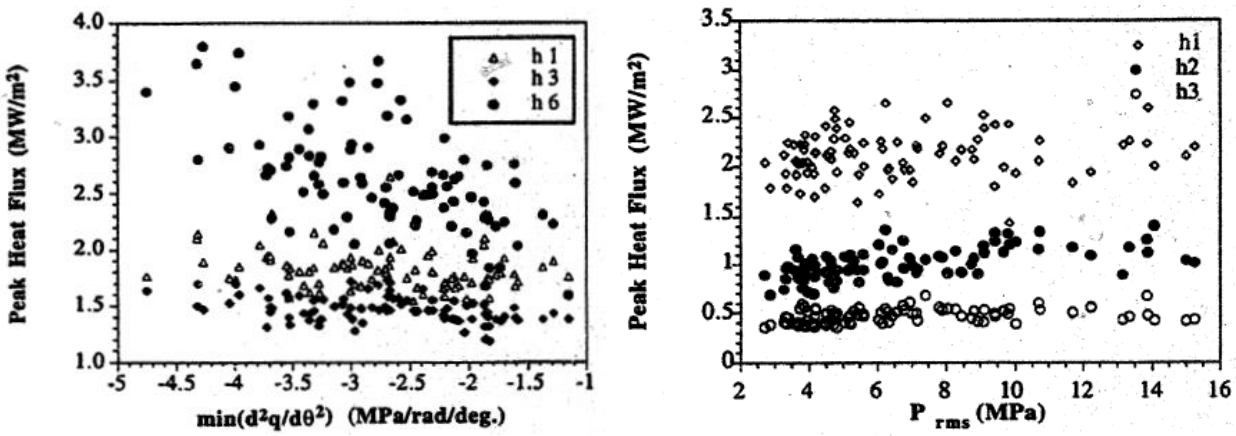

Figure 2.12 Peak heat-flux versus $min(d^2Q/d\Theta_2)$ and P_{rms} for different probe locations at AFR13 [41]

Another approach to correlate knock intensity is to investigate the time derivative of certain species during autoignition as calculated by detailed chemical kinetics. Najt [31] suggested that the knock intensity was a function of the rate of CO_2 production in the end gas, thus the knock intensity should scale with the rate of CO oxidation at the time of knock, see equation (2.14). The rate of CO oxidation represents the hot-flame oxidation, which corresponds with the overall energy release rate. It was concluded that the predicted knock intensity showed a good correlation with the predicted knock phasing (defined as $CA_{@Pmax}$-$CA_{@Knock}$).

Cowart et al. [32] used a detailed chemical kinetic model with 380 species and 1972 reactions to predict the knock intensity following the same approach as Najt [31]. The knock intensity and the time derivative of [CO] at 1100K are shown in Figure 2.13. Cowart et al. claimed that both the knock intensity and probability could be predicted based on the correlation. However, the correlation between predicted $d[CO]/dt$ and the experimentally measured knock intensity for different intake temperature is not unique, and the number of data points is not large enough to validate a convergence of the approach. It is hard to estimate experimental knock intensity with only given predicted time derivative of [CO] value.

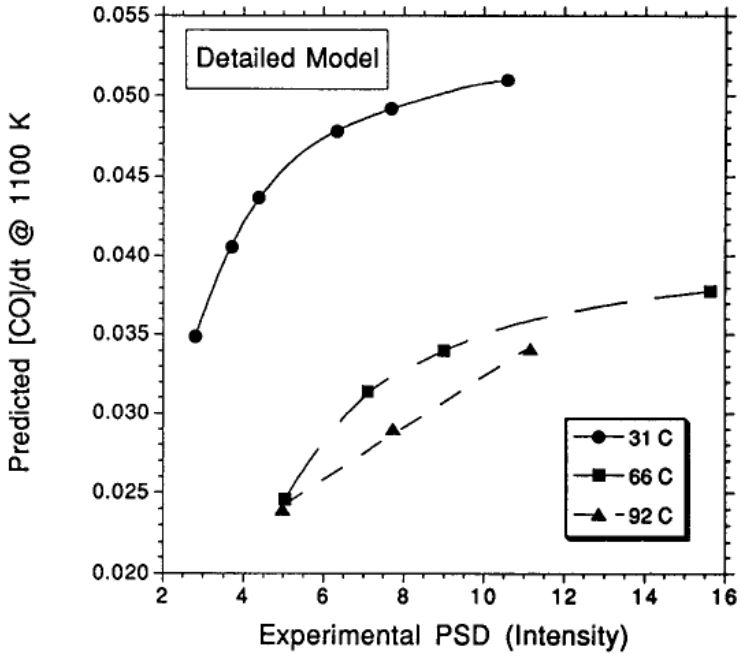

Figure 2.13 Model predicted [CO]/dt@1100K against experimental PSD [32]

2.1.2.2 Chemical kinetics based knock intensity

Bradley et al. used an estimated value of the volumetric autoignition heat release rate to correlate with the knock intensity [33]. The volumetric autoignition heat release rate was calculated by separating the rate of heat release between normal flame propagation and autoignition of the end-gas. An Arrhenius form, stated in equation (2.16), was assumed to predict the volumetric heat release rate, where A is an Arrhenius constant, μ_f is the mass fraction of the fuel and E is the activation energy. The volumetric autoignition heat release $\dot{q}_a$ was approximated by $Q_{am}\rho/m_a$, where Q_{am} is the difference of the mean heat release rate between the maximum heat release rate due to the autoignition and the heat release rate at the knock onset. The Arrhenius constant and the activation energy for different fuels were determined from finding the best fit between the temperature and $\dot{q}_a$, calculated by experimental heat release. The autoignition volumetric heat release rate calculated by using the fitted Arrhenius constant and the activation energy for knock intensity are shown in Figure 2.14. A weak linear correlation for a toluene/n-heptane mixture was found and a general quadratic relation was found for PRF fuels. This approach relies on an accurate estimation of the heat release rate and the temperature of the end gas. The end gas temperature was estimated by a correlation based on the in-cylinder pressure, instead of full- CFD or multi-zone code, which predicts those values more accurately.

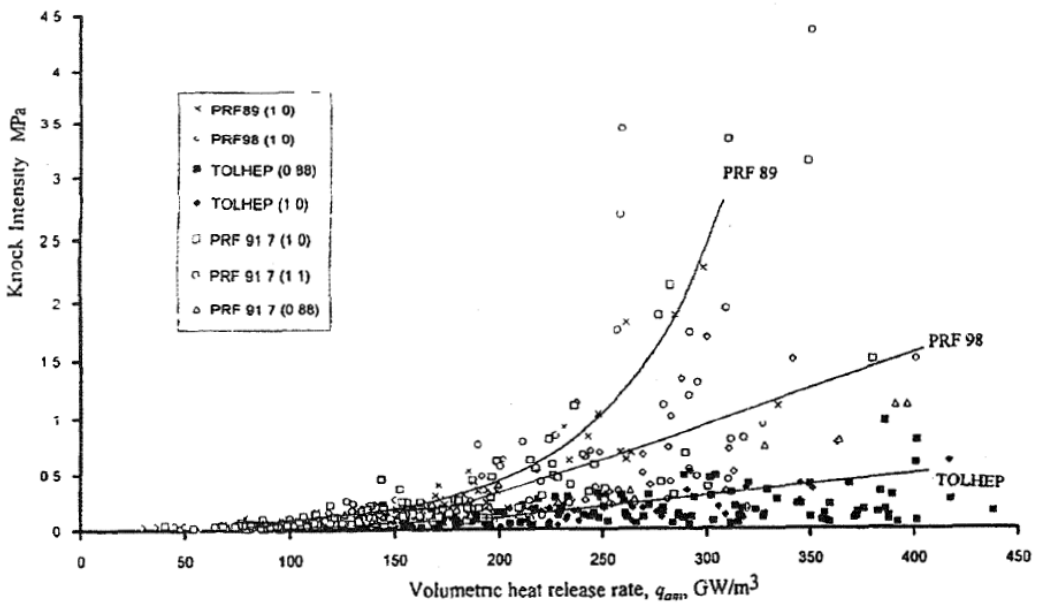

Figure 2.14 Knock intensity plotted against the autoignition volumetric heat release rate [33]

2.1.2.3 Mass burn fraction and knock intensity

There have been many attempts to quantify the severity of knock by correlating to the cumulative energy release at the onset of knock [35, 36, 42]. Chun investigated the effect of the engine operating conditions on the knock onset and knock intensity and concluded that combustion-related parameters are well correlated with the knock onset, while the individual knock intensity does not correlate with the combustion rate or unburned fuel mass at the knock onset [34]. The time from spark ignition timing to 50% of the fuel mass burnt are plotted against the measured knock intensity in Figure 2.15 (a). The 50% burn duration represents the early flame development of the mixture, which plays an important role in the cyclic variation. It is assumed that the cyclic variation is mostly controlled by the early flame development and has large effect on the knocking combustion. However, weak correlations were found for the range of engine operating conditions. Figure 2.15 (b) shows the unburned mass fraction at knock onset and its correlation to knock intensity. It could be easily assumed that the pressure oscillation produced

by the autoignition should be proportional to the rapidly released energy of the end-gas. The general trend found for different engine operating conditions is increasing knock intensity as unburned mass fraction increases; however, the spread of knock intensity at the given unburned mass fraction was large, about 4 [atm].

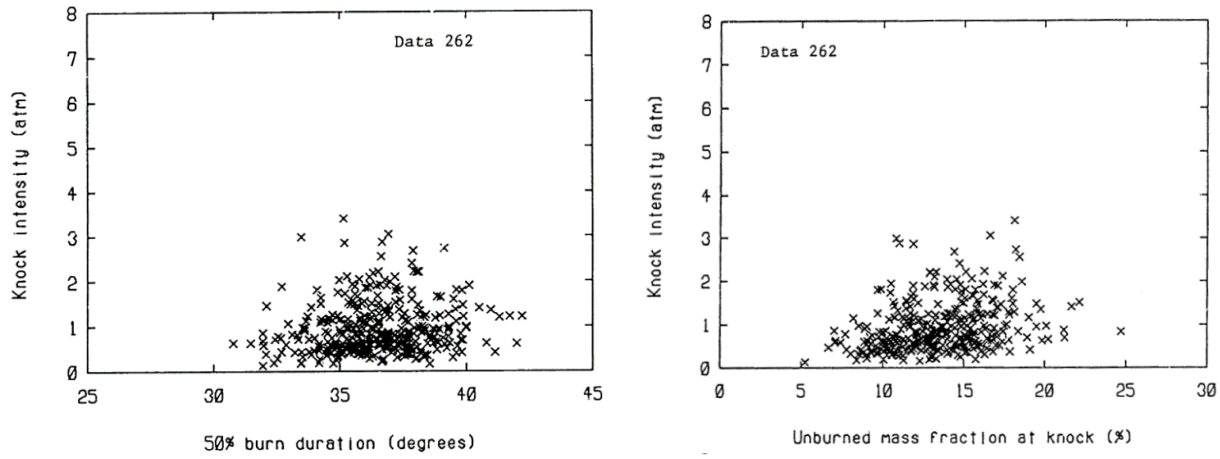

(a) (b)

Figure 2.15 Knock intensity and its correlation with unburned mass fraction [34]

Instead of comparing the unburned mass fraction at knock onset to knock intensity, Borg and Alkidas [35] curve-fit a Wiebe function to characterize the combustion profile of each cycle to calculate the potential difference in the energy release due to the autoignition and that of the normal combustion wave propagation. The parameter x_A was defined as the difference between the experimental and predicted non-knocking heat release rate at the time when the mass burn fraction was 0.99. Figure 2.16 shows the definition of parameter x_A (left) and its correlation to the knock intensity determined by the MAPO method. A weak correlation is observed.

(a)

(b)

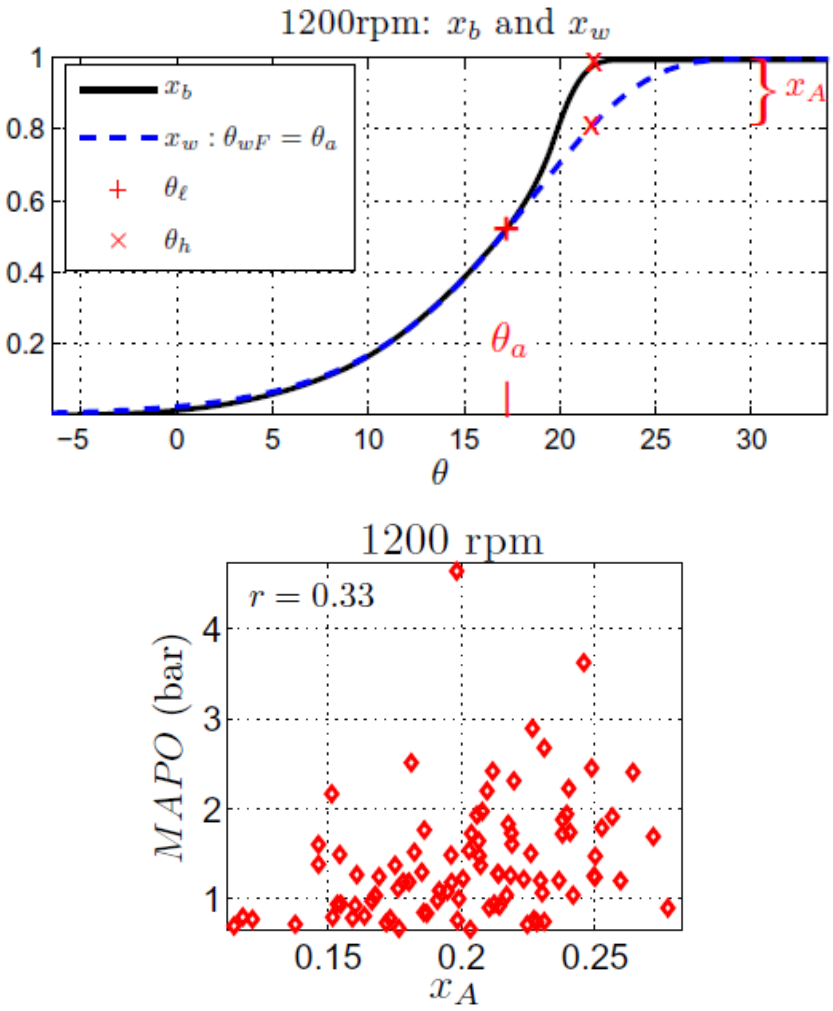

Figure 2.16 Estimating x_A and its correlation with knock intensity [35]

2.1.2.4 Volume expansion rate based knock intensity

A rapid energy release due to autoignition increases both pressure and volume of the end-gas, which is restricted by interaction with the burned gas at a given pressure. Experimental knock intensity is determined mostly by the amount of energy that is contained in the pressure oscillations due to its ease of measurement compared to measuring the end gas volume change. However, in modeling approaches, the volume expansion rate could be predicted with several assumptions.

With this motivation, there were several studies suggested to correlate knock intensity by predicting the volume expansion at the timing of knock.

Yelvington and Green suggested a knock intensity correlation that predicts viable HCCI operating range based on the volumetric heat release rate [39]. It was argued by the authors that a rate of pressure rise should be determined by the competition between volume expansion work at the speed of sound and rate of chemical heat release. A local overpressure will occur when the combustion rate is fast enough before fuel and air parcel expanding to equilibrate the in-cylinder pressure. Their correlation to determine knock in an HCCI engine is stated in equation (2.24) where, L_C is characteristic length taken as 1/10 of the engine bore and $\dot{q}$ is the volumetric heat release rate. A volumetric heat release rate due to the chemical heat release was scaled with A^*u_{sound}, where A is frontal area of the end-gas and u_{sound} is the speed sound at the given thermodynamic conditions. A newly introduced term, β, accounts for both work done by volume expansion and the rate of chemical heat release due to the autoignition. The differences between SI and HCCI knock should be noted that the competition between turbulent flame speed and ignition delay at near stoichiometric mixture determines overpressure at SI engine, while the competition between the heat release rate in the lean mixture and fuel and air mixture parcel expanding speed determines viable knock in HCCI combustion. The KIVA-3V CFD code was used to predict HCCI knock limits for different equivalence ratios and EGR rates. The predicted knock limits were well matched with the experimental knock limit of 5 bar/degree.

$$\beta = \frac{L_c(\gamma-1)}{\gamma p}\frac{\dot{q}}{u_{sound}} \leq 1 \qquad (2.24)$$

Bradley and Kalghatgi [33, 43] investigated super-knock in boosted spark ignition engines by the relative differences between the spatial distribution of ignition delay and the ignition wave propagation speed. For the most severe knocking combustion, about 40% of the mass of the original charge is burned instantaneously to create a rapid increase of the pressure and rapid rate of change of the volume, *dV/dt*. By acoustic theory, the instantaneous sound pressure *p(t)*, at the distance *d* from the source can be expressed as equation (2.25) [38]. The volumetric expansion rate of the hot spot with the area of the reaction front are, *A*, propagating to the unburned gas at a velocity u_a is $A*u_a$. The burned and unburned gas density difference should be accounted for to calculate the net rate of the volume expansion as stated in equation (2.26), where σ is the ratio of unburned to burned gas densities. Assuming a small spherical hot spot of radius *r* and differentiating equation (2.26) with respect to *t* gives the volume expansion rate as stated in equation (2.27). Combining equation (2.27) with (2.25) gives equation (2.28) where $\xi=a/u_a$ and *a* is the speed of sound gives non-dimensional form of pressure oscillation as stated in equation (2.28).

$$\Delta p(t) = \frac{\rho}{4\pi d}\left|\frac{d}{dt}\left(\frac{dV}{dt}\right)\right|_{t-t_a} \tag{2.25}$$

$$dV/dt = Au_a(\sigma - 1) = 4\pi r^2 u_a(\sigma - 1) \tag{2.26}$$

$$\left|\frac{d}{dt}\left(\frac{dV}{dt}\right)\right|_{t-t_a} = 4\pi r(\sigma - 1)\left(2\sigma u_a^2 + r\frac{du_a}{dt}\right) \tag{2.27}$$

$$\frac{\Delta p(t)}{p} = \left[\frac{r\gamma}{d}(\sigma - 1)\left(2\sigma\xi^{-2} + \frac{r}{a}\frac{d\xi^{-1}}{dt}\right)\right]_{t-t_a} \tag{2.28}$$

Figure 2.17 (a) shows the history of a hot spot temperature, pressure and combustion wave speed during a developing detonation where the initial conditions were r_0=3 [mm], ξ=1, Φ=1, T_0=1200

[K] and P_0 =5.066 [MPa]. A rapid pressure and temperature rise is found after time sequence 1, which was 35.81 [μs]. The wave speed at the fully developed detonation was near 1600 m/s, which is close to the Chapman-Jouguet velocity. By using an excitation time for energy release energy τ_e, another dimensionless parameter $\varepsilon=(r_0/a)/\tau_e$, which is a measure of the hot spot reactivity, was introduced and plotted against the resonance parameter ξ, in Figure 2.17 (b). Conditions of developing detonation are marked with the upper and lower limit. This work provided an explanation on the volume expansion and its criteria for developing detonation, however, further investigation comparing experimental results of knock intensity is needed.

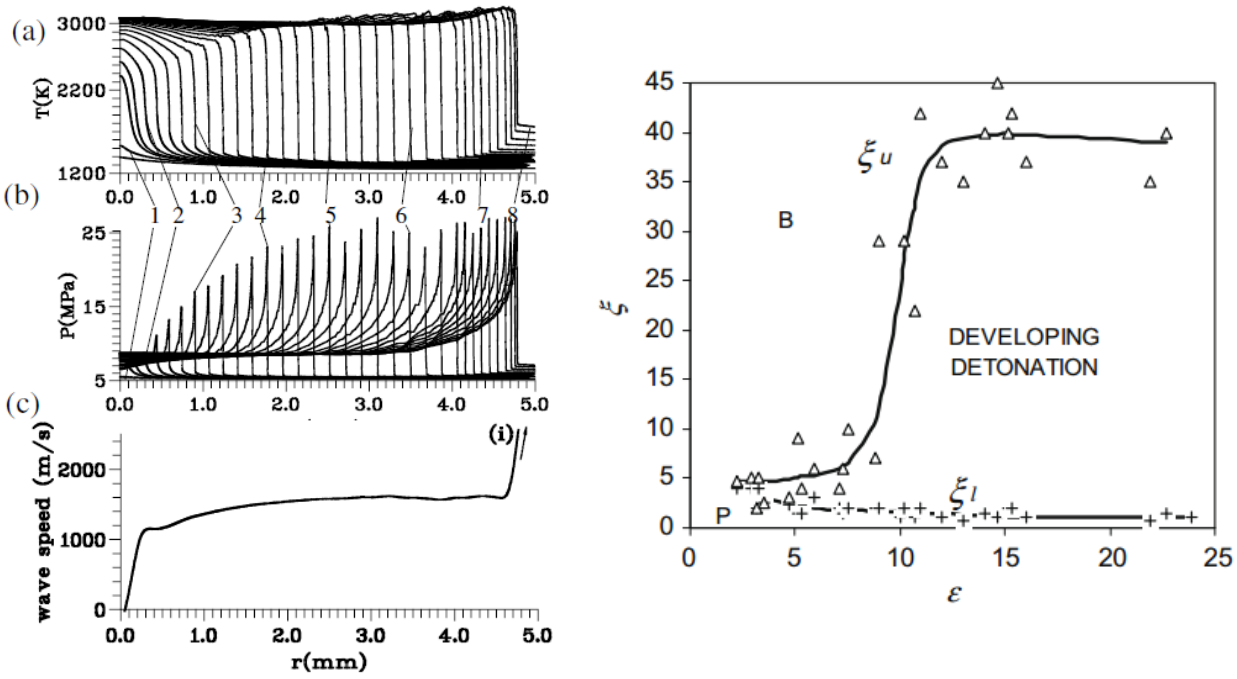

(a) (b)

Figure 2.17 History of a hot spot during detonation and conditions for the developing detonations [44]

Most knock intensity correlation approaches discussed in this section were not successful at predicting the knock intensity. Correlations based on the heat release rate data cannot avoid biases

caused by the filtering of in-cylinder pressure and, therefore, are not feasible to be used for the wide range of the knocking combustions. Verification of correlations based on a single thermodynamic parameter, such as a time derivative of species concentration or mass burn fraction, only showed a very weak correlation.

2.1.2.5 Blast Wave Theory

A blast wave is the pressure wave from a release of large amount of energy in a relatively small volume, generated by high explosives that detonate to deliver a propagating supersonic shock front. G.I. Taylor investigated the blast wave assuming an idealized point source of energy released abruptly and the spherical shock wave propagating outward based on the similarity solution as stated in equation (2.29) [45].

$$E = \left(\frac{\rho_0}{t^2}\right)\left(\frac{r}{\gamma}\right)^5 \tag{2.29}$$

The variables are the energy released E, density of air ρ_0, time duration t, radius of the blast wave, r, and the specific heat ratio of air γ. The wave travelling speed resulting from autoignition in an engine is thought to be sonic for engine-like temperatures, and therefore, the physical link between a point source explosion and the autoignition event in engine is not very strong. However, blast wave theory provides a link between released energy, time, and the size of the volume expansion that could be useful in estimating the time and size of a hot-spot after the autoignition.

2.1.3 Knock Modeling

There have been many knock models suggested ranging from the relatively simple knock integral method for knock onset, to simplified single-zone thermodynamic models incorporating detailed chemical kinetics, to spatially resolved CFD or LES models.

2.1.3.1 Knock onset modeling by knock integral method

The simplest method for predicting the onset of knock is the knock-integral model introduced by Livengood and Wu [46]. The knock integral, shown in equation (2.30), relies on an expression for the ignition delay for the time-varying thermodynamic state of the end gas mixture.

$$\int_{t=0}^{t_i} \frac{1}{\tau_{ig}} dt = 1 \tag{2.30}$$

Douaud and Eyzat proposed an empirical correlation to calculate the ignition delay as a function of the pressure, temperature and octane number (ON) as seen in equation (2.31) [47]. Studies conducted by various authors [42, 48, 49] to predict the onset of knock based on the knock-integral method have shown promising results. Although the knock-integral method provides a reasonably accurate prediction of the knock onset with limited calculation complexity, its use is limited to predicting the knock onset. The location of the knock sites, species chemical concentration changes and the combined effects on the knock onset, and the knock intensity must be predicted by other approaches.

$$\tau_{ig} = A\left(\frac{ON}{100}\right)^{m} p^{n} \exp\left(\frac{B}{T}\right) \tag{2.31}$$

2.1.3.2 Acoustics based pressure oscillation

Draper [15] provided a mathematical description of the pressure oscillation based on the acoustic wave theory to give a general solution of the pressure wave in cylindrical coordinates. Brecq and Le Corre [50] suggested the acoustic-oscillation model to predict the pressure envelope curve under knock conditions by solving equations (2.32) and (2.33) using Draper's disk-shaped geometry model approach [15], where $\tilde{p}$ is outer layer pressure corresponding with pressure oscillation and θ is window crank angle.

$$\tilde{p}(\theta) = aC\frac{\beta}{\alpha}e^{\frac{a^2}{2\alpha}}\left(\psi(\theta) - \frac{1}{a}e^{\frac{a^2}{2\alpha}} + \frac{1}{\beta}e^{\frac{\beta^2}{2\alpha}}\right) \tag{2.32}$$

$$\psi(\theta) = \int_0^{\theta} e^{\frac{(\alpha t+\beta)^2}{2\alpha}}dt,\ a = \alpha\theta + \beta \tag{2.33}$$

Coefficients used in equations stand for the slope α, the engine signature β and the cyclic knock feature C were found by the least square method to find best match with the experimental results. Figure 2.18 shows the model results of predicted knock intensity, defined by the MAPO method, with experimental results. Although there was a good agreement between the model and the experimental results, three coefficients should be found by finding the best match compared to the experimental results. Those coefficients are only valid for the fixed engine operating condition and must be changed for different conditions.

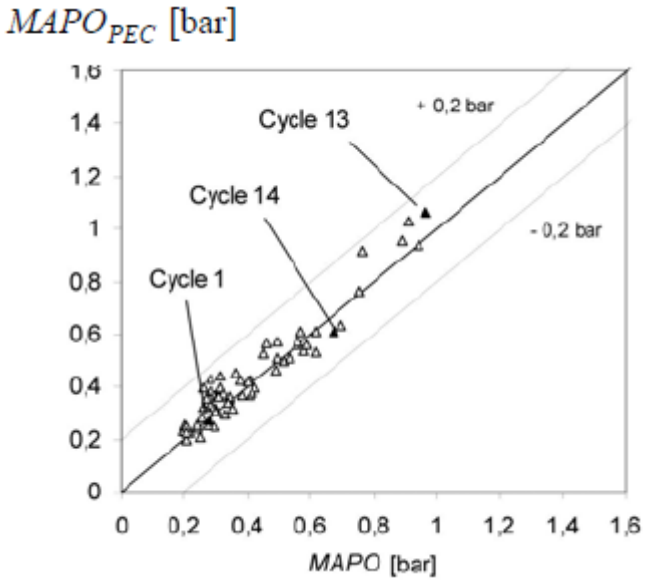

Figure 2.18 MAPO validation between experiment and the model [50]

Gaeta et al. [51] further improved Brecq and Le Corre's approach, and developed a model that predicts the oscillation of the pressure wave under knocking conditions by solving a wave equation. The pressure disturbance in cylindrical coordinates with a damping constant σ is shown in equation (2.34). The damping constant was evaluated based on experimental results, i.e. matching the time decay of the pressure oscillation. A two-zone thermodynamic model was developed based on the experimental cylinder pressure, inlet and exhaust mean pressures, and air and fuel mass flow rates to calculate the burned mass fraction and temperatures of burned and unburned gas. The mean pressure, burned and unburned volume and volume expansion rate at knock onset calculated by the two-zone model were used as initial conditions for the wave equation. The model was validated by using a genetic algorithm to optimize the model parameters, such as, damping constant, volume, size and location of unburned gas, and the pressure derivative at knock onset. Figure 2.19 shows well matched pressure oscillation and its frequency spectrum calculated

by the model and the experiment. However, the model is limited with the parameter optimization and therefore, is demonstrative rather than predictive.

$$\frac{\partial^2 p}{\partial t^2} + \sigma \frac{\partial p}{\partial t} = a_0^2 \left[\frac{\partial^2 p}{\partial r^2} + \frac{1}{r} \frac{\partial p}{pr} + \frac{1}{r^2} \frac{\partial^2 p}{\partial \theta^2} + \frac{\partial^2 p}{\partial z^2} \right] \quad (2.34)$$

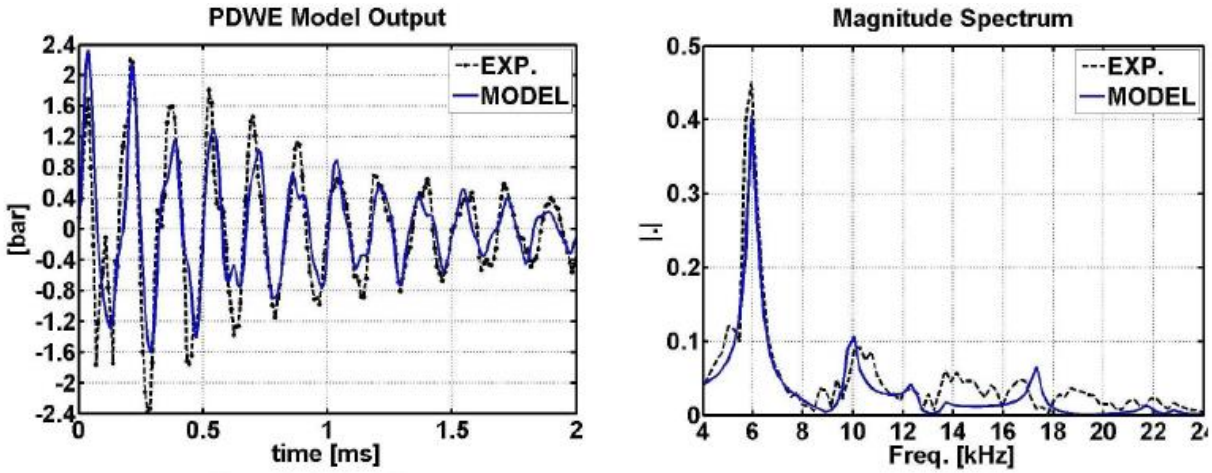

Figure 2.19 Comparison of the model predicted pressure oscillation and frequency spectrum [51]

2.1.3.3 Full-CFD model

The rapid increase of computing power has triggered expanded computational research into knock phenomena. Knock-predicting models using a turbulent flame propagation model and full combustion kinetics have been introduced [4-6, 52-56]. A full CFD calculation can provide highly accurate predictions of knock onset timing, the location of the knock, and the development of pressure waves in the cylinder. However, even with the fastest computer, the calculation time is relatively long and therefore, using a full CFD calculation is not a viable way to model cyclic variation and its effect on knock. As a result, most full-CFD knock models are limited to calculating the average cycle or a few characteristic cycles chosen arbitrarily.

Blunsdon and Dent developed a computational knock model in the KIVA-2 code by implementing the mixing-controlled combustion model and the Shell autoignition model [4]. They investigated knock phenomena in a simple, disk-shaped three-dimensional domain as shown in Figure 2.20. The model was developed based on the Ricardo E6 engine operating at a baseline, light knock condition. The effects of ignition timing, turbulent kinetic energy, EGR and swirl on autoignition characteristics were predicted by the model. The CFD results showed different pressure oscillation characteristics at different locations, see Figure 2.20, of a computational pressure transducer. A mean pressure oscillation was calculated for each operating condition. Knock intensity determined by MAPO and SEPO methods from the model predicted pressure data and compared to different ignition timings. A general trend of increased knock intensity as ignition timing advances was found. However, the work done by Blunsdon and Dent was limited to only computational work and the predicted knock intensity was not compared directly with experimental knock measurements.

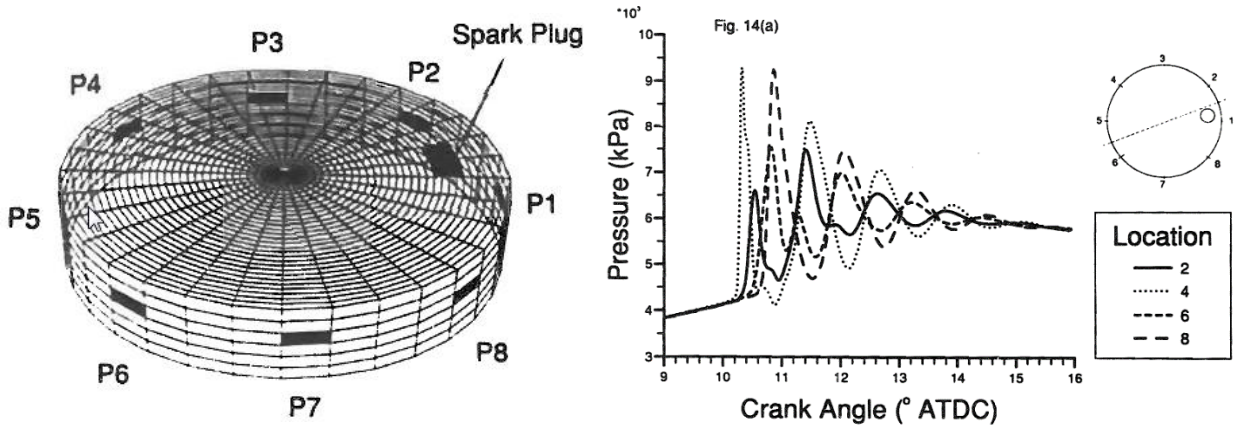

Figure 2.20 Computational mesh at TDC and predicted pressure oscillation [4]

Liang et al. used a *G*-equation model to describe premixed turbulent flame front propagation, and incorporated detailed chemical kinetics to model end gas autoignition [6]. The computational

mesh shown in Figure 2.21 (a) contained 170,000 cells and included the intake and exhaust manifolds. The G-equation model was validated with experimental in-cylinder pressure, and showed a good agreement for different ignition timing and manifold pressure cases. To determine knock from the model result, a knock index *KI* was defined as,

$$\mathrm{KI} = \frac{1}{N}\sum_{n=1}^{N} PP_{max,n} \tag{2.35}$$

where PP_{max} is the maximum peak-to-peak value and N is the number of numerical pressure transducer locations. Figure 2.21 (b) showed predicted in-cylinder pressure and its oscillation due to the autoignition of the end-gas. The predicted knock intensity index increased as spark timing advanced. The effects of the cooled EGR and a split-injection strategy on the knock mitigation were investigated. However, only a single cycle was calculated for the given operating condition, and the effect of cyclic variations in the knocking combustion was neglected.

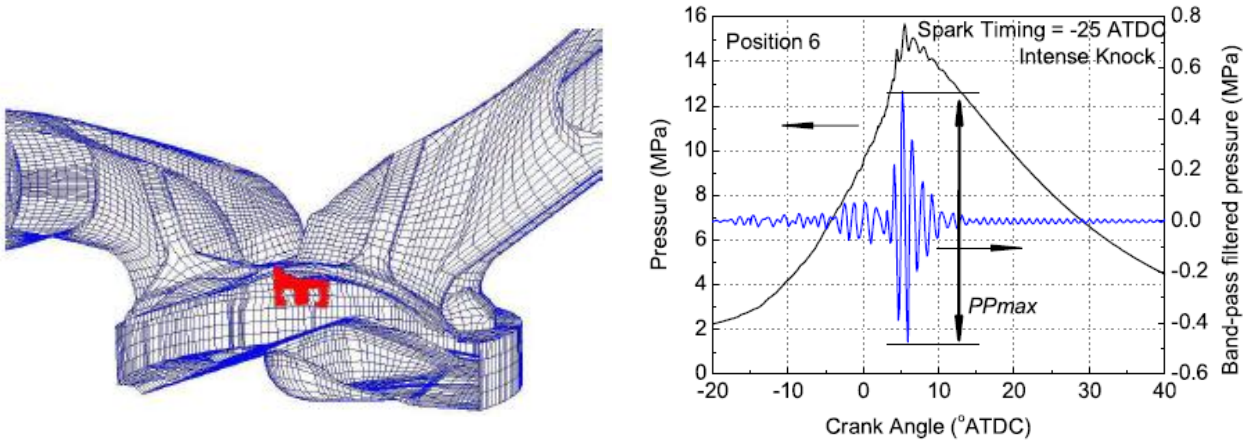

(a) (b)

Figure 2.21 Computational mesh and predicted raw and filtered pressure [6]

2.2 Cyclic Variation

Even when running at a fixed operating condition, the cylinder pressure of each cycle is different. Cyclic variations result from the slight variation in the engine input parameters (trapped mass of fuel, air and exhaust residual), and from the stochastic mixture motion, flame development and flame propagation. Minimizing cyclic variations is important to improve the vehicle driveability, and to push the operating conditions closer to their limits.

2.2.1 Measures and Factors of Cyclic Variation

2.2.1.1 Measures of Cyclic Variation

The measures of cyclic variation can be categorized as pressure-based, burn rate-based and flame position-based as listed in Table 2-5 [8, 9, 57].

Table 2-5 Measures of Cyclic Variation

Pressure	p_{max}	Maximum pressure	
	CA_{pmax}	Location of peak pressure	
	$(dP/d\Theta)_{max}$	Peak pressure rise rate	
	IMEP	Indicated mean effective pressure	
Burn rate	$(dQ/d\Theta)_{max}$	maximum heat release rate	
	Flame development angle	$CA_{0\text{-}10}$	the crank angle at which 10% of the energy has been released
		$CA_{10\text{-}90}$	the rapid burning angle
		CA_{50}	the burn phasing
	$(dX_b/ d\Theta)_{max}$	maximum rate of mass burning rate	
Flame position	-	Flame radius, flame front area, enflamed or burned volume, flame arrival time at given locations	

Matekunas used the maximum pressure to measure cyclic variation because of its ease of measurement and direct relation to the rate of combustion [44] under the rationale that piston motion in the vicinity of TDC is relatively small and a fast (slow) burn rate brings high (low) peak pressure. However, it has been argued by Heywood [57] and Stone et al. [13] that IMEP is a better metric than the maximum pressure because IMEP is a measure of the work that is produced by the combustion, which directly impacts driveability. The average and CoV values are commonly used indicators; CoV_{IMEP} is calculated by equation (2.36). Heywood noted that downgraded vehicle driveability is noticeable when CoV_{IMEP} exceeds about 10 percent [57]; currently a 3% threshold is used for automotive applications.

$$CoV_{IMEP} = \frac{\sigma_{IMEP}}{IMEP} 100\% \tag{2.36}$$

In general, minimal variation of IMEP is found at ignition timing close to MBT [58]. Brown compared the use of average and CoV value of both IMEP and the maximum pressure for a range of ignition timing [58]. It was shown that the average value of the maximum pressure increases as ignition timing advances. For most advanced ignition timing cases, it could be possible that the combustion is terminated before TDC and the maximum pressure is determined by the piston motion.

2.2.1.2 Factors of Cyclic Variation

Sources of the cycle-by-cycle variation in flame speed can be categorized as [8, 9, 59, 60];

1. Chemical factors: equivalence ratio, dilution level, fuel type

2. Physical factors: ignition system, combustion chamber geometry, compression ratio, mixture preparation, engine speed

3. In-cylinder flow effects: intake valve- or port-generated swirl and tumble, and in-cylinder turbulence

Minimum cyclic variations are achieved at slightly rich mixtures, which correspond with the maximum burning velocity [61]. Figure 2.22 shows coefficient of variation of peak pressure as a function of equivalence ratio for two different engine speeds. Experiments were performed at wide-open-throttle using iso-octane. It is seen that minimum variation occurred for slightly rich mixtures for both engine speeds, and there was no significant difference between engine speeds. Young summarized the effect of equivalence ratio on cyclic variation based on a literature survey and concluded that minimum cyclic variation, for all indicators, were observed with a slightly rich mixture, Φ=1.1 to 1.25 [8]. For a better efficiency, lean combustion is favored, therefore, measures to decrease the cyclic variation are required.

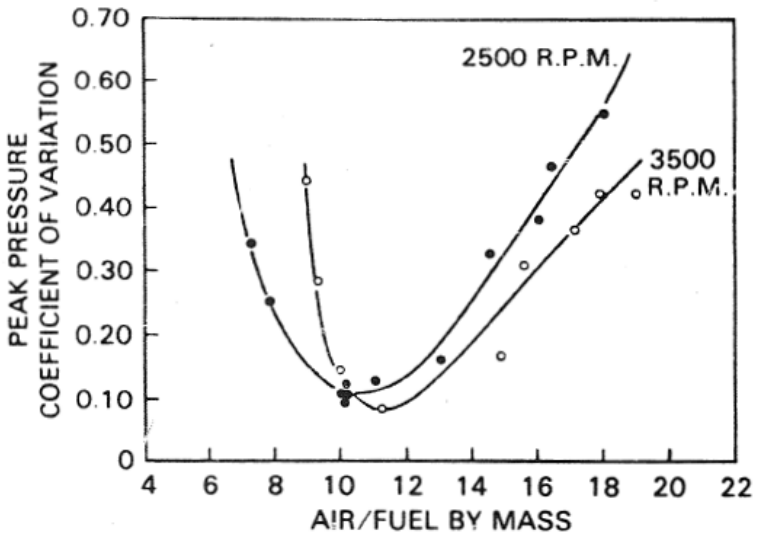

Figure 2.22 COV_{Pmax} versus equivalence ratio for two engine speeds [10]

The effect of charge dilution was investigated by several authors by changing the amount of EGR, skip-firing, adding inert additives and adjusting the throttle position [7, 10, 62]. The dilution effect on cyclic variation, either by excess air or increased EGR, increases cyclic variation by decreasing the burning velocity, i.e. it has the same effect as varying equivalence ratio.

The ignition system affects cyclic variation by determining the initial flame kernel development, which also affects the overall burning speed. Young concluded that the spark gap location, number of ignition points and spark timing affect cyclic variation while the spark energy, spark duration, spark gap spark jitter and electrode shape have little effect [8]. These conclusions were partially disproved by investigations conducted later [9].

The effects of ignition system and spark plug type were investigated by Pischinger and Heywood [56]. Figure 2.23 shows the effects of spark timing and spark type on COV_{IMEP} by using a standard and shrouded intake valve. The cyclic variation was minimized in the vicinity of MBT timing for all spark plug types. The spark plug type was found to have less effect on cyclic variation than the ignition timing. Using a shrouded-valve, the differences in cyclic variations

were even smaller than for the standard valve. Other spark plug design-related factors, such as the spark discharge characteristic, spark plug electrode shape, spark plug number and location are all related to burning rate. To reduce cyclic variation, longer spark discharge duration, higher discharge energy, increased number of spark plugs are favorable because they promote burning rate during the early flame development.

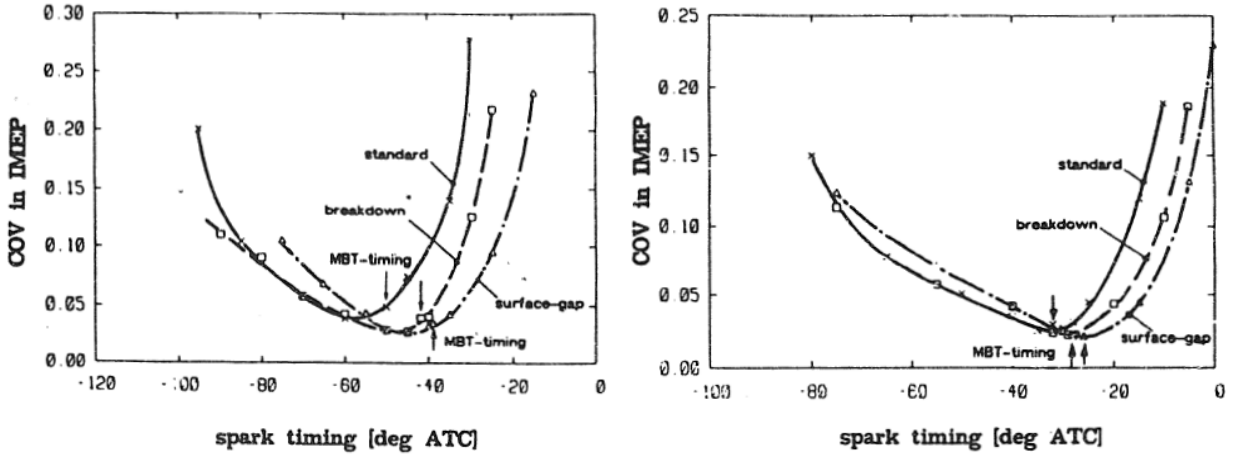

(a) Base type valve

(b) Shrouded type valve

Figure 2.23 COV_{IMEP} as a function of ignition timing for three different spark plugs [56]

The effect of increased engine speed is generally reported as producing higher cyclic variations [8]. It is assumed that increased turbulence due to increased engine speed contributes to higher flame speed variations. The compression ratio affects cyclic variation by its role on the trapped residual fraction. Winsor and Patterson found lower peak pressure variations at higher compression ratios [11].

It is normally assumed that a more homogeneous mixture would result in smaller cyclic variation. However, experiments performed using skip-firing and adding external dilution did not show a significant cause and effect relation with the mixture preparation [11]. Later, it was found

that non-homogeneous mixtures with higher burning velocity could result in lower cyclic pressure variations than well mixed, homogeneous mixtures [36, 63].

2.2.2 Cyclic Variation Modeling

2.2.2.1 Semi-empirical turbulence model

Semi-empirical turbulent cyclic variation models have been developed to relate combustion variations to early flame velocity variations in the vicinity of the spark plug. The basis for each model was that the initial flame development plays a major role for the combustion variations.

All of the models that employ a turbulent-entrainment, or eddy burn-up model are based on the work done by Blizard and Keck [64] and Tabaczynski et al. [58]. The model is a phenomenological, thermodynamic two-zone combustion model that is based on mixing length theory and two parameters: a turbulent entrainment speed and characteristics eddy radius. The effect of the intake-generated turbulence on burning rate is predicted and compared to the experimental results in Figure 2.24. The burn rate is calculated from the equation (2.37) and (2.38), which are slightly modified by different studies.

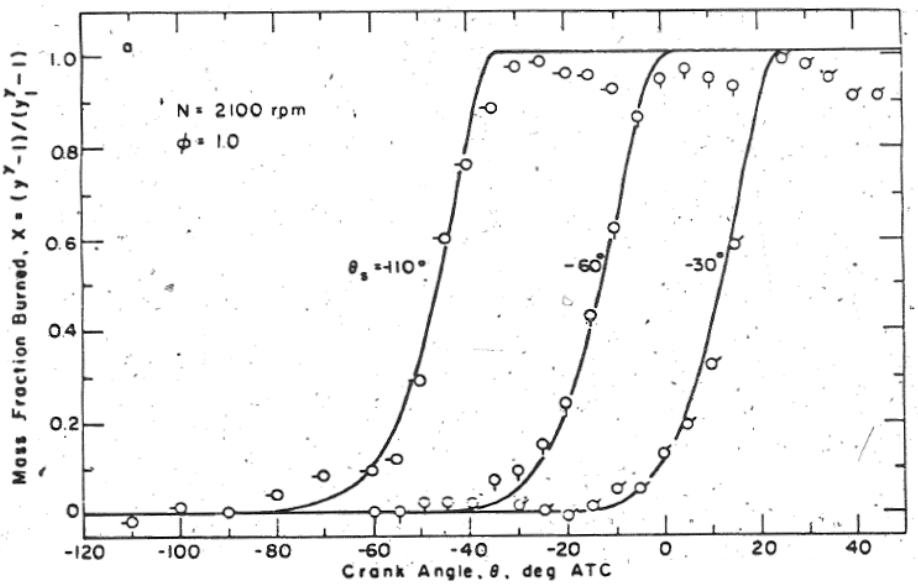

Figure 2.24 Mass fraction burned of experiments and model best fit [64]

$$\frac{dm_e}{dt} = \rho_u A_f \left(\alpha \sqrt{\frac{\rho_u}{\rho_b}} u' \left(1 - e^{-\frac{r_e}{r_c}} \right) + S_L \right) \tag{2.37}$$

$$\frac{dm_b}{dt} = \frac{m_e - m_b}{\tau_c} + \rho_u A_f S_L \tag{2.38}$$

m_e is the total mass entrained by the flame

m_b is the total burned mass

ρ_u, ρ_b are the densities of the unburned and burned gases

A_r, r_f are the area and radius of a spherical flame front required to entrain me

r_c is the order of the integral length scale

u' is the turbulence intensity

S_L is the laminar flame speed

τ_c is the chemical time for eddy burn-up

α is a constant

Barton et al. developed a model describing the gas velocity variations in the vicinity of the spark plug during the initial burn duration [65]. It was assumed in the model that the duration between the ignition timing and first 5% mass burn determines the cyclic variations in the

combustion process. The rate of change of the burned volume for constant volume combustion is expressed in equation (2.39) as,

$$\frac{dV_b}{dt} = A_f S_l E f(u) \tag{2.39}$$

where,

V_b is the volume of burned gas

A_f is the flame front area

S_l is the laminar burning velocity

E is expansion ratio = $T_b M_u / T_u M_b$

$f(u)$ is an unknown function, which represents the dependence of laminar flame speed

Assuming a hemispherical burning shell of radius r_b and constant values for expansion ratio E and $f(u)$ during initial flame development will give the volume burned in the time t_b as equation (2.40). By assuming a constant relative burned volume at the end of the initial burn period, the laminar burning velocity at time t_b was obtained as equation (2.41), where the subscript i refers to conditions existing at the time of ignition. $S(x)$ is the standard deviation of the variable x. Figure 2.25 shows a good agreement between initial burn duration and the variation at the end of the initial burn period, which the correlation factor was 0.975. Later, Young commented about the unknown function f(u) as equation (2.42), which was based on the combustion experiment using hot-wire velocity data [8].

$$V_r = \frac{V_b}{V_i} = \frac{2}{3}\pi S_b^3 E^3 f^3(U) \left. t_b^3 \right/ V_i \tag{2.40}$$

$$\left[\frac{S(t_b)}{S(u_i)}\right] = C_3 \left[\frac{v^{1/3}}{E S_b}\right]_i \frac{1}{f^2(u)} \frac{df(u)}{du} = C_3 \left[\frac{v^{\frac{1}{3}}}{E S_b}\right]_i g(\bar{u}_i) \tag{2.41}$$

$$\frac{1}{f^2(u)} \frac{df(u)}{du} = \left(\frac{1}{\bar{U}_i}\right)^{1.3} \tag{2.42}$$

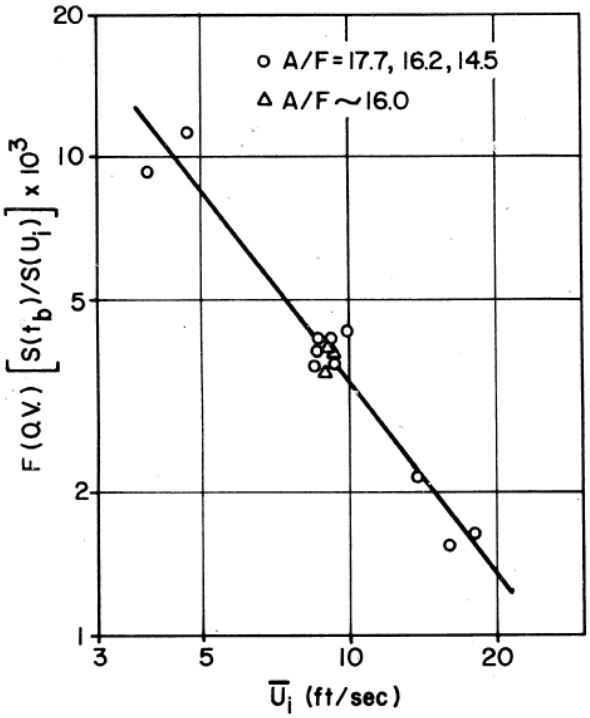

Figure 2.25 Correlation of initial burn duration and velocity variations [65]

Winsor and Patterson developed a model relating mixture velocity and its variations to combustion velocity variations [11]. In this model, it is assumed that the average flame velocity is sensitive to the local turbulent velocity until the flame kernel grows to a critical period t_c and critical range, d_c. The variations in the cyclic combustion were related to the velocity variations by assuming both the turbulent velocity and the flame speed have a certain average value. For a given cycle,

$$d_c = v_f t_c \tag{2.43}$$

where, v_f is an average flame speed during the critical period. Equation (2.43) was differentiated with respect to the turbulent velocity (u), by assuming the constant critical distance for each cycle.

With further assumptions that combustion variations occur during the critical period and there is a linear increase of the turbulent velocity and the turbulent flame speed with the engine speed, the final expression of the burn time variation is stated in equation (2.44). The average flame speed during the critical period ($\bar{v}_f$) was estimated from dividing the total flame travel distance across the combustion chamber (D) by the total burning time ($\bar{t}_b$). Figure 2.26 shows a good agreement between the mean burn duration and burn time variation for different operating conditions.

$$s(t_b) = \frac{d_c}{\bar{v}_f}\frac{S(u)/\bar{u}}{1+[S(u)/\bar{u}]^2} = \frac{d_c}{D}\bar{t}_b\frac{S(u)/\bar{u}}{1+[S(u)/\bar{u}]^2} \tag{2.44}$$

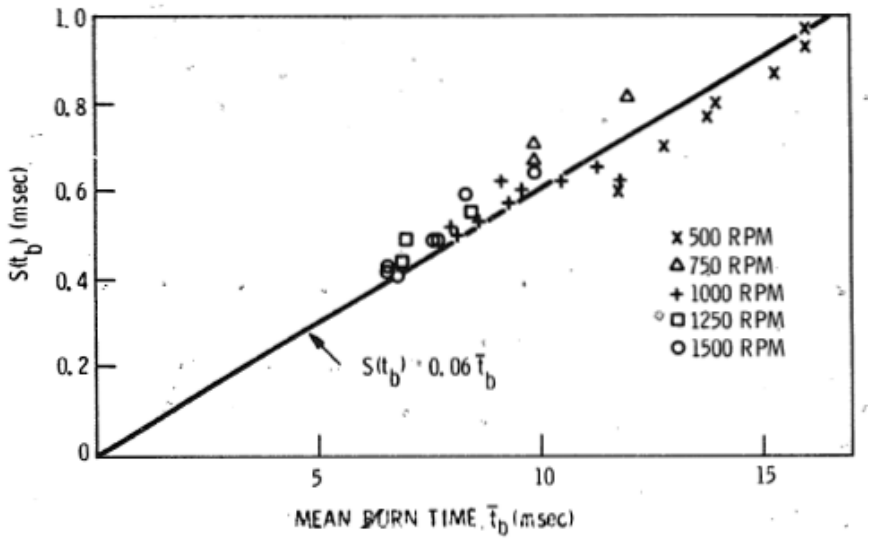

Figure 2.26 Burn time variations versus mean burn time [11]

Stone et al. assumed that the flame kernel displacement plays a major role for the combustion variations. The turbulent combustion model was modified to vary the ignition sites, which are shown in Figure 2.27 (a). Flame kernel displacement was modeled by moving the ignition point to different sites arbitrarily. The model was validated by comparing model calculated and experimental results of the mean combustion parameter. An average of 8

locations in Figure 2.27 (a) was used to calculate average model result. It was noted by Stone et al. that the goal of the study was investigating the effect of flame kernel displacement on combustion variation using a phenomenological turbulent combustion model. Since the research had no actual data of the early flame development, an arbitrary selection of the ignition sites was made to compute combustion variation. The model effectiveness was evaluated by comparing experimental results and the model predicted values of COV_{IMEP} and following combustion durations: 0-10% burn, 0-50% burn and 0-90% burn. Figure 2.27 (b) shows reasonable agreement of COV_{IMEP} values between experimental and model predicted results. This agreement was also found for different cyclic variation parameters. Most significant disagreement was found with the slow laminar burning mixtures (weak mixtures at full throttle or any of the mixture strengths at part load), which the maximum pressure is determined mostly by the compression stroke rather than combustion.

(a)

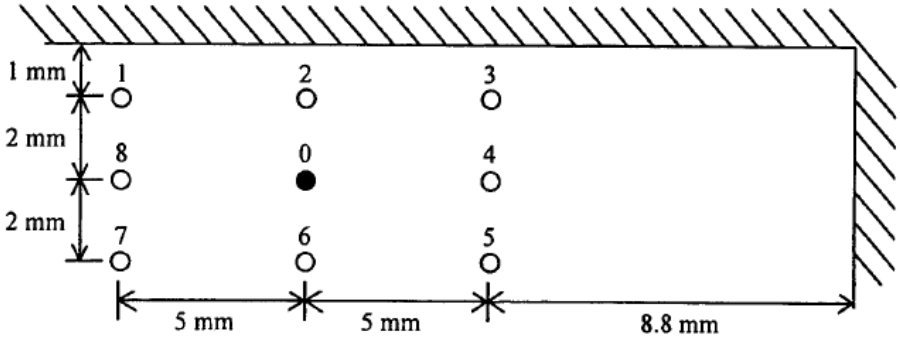

(b)

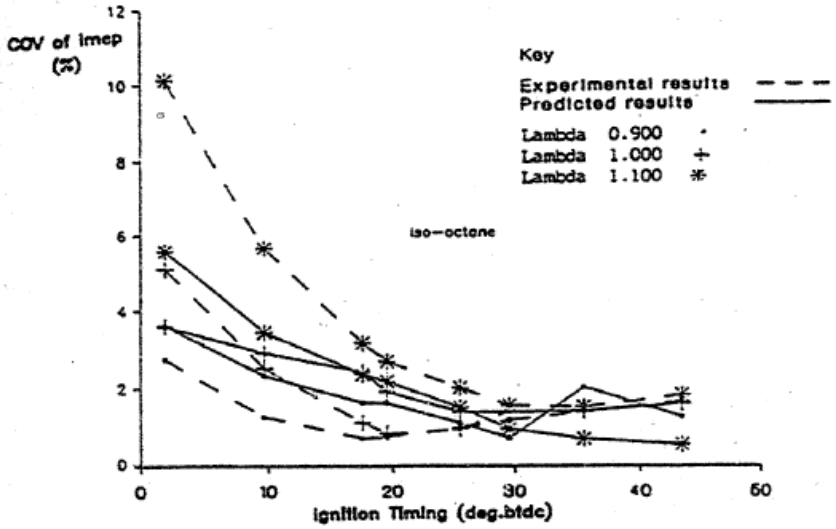

Figure 2.27 Assumed distribution ignition sites and CoV_{IMEP} of predicted and measured cycle-by-cycle variations [13]

Further improvement of the turbulent entrainment model was reported by Brehob and Newman [66]. The General Engine Simulation (GESIM) code was coupled with a Monte-Carlo simulation to calculate the distribution of cyclic variations by using the prior cycle residuals as an input condition for the following cycle. To induce cyclic variation in the model, the turbulence integral length scale r_c, flame kernel offset from the spark plug and the constant α were varied randomly from equation (2.37) and (2.38). The turbulence integral length scale determines the early burn period by defining the position of the wrinkled flame front. The flame kernel offset influences the later stages of combustion and the parameter α influences the rate of turbulent flame propagation. Experimentally determined average and standard deviation for those three

parameters were perturbed randomly as input conditions for GESIM. The cyclic variation computed by the model was quantified by burn duration (0-2%, 0-10% and 0-90% mass burn), location of the peak pressure, peak pressure and IMEP. The frequency distributions of the cyclic variation are shown in Figure 2.28. The average and standard deviation values calculated by Monte-Carlo simulation were compared to the experimental values to validate the model. It was found that r_c affects early burn and offset late burn while α affects all the combustion related parameters.

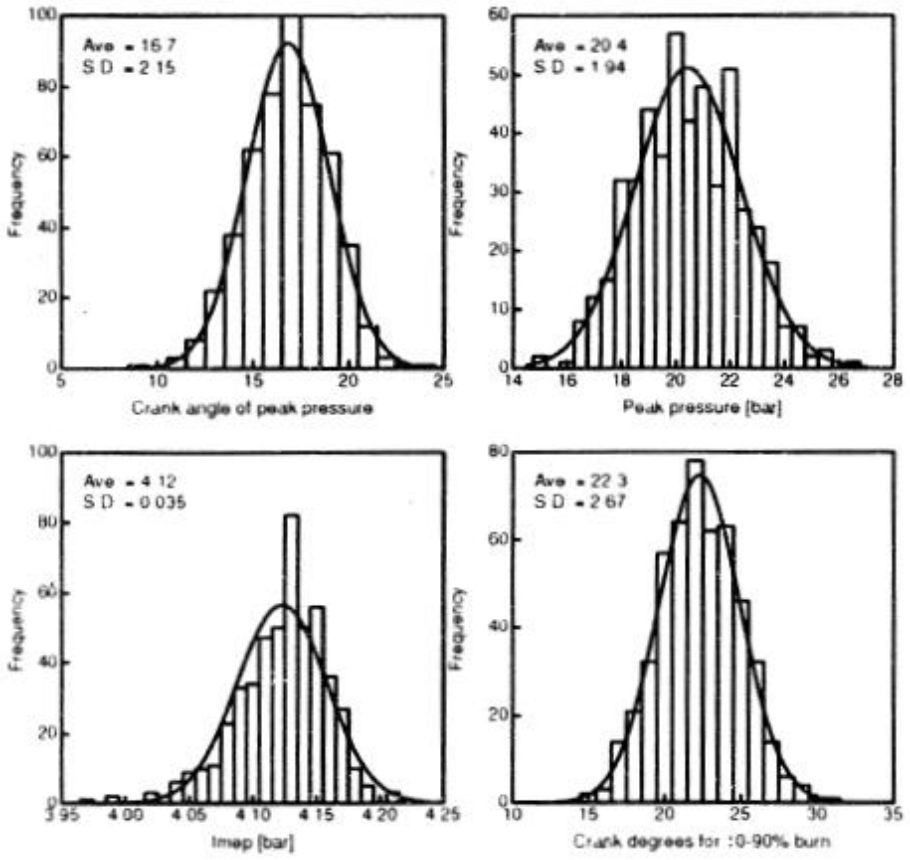

Figure 2.28 Flame center offset α and r_c randomly perturbed for 500 cycles [66]

2.2.2.2 Detailed turbulence model

Recently, cyclic variation have been studied using full-CFD, large eddy simulation (LES) coupled with detailed chemical kinetics model to calculate the differences in the flow field during combustion. Enaux et al. used multi-cycle LES model to reproduce the cyclic combustion variability for 25 consecutive cycles [67]. The LES model was validated by comparing the in-cylinder pressure envelope between the experimental and model results. It was found that velocity fluctuations near the spark plug, which induce variations of the early flame kernel growth and the overall combustion, plays the most important role in cyclic variations while the effect of the local dilution ratio or the temperature at ignition timing revealed a weak correlation. Figure 2.29 shows the differences in velocity vectors in a cut plane through the spark plug at ignition timing for three cycles. The CPU time for the model was approximately 1.4 day per cycle on 400 processors.

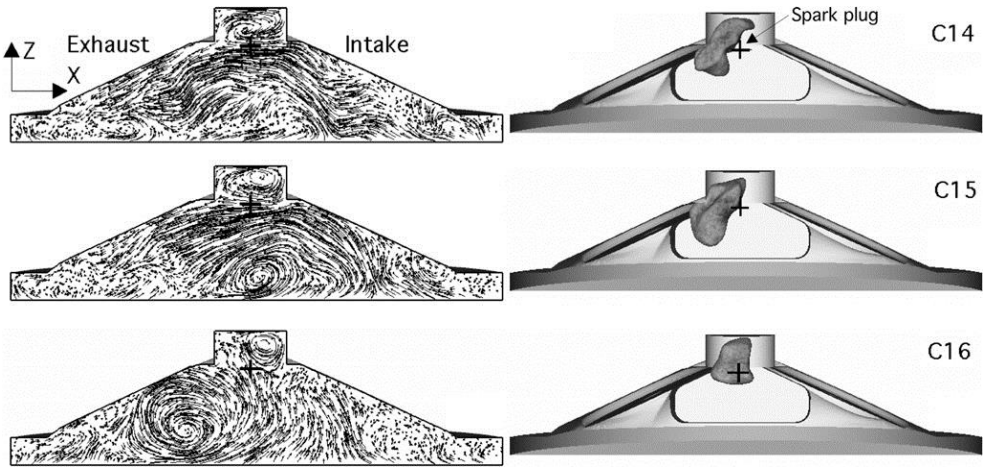

Figure 2.29 Velocity vector at spark timing in a cut plane through the spark plug and iso-surface of progress variable c=0.5, 5 CAD after ignition [67]

Goryntsev et al. used an LES model to investigate the impact of the air-fuel mixing process on cycle-to-cycle variations in DISI IC engines [68]. Consecutive studies conducted by Goryntsev

et al. include validating KIVA-3V-LES code with direct numerical simulation [40, 69, 70] and extending the work to fuel spray injection-driven flow. The spray module was based on the 3-dimensional CFD-code KIVA-3V. To characterize cyclic variation, the fuel spray angle was varied randomly as 40º, 50º and stochastic variations in the range of 40±3º with the fuel thickness of 12.5º. Figure 2.30 displays the instantaneous and averaged profile of the cyclic variation for velocity (a,c) and temperature (b,d) for 32 consecutive cycles. Though use of full-CFD calculation provides the most accurate results with spatial distribution in the combustion chamber, its use for modeling the cyclic variation is limited due to the relatively large amount of computing power required to calculate number of cycles to validate the model convergence.

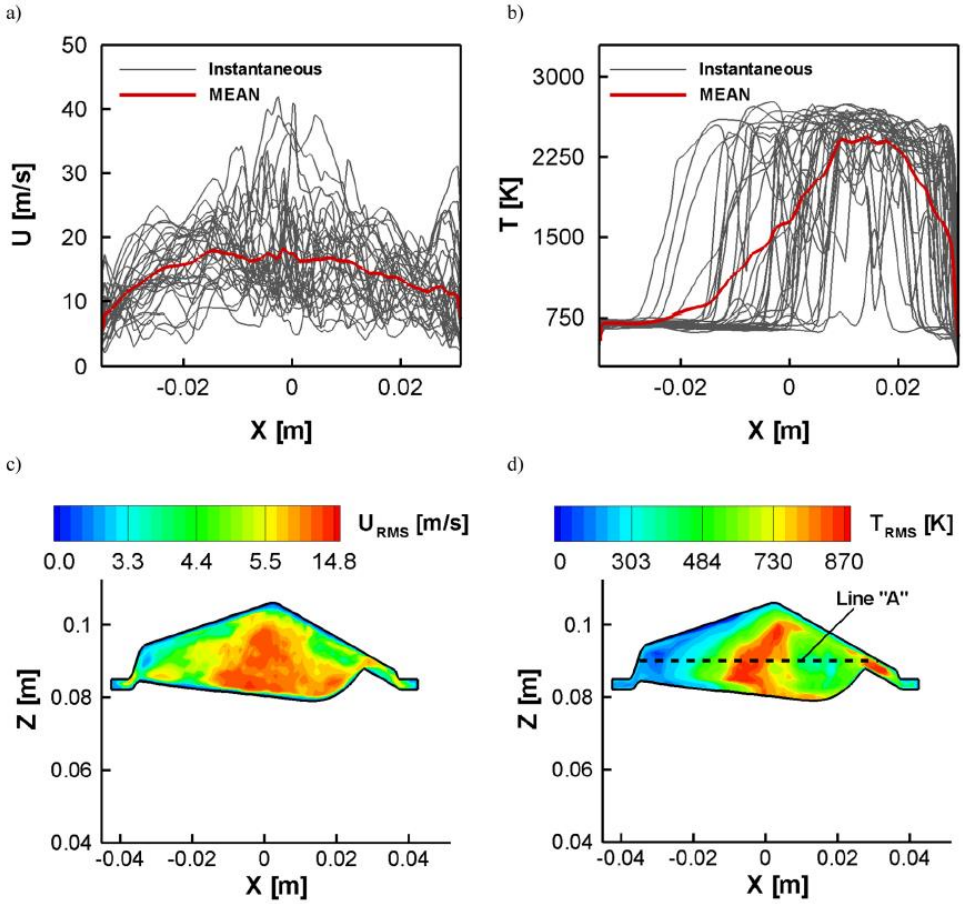

Figure 2.30 Instantaneous and mean profiles and standard deviation of in-cylinder velocity and temperature in the cross section of the combustion chamber at 15 º bTDC of 32 consecutive cycles [70]

2.2.2.3 Other approaches

A non-linear regression model was suggested by Dai et al. to practically model and predict cyclic variation for different operating conditions [71]. Seven independent parameters, RPM, IMEP, equivalence ratio, residual mass fractions, CA0-10, CA10-90 and CA50 were used to find a non-linear regression model from 6000 data points from 13 engines. The model predicts CoV_{IMEP} as a function of 7 parameters listed above. In Figure 2.31, a good agreement between the predicted and measured CoV_{IMEP} is shown except when experimental CoV_{IMEP} value is larger than 10%. Each data point represents the CoV_{IMEP} value of different operating condition. This approach provides practical guidance of predicting the CoV_{IMEP} and the effect of the parameters on the overall cyclic variations.

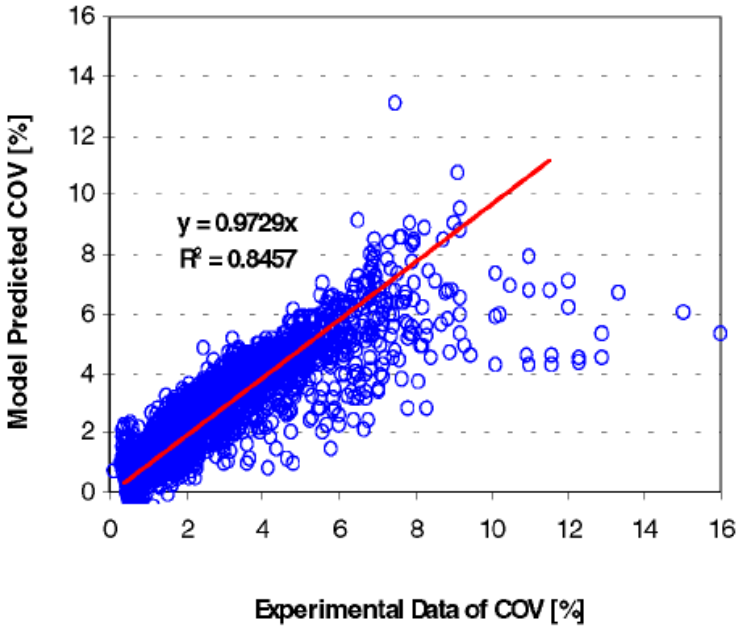

Figure 2.31 Non-linear regression model CoV_{IMEP} compared to experimental results [71]

Bozza et al. suggested that the initial pressure of each cycle was randomly perturbed from the average value as shown in equation (2.45) [72]. The range of random variation, *xband*, was

adjusted to find the optimum value for every different operating condition. A quasi-dimensional turbulent combustion model was developed to calculate the pressure trace. Figure 2.32 shows experimental and the model-calculated in-cylinder pressure traces for 94 cycles. The parameter x_{band} was optimized to have a good match of the pressure spread, shown in the PDF plot of the normalized IMEP. It was claimed by Bozza et al that a statistically equivalent pressure data could be obtained by using this method. However, use of this method is limited to optimizing the parameter x_{band}. Though the PDF of normalized IMEP matched well, the spread of peak pressure between experiment and calculation shows significant differences. A larger number of cycles is required to confirm the convergence of the random perturbation.

$$P_i = P_{i,av} * rnd(1 \pm x_{band}), \quad i = 1,5 \tag{2.45}$$

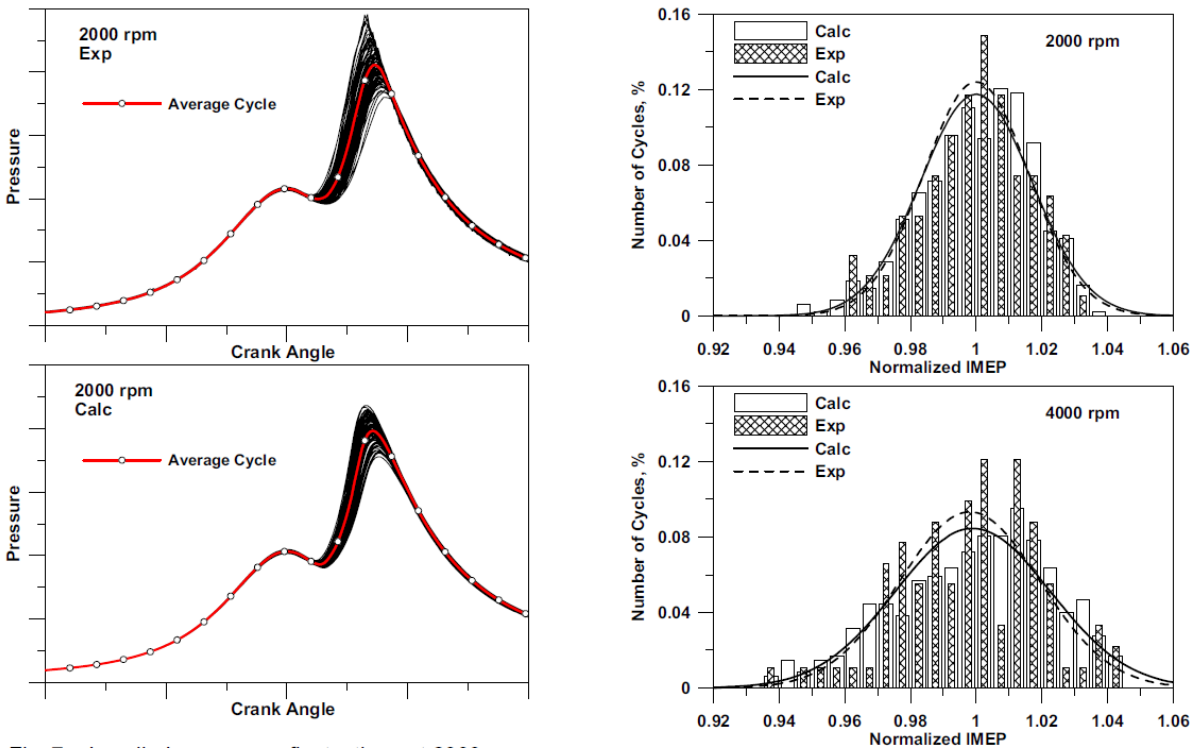

Figure 2.32 In-cylinder pressure fluctuation and probability density function of experiment and calculation [72]

2.3 Wiebe Function

The Wiebe function, which is shown in equation (2.46), is an analytical function that can be used to characterize the burn rate in spark ignition engines in a feasible way. The Wiebe function is a four-parameter expression that gives an 'S' shape curve and has been widely used to characterize the cumulative mass burn fraction of the fuel. The Wiebe function can be used with different combustion systems and fuels including classical spark ignition engines, gasoline direct injection (GDI) engines, homogeneous charge compression ignition (HCCI) and premixed charge compression ignition (PCCI) engines [73].

$$X_b = 1 - \exp\left[-b\left(\frac{\theta-\theta_{ig}}{\theta_{comb}}\right)^{m+1}\right] \tag{2.46}$$

A combustion event consisting of many chemical reactions can be classified as an elementary process, which includes reactions of hydrogen forming water, and an effective reaction, which is the carbon monoxide oxidation reaction. Figure 2.33 shows the elementary and effective reactions and its schematic diagram as a function of time. Wiebe postulated [73] that the incremental change in the number of molecules of the main reactant, *dN*, participating in the effective reaction in the time interval from *t* to *t* + *dt* is directly proportional to the change in the number of effective reaction centers, N_e, *i.e.*, dN_e-$dN = ndN_e$, where *n* is the constant of proportionality as shown in equation (2.47).

$$-\left(\frac{dN}{dt}\right) = n\left(\frac{dN_e}{dt}\right) \tag{2.47}$$

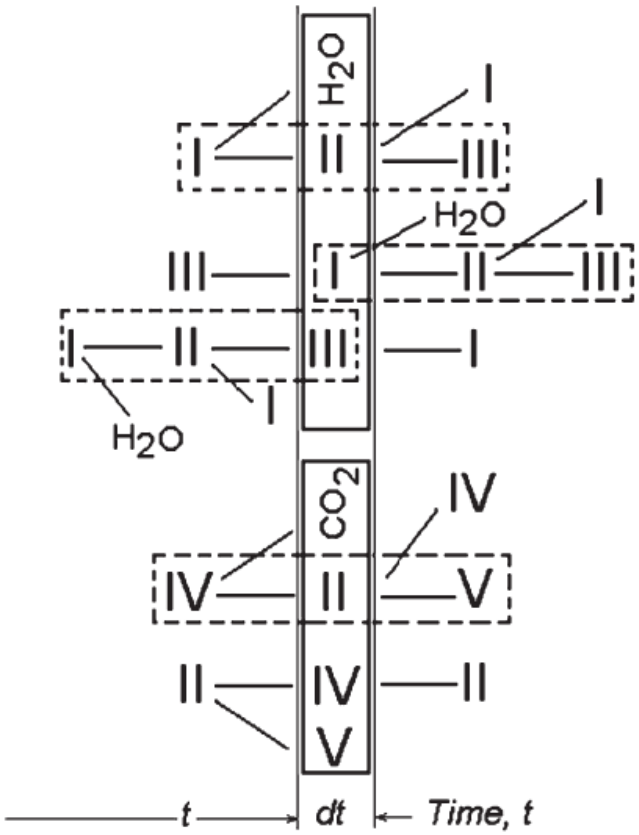

(a)

Elementary process	
Reaction I	$OH + O_2 = H_2O + H$
Reaction II	$H + O_2 = OH + O$
Reaction III	$O + H_2 = OH + H$

Effective reaction	
Reaction IV	$OH + CO = CO_2 + H$
Reaction II	$H + O_2 = OH + O$
Reaction V	$O + CO = CO_2$

(b)

Figure 2.33 Schematic diagram of elementary and effective chemical processes and chain reactions as a function of time [73]

Defining the relative ratio of the effective centers in the time interval *dt* as $\rho \equiv \left(\frac{dN_e}{dt}\right)/N$ and rewriting equation (2.47) as

$$\ln\frac{N}{N_0} = -\int_0^t n\rho dt \tag{2.48}$$

$$\frac{N}{N_0} = exp\left[-\int_0^t n\rho dt\right] \tag{2.49}$$

where N_0 is the number of moles of the main reactant at start of reactions. The overall burned fraction at time *t* can be defined as

$$X_b = \frac{N_0 - N}{N_0} \tag{2.50}$$

Then

$$X_b = 1 - \frac{N}{N_0} = 1 - exp\left[-\int_0^t n\rho dt\right] \quad (2.51)$$

$$\frac{dX_b}{dt} = \mathrm{n}\rho exp\left[-\int_0^t n\rho dt\right] = \rho\mathrm{n}(1 - X_b) \quad (2.52)$$

If the relative density of the effective centers can be expressed as $\rho = kt^m$, where *k* and *m* are constants, and if *nk* = *K*, equation (2.52) can be rewritten as

$$\frac{dX_b}{dt} = \mathrm{K}t^m exp[-\{K/(m+1)\}t^{m+1}] \quad (2.53)$$

$$X_b = -exp[-\{K/(m+1)\}t^{m+1}] \quad (2.54)$$

where Wiebe named the parameter *m* as a 'combustion characteristic exponent'. Consider a completed combustion event at time θ_{comb}, the burn fraction becomes

$$X_{comb} = 1 - \exp\left[-\{K/(m+1)\}{\theta_{comb}}^{m+1}\right] \quad (2.55)$$

Similarly at any time θ from the ignition timing,

$$X_b = 1 - \exp\left[-(K/(m+1))\left(\theta - \theta_{ig}\right)^{m+1}\right] \quad (2.56)$$

Taking the logarithm of equations (2.55) and (2.56) and dividing one by the other yields,

$$X_b = 1 - \exp\left[-\mathrm{b}\left[(\theta - \theta_{ig})/\theta_{comb}\right]^{m+1}\right] \quad (2.57)$$

Where $\mathrm{b} = -\ln(1 - X_{comb})$. Note that X_{comb} value of 0.985 corresponds to the value of Wiebe function parameter *b* around 4.19, which explains the reason why a generally accepted value for Wiebe function parameter *b* is close to 4.

To verify the combustion characteristic exponent, *m*, find the 1st and 2nd derivative of the Wiebe function as a function of time (θ) as shown in equations (2.58) and (2.59).

$$\frac{dX_b}{d\theta} = \frac{\boldsymbol{b(m+1)}}{\theta_{comb}}\left(\frac{\boldsymbol{\theta - \theta_{ig}}}{\theta_{comb}}\right)^{\boldsymbol{m}} exp\left[-b\left(\frac{\theta - \theta_{ig}}{\theta_{comb}}\right)^{m+1}\right] \quad (2.58)$$

$$\frac{d^2X_b}{d\theta^2} = \frac{\boldsymbol{b(m+1)}}{\theta_{comb}} exp\left(-b\left(\frac{\theta-\theta_{ig}}{\theta_{comb}}\right)^{m+1}\right)\left[-\frac{\boldsymbol{b(m+1)}}{\theta_{comb}}\left(\frac{\boldsymbol{\theta-\theta_{ig}}}{\theta_{comb}}\right)^{\boldsymbol{2m}} + \frac{\boldsymbol{m}}{\theta_{comb}}\left(\frac{\theta-\theta_{ig}}{\theta_{comb}}\right)^{m-1}\right] \quad (2.59)$$

At the condition where mass burn fraction (dX_b) is at the maximum, $\frac{d^2X_b}{d\theta^2} = 0$, should be satisfied. Then,

$$\left[\left(\frac{\theta-\theta_{ig}}{\theta_{comb}}\right)^{m+1}\right] = \frac{m}{b(m+1)} \quad (2.60)$$

Plugging in equation (2.60) in to equation (2.46) gives

$$X_{b@dXb,max} = 1 - exp\left[\frac{-m}{m+1}\right] \quad (2.61)$$

It is shown in equation (2.61) that the burn fraction at the maximum burning rate is only a function of the combustion characteristic exponent, *m*. For a typical combustion profile, where $X_{b@dXb,max} \approx 0.5$, the value of *m* is about 2.25. Based on equation (2.61), a relatively slow burning cycle with $X_{b@dXb,max} \approx 0.55$ and relatively fast burning cycle with $X_{b@dXb,max} \approx 0.45$ will give the value of *m* about 3.96 and 1.49.

Chapter 3 Experimental Configuration

Experiments and data analysis were performed to investigate knock statistics. Engine in-cylinder pressure data were collected and the combustion profile was analyzed to determine the thermodynamic conditions at knock onset and understand the statistical distribution of knock event characteristics. This chapter discusses the experimental configuration, data collection and analysis tools that were used for knock investigation in this research.

3.1 Engine Specifications and Data Acquisition

Experiments were performed on a 3-cylinder outboard marine engine [74]. Specifications of the engine and fuel are listed in Table 3-1. Figure 3.1 shows the shape of a combustion chamber and the locations of pressure transducer and spark plug. The shape of the combustion chamber is not close to a pent roof type and the location of the spark plug is skewed from the center due to the limited area of installation.

Table 3-1: Outboard marine engine specification

HP / kW @ Prop	40 / 29.4
Max RPM (WOT)	5500-6000
Cylinder/Configuration	3 (in-line)
Displacement [cm^3]	747
Bore & Stroke [mm]	65 × 75
Compression Ratio [-]	9.73
Air Induction System	2-Valve per Cylinder, Single Overhead Cam
Mixture Preparation	Port fuel injection
Octane	85

Engine tests were run at a range of speeds (1650, 1900, 2200, 2600 and 2900 RPM), loads of 25, 50, 75 and 95%, AFRs of 13:1, 14:1, 15:1 and 16:1, and over the full range of ignition timing,

i.e. from not knocking to heavily knocking. AFR was monitored with a Bosch LSU 4.2 wideband O2 sensor, installed at exhaust pipe. The engine was controlled by two ECUs, the engine ECU and the lab-control ECU. The engine ECU allows ignition timing and AFR to be locked and offset. The data were collected after the ignition timing and AFR for all three cylinders were locked. The lab-control ECU was used to control intake air temperature, coolant temperature and throttle position. Intake air temperature was monitored and controlled using an intake heater to 50^{o}C and the coolant temperature was controlled to 65^{o}C for all test cases.

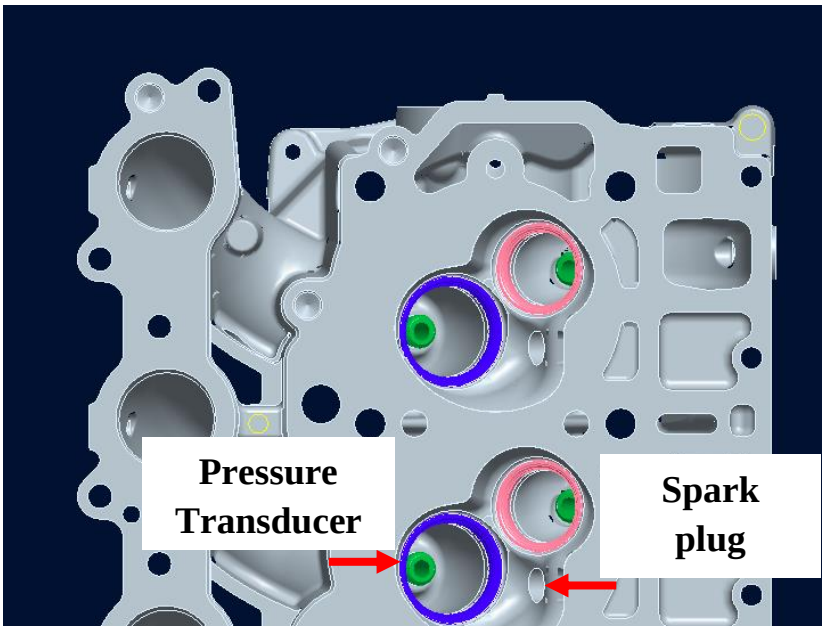

Figure 3.1 Combustion chamber shape and pressure transducer location

The mass of fuel, was determined from fuel per cycle data collected at the engine ECU. The data were collected at 50 ms frequency for minimum 30 seconds at each condition and average and CoV values are listed in Table 3-2. It should be noted that the measured fuel mass per cycle from the engine ECU is the measure of the fuel that is injected to the port, which is controlling the overall AFR in a closed-loop control. Because the mass of fuel is not a function of ignition timing,

all the calibration tests were performed at the ignition timing of -25 aTDC. The reference values are the amount of the fuel pre-determined by the engine ECU to maintain AFR for all three cylinders. The mass of fuel for only cylinder #2 was adjusted ±1 mg per cycle to calibrate the uncertainty of the fuel amount. The predicted AFRs listed in the Table 3-2, were calculated by assuming that the amount of air flow is constant, since throttle position was fixed. The total fuel mass was adjusted by changing the fuel amount in cylinder #2. The AFR data were also collected from the engine ECU at 50 ms frequency for minimum 30 seconds and average and CoV values are listed in the Table 3-2. It is shown in the Table 3-2 that predicted and measured average AFR values for ±1 mg cases are closely matched. This implies that the AFR measurements show good accuracy. Based on the assumption that the amount of air is a constant, the variation of AFR should be the result of the uncertainty of fuel mass. For a range of operating conditions, the CoV of fuel mass was determined as 0.11 ~ 0.2%. This corresponds with 0.22 ~ 0.4% uncertainty of the fuel mass with 95% confidence interval.

Table 3-2 Calibration of fuel mass and its uncertainty using O_2 sensor

Speed [RPM]	Load [%], AFR [-]	Fuel per cycle total			AFR predicted [-]	AFR measured by O_2 sensor	
		Fuel mass target per cycle at cyl#2 [mg/cyc]		CoV [%]		Average [-]	CoV [%]
1900	75% AFR15	-1mg	12.82	0.65	13.42	13.45	0.14
		Ref.	13.82	0.62	-	13.09	0.20
		+1mg	14.82	0.65	12.78	12.81	0.14
	95% AFR13	-1mg	15.61	1.10	13.31	13.29	0.13
		Ref.	16.61	1.12	-	13.04	0.13
		+1mg	17.61	1.08	12.78	12.77	0.11
2200	75% AFR15	-1mg	13.18	1.21	14.26	14.27	0.12
		Ref.	14.18	1.18	-	13.92	0.13
		+1mg	15.18	1.21	13.60	13.66	0.13
	95% AFR13	-1mg	16.72	2.39	13.19	13.20	0.12
		Ref.	17.72	2.41	-	12.94	0.13
		+1mg	18.72	2.41	12.71	12.70	0.14
2600	75% AFR15	-1mg	17.07	2.93	13.15	13.16	0.14
		Ref.	18.07	2.90	-	12.91	0.12
		+1mg	19.07	2.95	12.67	12.66	0.15
	95% AFR13	-1mg	12.88	2.41	14.40	14.38	0.16
		Ref.	13.88	0.62	-	14.05	0.16
		+1mg	14.88	2.34	13.72	13.79	0.12

3.2 Pressure measurement and analysis

In-cylinder pressure was measured with a Kistler 6125B transducer and a Kistler 5010B charge amplifier installed in the 2nd cylinder. The intake runner pressure was measured using a Kulite XT-123B-190 absolute pressure transducer for pegging the in-cylinder pressure. The signals were collected using a National Instrument NI PCI-6143 DAQ through a NI BNC 2110 shielded connector block. The data were collected at a fixed sampling frequency of 200 kHz; a minimum of 5,000 consecutive cycles were acquired for all cases.

The in-cylinder pressure data were low-pass filtered to remove noise and high-frequency pressure oscillation associated with engine knock. The in-cylinder pressure were high-pass filtered

by subtracting the low-pass filtered data from the raw data. The Butterworth filter, which is widely accepted with its simplicity and acceptable performance, was used in low-pass filtering. The performance of a Butterworth filter depends on the selection of the cut-off frequency, which assumes the raw signal to be stationary and is unable to process non-stationary signals [75, 76]. Figure 3.2 shows the raw and low-pass filtered in-cylinder pressure of a single cycle with severe knock. It is seen in the Figure 3.2 (a) that low-pass filter removes high-frequency noise successfully. However, Figure 3.2 (b) shows over-estimated in-cylinder pressure by the low-pass filter around knock onset, where the signal is non-stationary. Because of the bias from the low-pass filter, the knock onset and MAPO knock intensity will be determined by analyzing the raw pressure data directly, as discussed in Chapter 4.

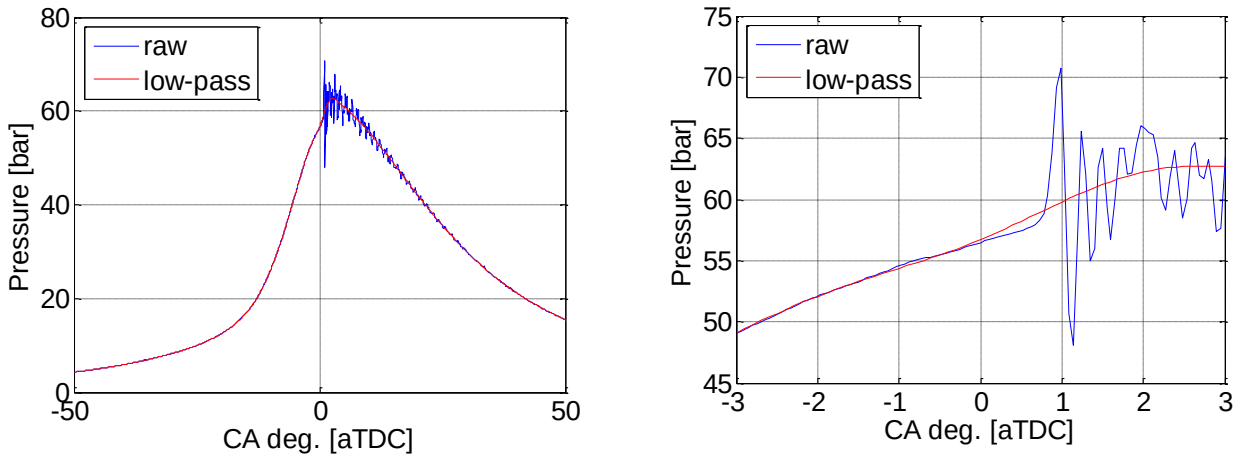

Figure 3.2 Raw and low-pass filtered in-cylinder pressure at 1900RPM, 95% load, AFR13 and ignition timing -35 aTDC

The time-based raw data were spline-fitted and interpreted at a fixed crank angle resolution to be handled with ease in an automated code. The length of each cycle varies even at a fixed operating speed due to the existence of a cyclic variation, which changes engine speed

continuously. The resolution of the spline-fitted data was selected to be 0.1 CA degree to maintain reasonable accuracy of the in-cylinder pressure. Figure 3.3 shows the comparison of a pressure trace from a single cycle with very high knock intensity. The raw data acquired at resolution of 200 kHz at 1900RPM is labeled as 5 μs per data point. It is shown in Figure 3.3 that a resolution 0.1 CA degree is required to maintain a reasonable accuracy of the magnitude and frequency of the pressure oscillation after an autoignition. In this research, a constant number of 0.1 CA degree resolution was used to fit the raw data. The low-pass filter will be applied to the 0.1 CA degree fitted data to calculate heat release rate and the thermodynamic engine model to determine parameters related to the heat release and the thermodynamic conditions at knock onset. It should be noted that all knock metrics were determined from the raw data to preserve accuracy.

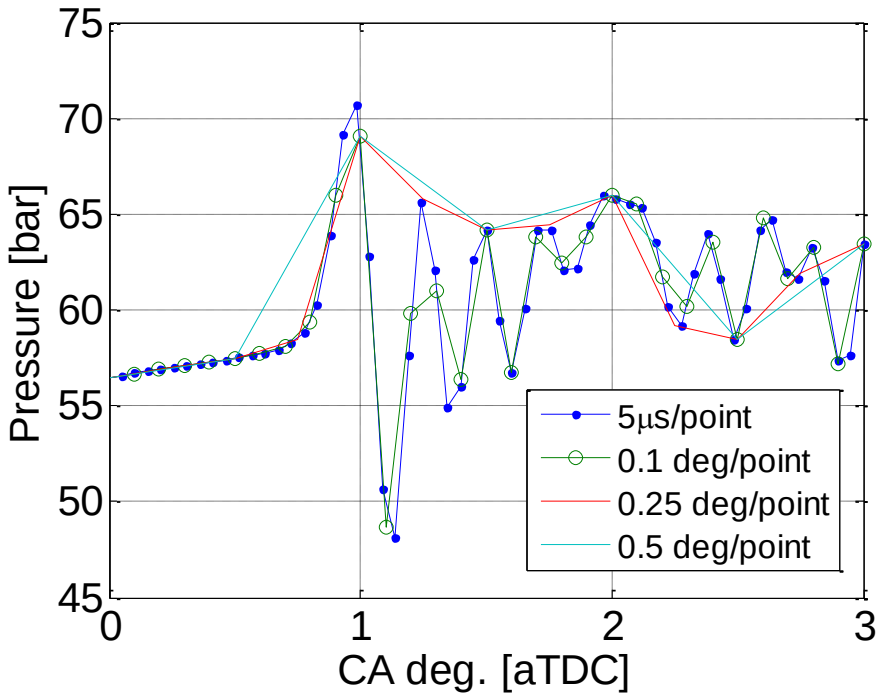

Figure 3.3 In-cylinder pressure comparison at data resolution at 1900RPM, 95%, AFR13 and ignition -35 aTDC

3.3 Thermodynamic Engine Model

A single-zone thermodynamic engine model was developed to calculate the in-cylinder pressure and end-gas temperature as a function of crank angle. The model is effectively the same as that used to calculate heat release, see equations (5.1) – (5.6). The energy release as a function of a crank angle was determined from Wiebe function parameters, which were curve-fitted from cumulative heat release. Details about Wiebe function and curve-fitting will be discussed in Chapter 6. The end-gas temperature was calculated from equation (3.1)

$$\frac{dT_u}{dt} = \left(\frac{\gamma-1}{\gamma}\right)\left[\frac{T_u}{p}\frac{dp}{dt} + \frac{q_u}{m_u R_u}\right] \tag{3.1}$$

where T_u is the unburned end-gas temperature, p is the pressure, q_u is the heat transfer rate, m_u is the unburned mass, and R_u is the unburned gas constant. The measured in-cylinder pressure and predicted temperature at IVC timing were used as initial conditions. The calculation was continued until exhaust valve opening (EVO) timing. The residual mass fraction was calculated using the Yun and Mirsky correlation [77].

Sample predicted results of the in-cylinder pressure and end-gas temperatures are plotted in Figure 3.4. The predicted in-cylinder pressure by the thermodynamic engine model matches the experimental result well. There are differences during expansion stroke, which shows an over-estimated heat transfer effect, however, the model result was reasonably matched. The model predicted pressure will be used to validate the accuracy of calculated heat release and predicted end-gas temperature will be used in knock model to calculate ignition delay. The model's purpose is to estimate conditions at knock onset, so emphasis is placed on accuracy in this time window at the sacrifice of accuracy late in the cycle.

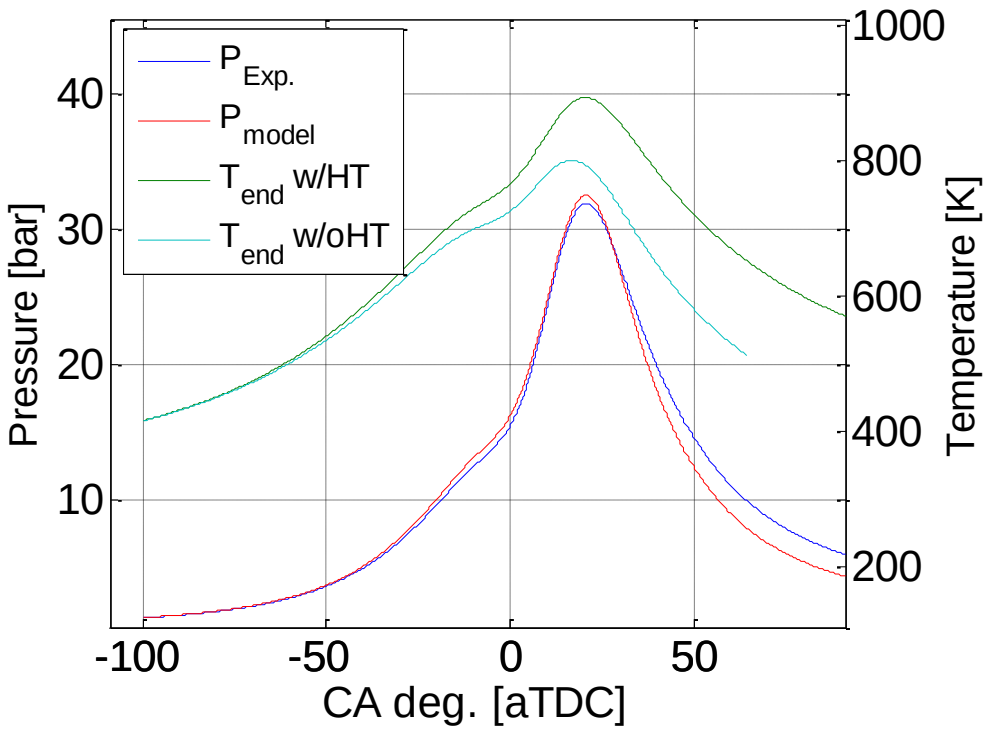

Figure 3.4 Thermodynamic engine model pressure and end-gas temperatures at 1900 RPM, 75% load, AFR14 and ignition timing -15 aTDC

Chapter 4 Engine Knock Metrics

Accurately determining knock onset is a critical step for investigating knock phenomena because the thermodynamic conditions at knock onset help define the ensuing event. If knock onset is determined one crank angle later than the initial pressure rise, the in-cylinder pressure and unburned mass fraction at knock onset can be differ by 5 bar and 0.05, respectively. Determination of knock onset automatically in software rather than manually was a more complicated problem than initially thought. Several methods have been developed and suggested to determine knock onset automatically, which enable handling a large number of cycles.

The most widely used method is the threshold value exceeded (TVE), which filters the raw pressure data using a high-pass filter and determines knock onset as the timing when the high-pass filtered pressure exceeds the pre-determined threshold value. The TVE method generally works with an accuracy of $\pm$0.5 CA deg. for severe knock intensity cycles, however, the errors can be larger for intermediate knock cases, and weak knock cycles will not be detected correctly. Another method of detecting knock onset is the signal energy ratio (SER) method (see Chapter 2.1.1.3), which determines knock onset as the time when the energy ratio increases rapidly by calculating the forward and backward energy contained in the pressure oscillation. Figure 4.1 shows an intermediate (a) and weak (b) knocking cycle and their knock onsets determined by the TVE and SER methods. It is shown in Figure 4.1 (a) that the pressure at knock onset determined by TVE method will be 7 [bar] higher than the SER method, and, visually, both are ~3 [bar] different than when the oscillation actually began, which occurred at TDC. For a weak knock cycle, the TVE-determined knock onset is ~2 CA degrees later than the visually determined knock onset, and ~4 CA degree after the SER-determined knock onset. In general, the SER-determined knock onset is always 2~3 CA degrees before the actual knock onset.

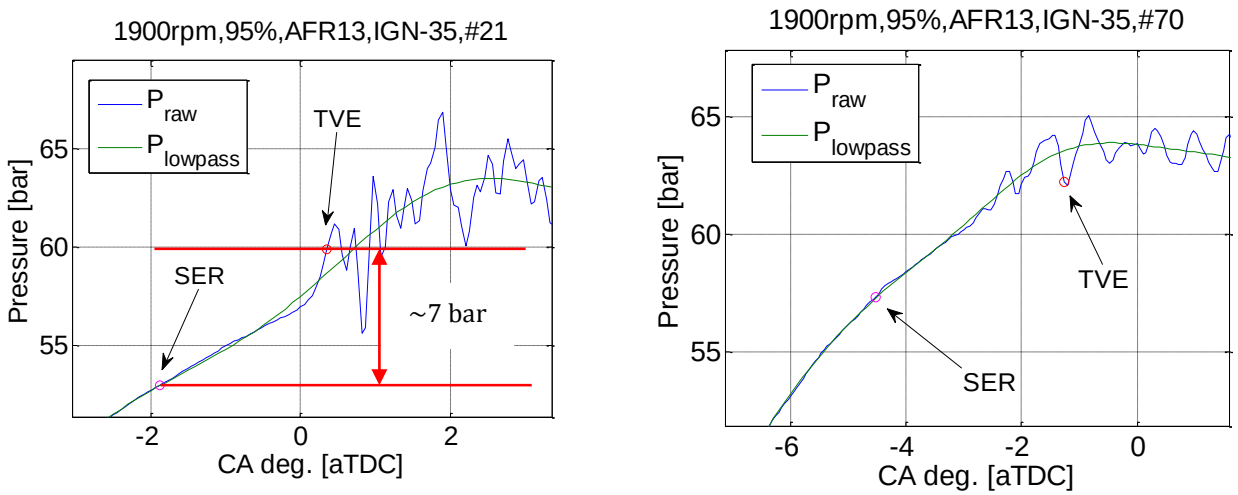

(a) (b)

Figure 4.1 In-cylinder pressure and detected knock onset(TVE and SER) at 1900RPM, 95%, AFR13 and ignition timing -35 aTDC

Inaccuracy of the TVE method is mostly due to a bias associated with the low-pass filtering. Figure 4.2 show a single-cycle raw and filtered pressure data along with the knock onsets determined by the TVE and SER methods. It is shown in the figure that the SER method determines a knock onset far advanced from the initial pressure rise, which occurred around -2.3 aTDC. The TVE-determined knock onset is at -2.6 aTDC, which is about 0.3 CA degree before the initial pressure rise. It is seen in Figure 4.2 (b) that the high-pass filtered pressure exceeds the threshold value at -2.6 CA degree, before the initial pressure rise, because of a bias resulting from high-pass filter. A dip is seen in the high-pass filtered data between -3.3° and -2.2 ° aTDC, which is a bias due to the filter. This is also seen in the low-pass filtered pressure data; from -3.3 ° to −2.3 ° CA, the low-pass filtered data exceeds the experimental data because of the influence of the higher pressures after knock onset that 'bleed' through the filter. As a result, the TVE-determined knock onset for severe knock intensity cycles is inaccurate due to the bias of high-pass filtered pressure; inaccuracies in determining weak and intermediate knock cycles are mostly due to the failure of setting an arbitrary threshold value.

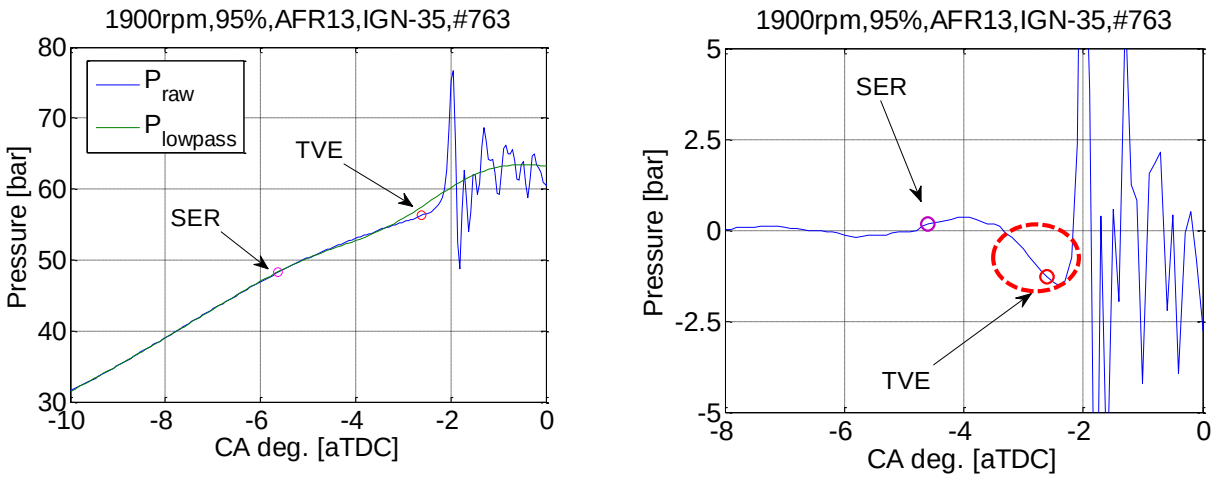

Figure 4.2 In-cylinder pressure and low- and high-pass filtered pressure at 1900RPM, 95%, AFR13 and ignition timing -35 aTDC

To avoid the bias associated with the Butterworth low- and high-pass filter in determining knock onset, a new filter was tested and validated. Figure 4.3 shows low- and high-pass filtered pressure data using different filters, such as median (med) and smoothing (SM) filters, and the combined use of the filters, for a single cycle with severe knock intensity. For both median and smoothing filters, 10 data points, which corresponds to 1 CA degree duration at this speed, were used for filtering. It is shown in Figure 4.3 (a) that the result of using median and smoothing filters matches the raw pressure much better around the initial pressure rise. It is also shown in Figure 4.3 (b) that the combined median and smoothing filtered pressure data are close to zero before the initial pressure rise, i.e., they match the raw cylinder pressure well up to knock onset. The Butterworth high-pass filtered pressure data fails to calculated reliable high-pass filtered pressure, especially in the range of ±1 CA degree from knock onset.

(a)

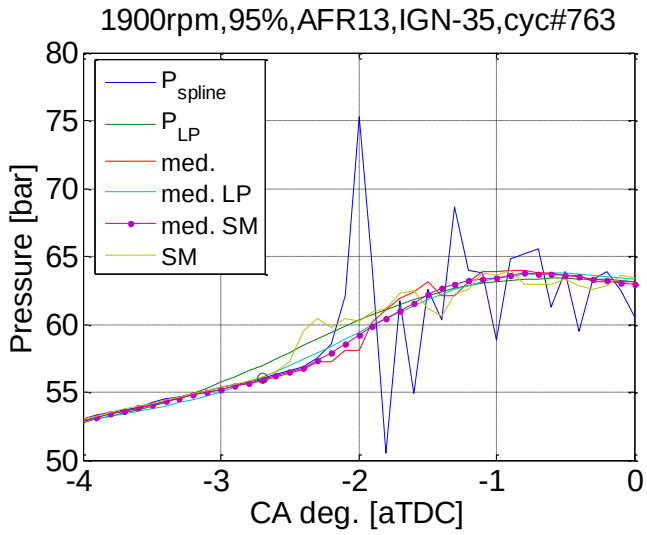

(b)

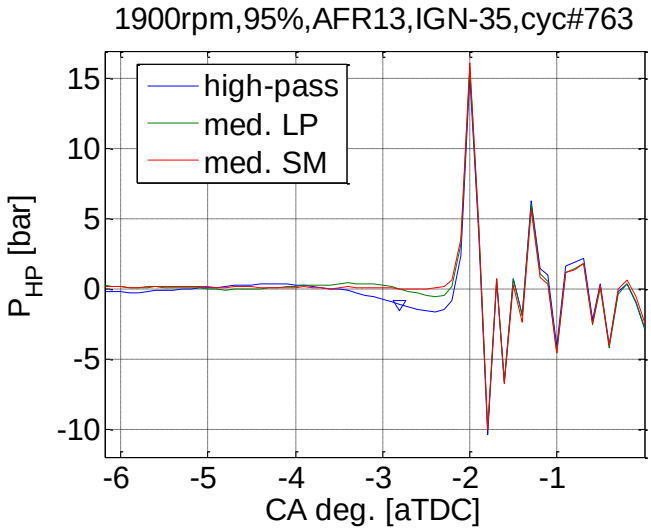

Figure 4.3 (a) Spline fitted experimental pressure and low-pass, median, median/low-pass, median/smoothing and smoothing filtered pressure (b) Butterworth, median/low-pass and median/smoothing hi-pass filtered pressure at 1900RPM, 95%, AFR13 and ignition timing -35 aTDC

To determine knock onset using the new filter, a new method was developed. Even though the high-pass filtered pressure and TVE method cannot provide an accurate result of determining the knock onset, it does, however provide a timing that is close to knock onset with good reliability. The dip in the high-pass filtered pressure was found, and used as a first estimate knock onset. The mean and standard deviation of the median and smoothing high-pass filtered pressure (med. SM

in Figure 4.3) for 5 CA degree before the estimated knock onset was computed to evaluate any noise included in the filtered data. It was concluded that using a threshold that was 5 times the standard deviation of the median and smoothing high-pass filtered pressure before the estimated knock onset showed good results for determining an accurate knock threshold. Figure 4.4 shows the calculation procedure for a sample condition.

Figure 4.5 (a) shows the knock onset determination for a severe knock case, where the TVE method is 0.5 CA degree later than the new method; the pressure at knock onset from the TVE method is about 4 bar higher than the true value. Figure 4.5 (b) shows the knock onset determination for a relatively weak knock case, with MAPO knock intensity of 1.5 bar. It is seen in the figure that the TVE-determined knock onset was at 3 aTDC, which is later than the observed initial pressure rise at 2.5 aTDC. Compared to the TVE-determined knock onset, the new knock onset determination method found knock onset very close to the initial pressure rise for both weak and strong knock cases. Figure 4.6 shows the knock onset determined by the new method at a different engine speed for both severe and intermediate knock intensity cycles. The new method is found to be more accurate.

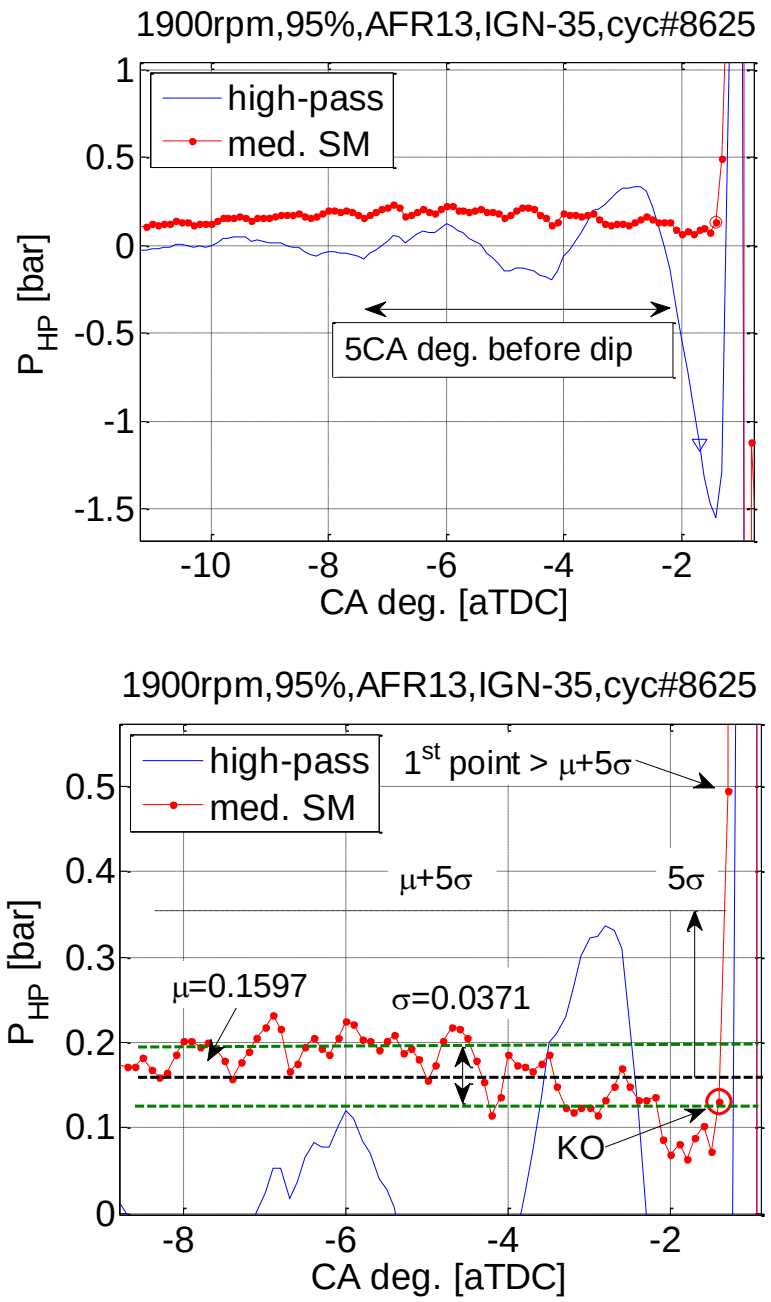

Figure 4.4 Comparison of filtering in-cylinder pressure at 1900RPM, 95%, AFR13 and ignition timing -35 aTDC

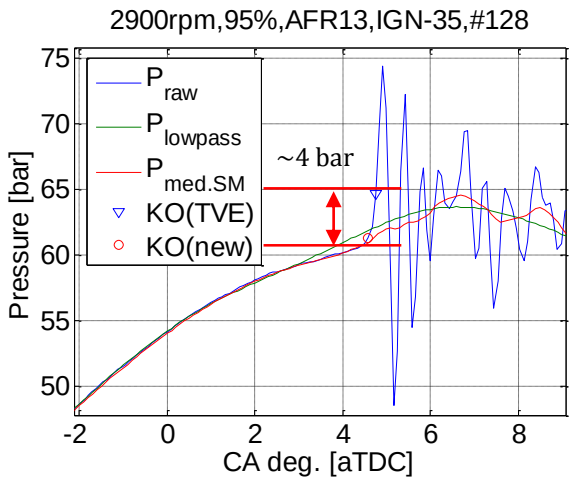

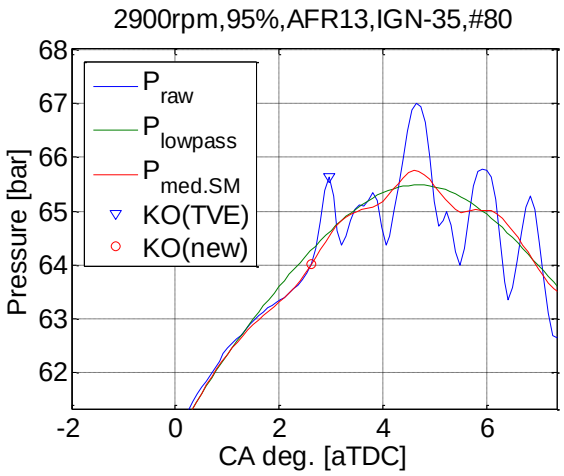

(a) (b)

Figure 4.5 Knock onset comparison at 2900RPM, 95%, AFR13 and ignition timing -35 aTDC

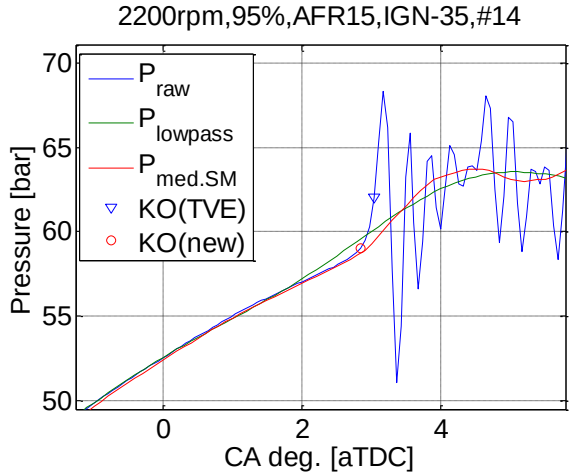

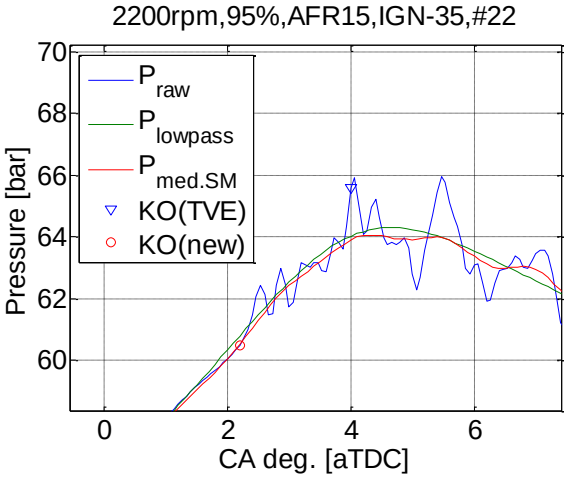

(a) (b)

Figure 4.6 Knock onset comparison at 2200RPM, 95%, AFR15 and ignition timing -35 aTDC

A comparison of new knock onset determination method to the other methods is summarized in Figure 4.7 for different speed and load conditions. Each condition with 5,000 cycles in-cylinder pressure data were used for PDF plot. It is seen in Figure 4.7 that the knock onset distribution of the new method lies between the SER and TVE method's distributions, but is closer to the TVE method. At low speed, the new method showed 1 CA degree advanced

knock onset results, while the high speed conditions showed relatively smaller differences in comparison to the TVE method.

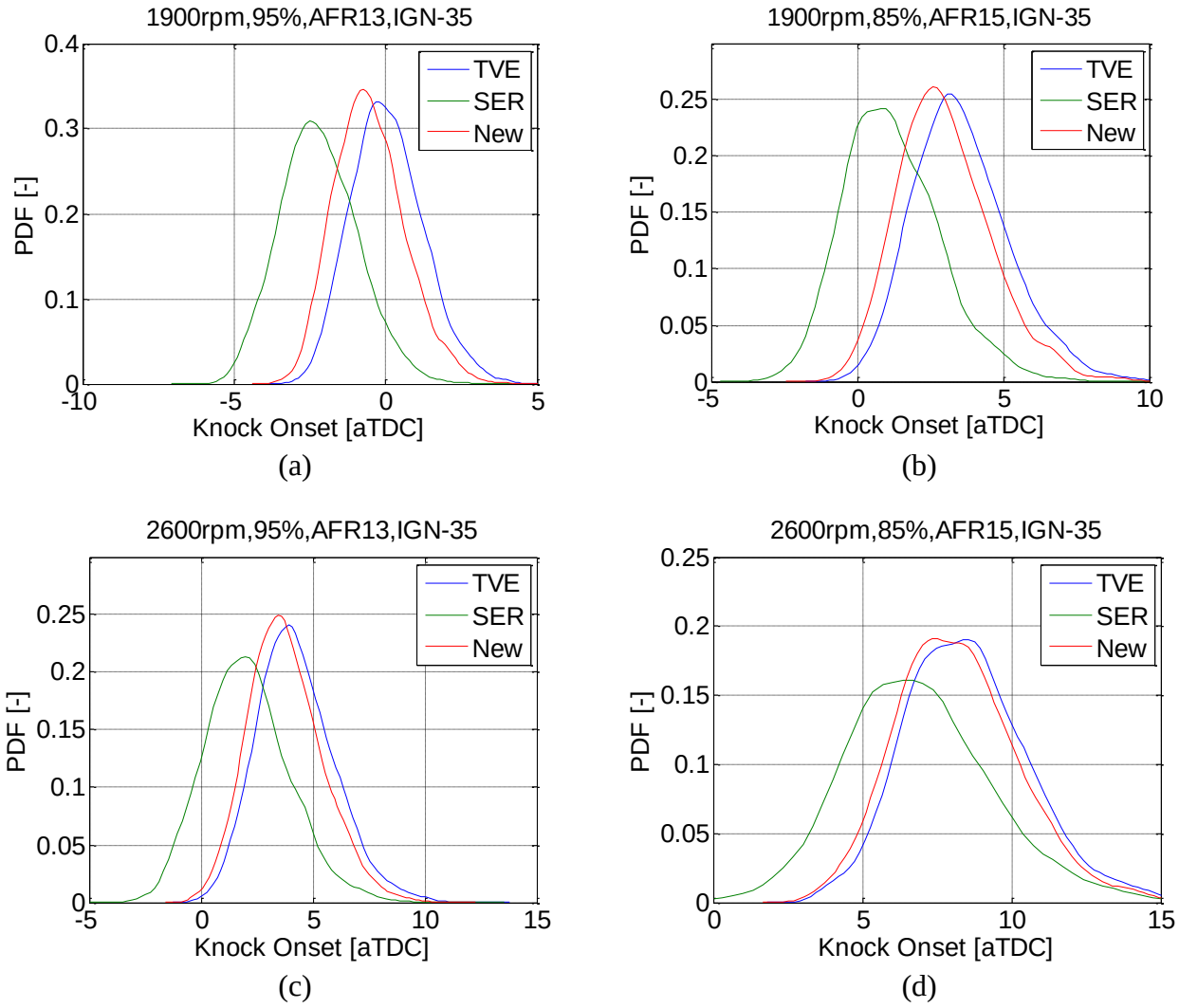

Figure 4.7 PDF of knock onset comparison using TVE, SER and new knock onset determination methods

Figure 4.8 shows the comparison of in-cylinder pressure at knock onset determined by the TVE, SER and new method at the same operating conditions seen in Figure 4.7. When

comparing the TVE and new method, the maximum difference of the in-cylinder pressure at knock onset was ~5 bar, which is about 10% of the in-cylinder pressure at knock onset.

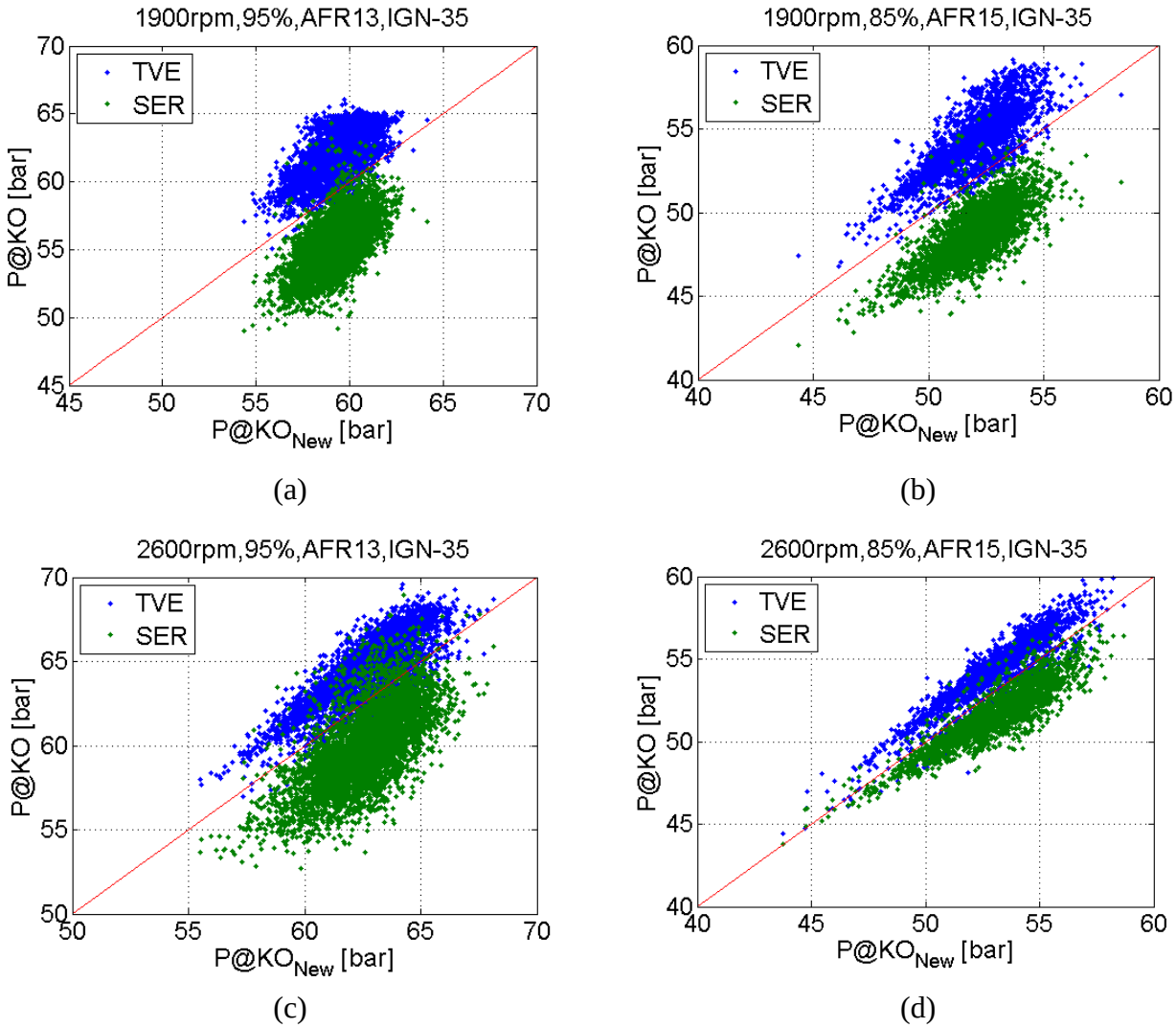

Figure 4.8 Comparison of in-cylinder pressure at knock onset determination by TVE, SER and new method

All following knock onset data shown in this thesis will be calculated using the newly developed method.

Chapter 5 Heat Release Rate Calculation

The combustion process and performance can be analyzed by measuring in-cylinder pressure and calculating the heat release rate. However, combustion analysis in an engine is complex because of volume change due to piston motion, mass loss due to blow-by gas, chemical processes with energy addition, and heat transfer to the combustion chamber surfaces. The heat release rate calculation is especially important in this research, because the unburned mass of fuel at knock onset will be a key parameter for understanding knock intensity. This chapter discusses a number of different heat release calculation approaches and its verification to calculate the most accurate heat release rate.

5.1 Fundamentals of Heat Release Rate Calculation

Heat release rate is calculated using a 1st law balance that includes heat transfer, using the Woschni heat transfer correlation, as seen in equations (5.1) - (5.3). A global energy balance was enforced between the fuel energy and the integrated heat release by scaling the heat transfer by a multiplicative constant as seen in equation (5.4). The heat transfer constant was determined using the ensemble averaged cylinder pressure of at least 1,000 consecutive cycles. The model allows for a temperature- and equivalence-ratio dependent specific heat ratio, γ, as given in equation (5.5) [78]. The residual mass fraction was calculated based using the Yun and Mirsky correlation [77]. By virtue of the single-zone assumption, only a mass-average temperature is calculated using the ideal gas law.

$$\frac{dQ_{ch}}{d\theta} = \frac{\gamma}{\gamma-1} p \frac{dV}{d\theta} + \frac{1}{\gamma-1} V \frac{dp}{d\theta} + \frac{dQ_{ht}}{d\theta} \tag{5.1}$$

$$h_c[\frac{W}{m^2K}] = 3.26B[m]^{-0.2} p[kPa]^{0.8} T[K]^{-0.55} w[\frac{m}{s}]^{0.8} \tag{5.2}$$

$$w = \left[C_1 \bar{S}_p + C_2 \frac{V_d T_r}{p_r V_r}(p - p_m)\right] \tag{5.3}$$

$$HT = \frac{Q_{hr} - \int \frac{dQ_{ch}}{d\theta} d\theta}{\int \frac{dQ_{ht}}{d\theta} d\theta} = \frac{Q_{hr} - \int \frac{\gamma}{\gamma-1} P \frac{dV}{d\theta} d\theta + \int \frac{1}{\gamma-1} V \frac{dp}{d\theta} d\theta}{\int hA(T - T_w) d\theta} \tag{5.4}$$

$$\gamma = max \begin{cases} \gamma_0 + \gamma_1 T[K] \\ \gamma_{HT} \end{cases} \tag{5.5}$$

$$\gamma_0 = 1.426\Phi^2 - 0.0459 \tag{5.5}$$

$$\gamma_1 = 10^{-5} \times (1.02\Phi^2 - 3.30\Phi - 9.44) \tag{5.5}$$

$$\gamma_{HT} = 0.0386\Phi^2 - 0.0838\Phi + 1.33 \tag{5.5}$$

$$Q_{cum} = \frac{\int \left(\frac{dQ_{ch}}{d\theta}\right) d\theta}{m_{fuel} * \eta_{comb} * LHV} \tag{5.6}$$

Figure 5.1 shows calculated heat release, heat transfer and cumulative heat release rate using equations (5.1) - (5.6). It is seen in Figure 5.1 that the heat release rate at the end of combustion is not zero. Ideally, the heat transfer multiplier, *HT*, should be close to unity if the Woschni correlation correctly predicts the overall heat transfer. However, the heat transfer multiplier was 2.55 for this case, which results in an over-prediction of the amount of heat transfer at the end of combustion.

For multi-cylinder engine applications like this, where the exact amount of fuel and air in any one cylinder is not known with high accuracy, the most critical parameter for heat release calculations was found to be the end angle of heat release calculation, i.e., the limits of integration in equation (5.4).

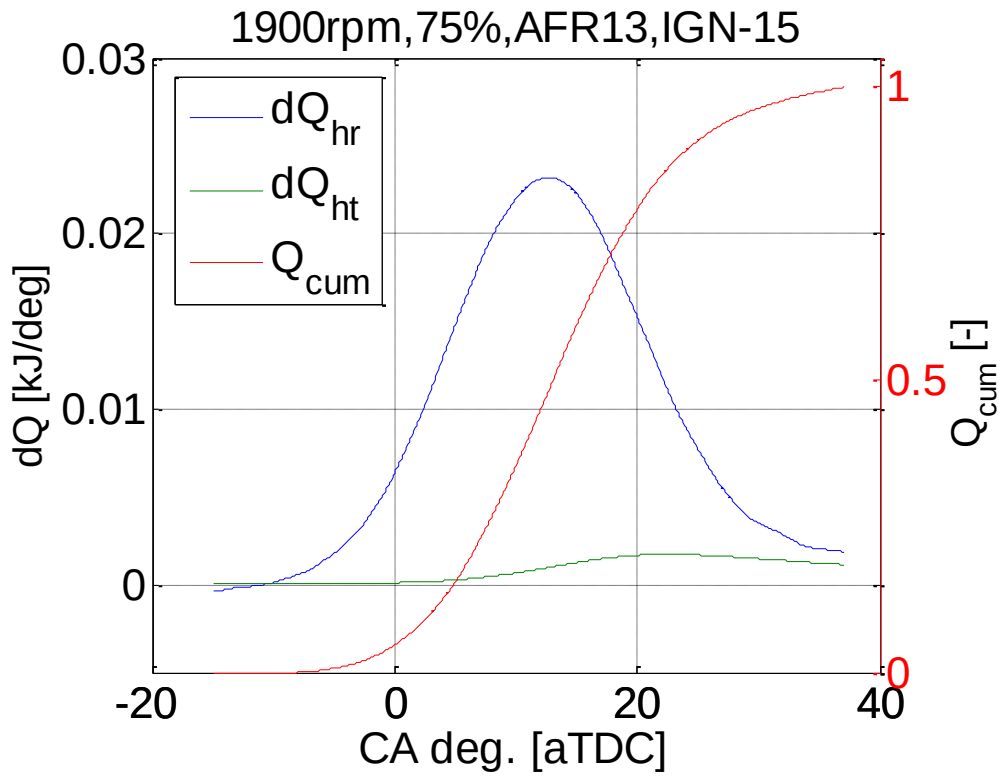

Figure 5.1 Calculated heat release, heat transfer and cumulative heat release rate at 1900RPM, 75% load, AFR13 and ignition timing -15 aTDC

The size of the calculation window affects the calculation of the experimental heat release mainly due to uncertainty in the heat transfer rate. An incorrect end angle of heat release calculation window can lead to inaccurate combustion phasing and unrealistically high values of the heat release near the end of combustion. A general profile of the cumulative heat release shows an 'S' shape curve, where the early and mid-flame developments are generally determined by the rapid increase of in-cylinder pressure. However, during the late period of a combustion, where the mass burn fraction is 0.8 or larger, the calculated heat release is significantly affected by the end angle of the heat release calculation window. If the end angle is too early, the calculated heat release rate becomes higher than it should be to match the energy balance (eq. (5.4)) in the short time window. On the other hand, when the end angle is too late, the calculated heat release rate

after CA90 will be dominated by the ability to correctly predict heat transfer, which can lead to an extended tail.

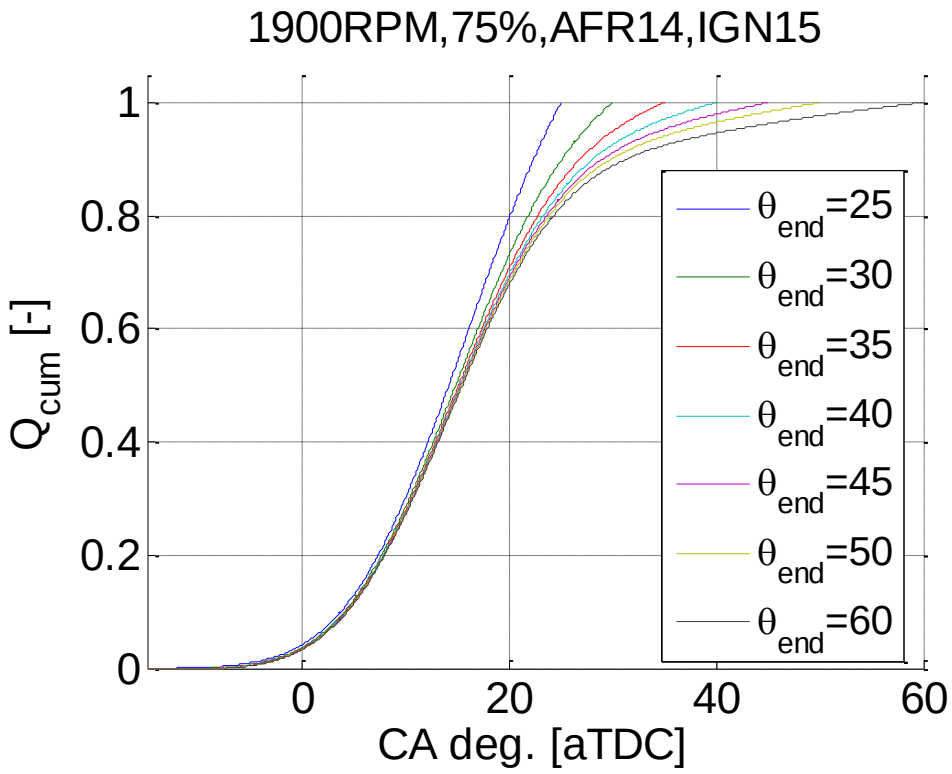

Figure 5.2 Calculated cumulative heat release rate at 1900RPM, 75% load, AFR14 and ignition timing -15 aTDC

A fixed heat release calculation window to determine the heat transfer multiplier was initially investigated for a range of operating conditions. Operating conditions with no knock were chosen to avoid any biases. Figure 5.2 shows the calculated cumulative heat release rates using equations (5.1) - (5.6), by changing the calculation window size from 40 to 65 CA degrees with 5 CA degree increments. It is seen in the Figure 5.2 that the cumulative combustion profile is largely affected by the window size of heat release rate calculation, mostly during the end of combustion where the burn fraction is larger than 0.8. The differences in crank angle for CA50 and CA80

were about 1 and 3.5 CA degree, respectively. During the end of combustion, the amount of heat release is mostly dominated by the amount of heat transfer. As a result, extending the window size of heat release calculation will not guarantee calculating a more accurate heat release rate. Instead, the same amount of total heat transfer will be distributed in a larger window size, affecting the overall combustion shape as a relatively slow burning case.

5.2 Fixed Heat Release Calculation Window

Initially, a fixed calculation window for investigation at 1900 RPM, of 45 CA degrees was used based on the relatively good match with a general shape of an 'S' curve. For a higher engine speed, the fixed calculation window was adjusted to allow same time duration, for example, 60 CA degrees at 2600 RPM.

Figure 5.3 (a) shows the calculated cumulative heat release rate using a fixed calculation window of 45 CA degrees for a range of operating conditions including three different AFRs and two different ignition timings. It is seen in the Figure 5.3 (a) that the fuel rich condition facilitates early flame development compared to the lean condition, giving an advanced combustion phasing, and lean combustion leads to a longer time period from ignition to CA20. However, the end angle of heat release calculation was fixed for all three AFRs, which forces the combustion to be ended at the given timing. As a result, the lean combustion shows a relatively slow development from ignition to CA20, however, the time between CA80 to CA100 is the shortest and vice versa for the rich combustion case. Forcing an energy balance into a fixed window size, which does not account for the differences in combustion development and phasing appears to have caused these errors in calculated heat release results. Figure 5.3 (b) shows the calculated cumulative heat release rate at

a different engine speed, but using the same actual time for the calculation window. The same effect of AFRs and combustion development is seen in the Figure 5.3 (b).

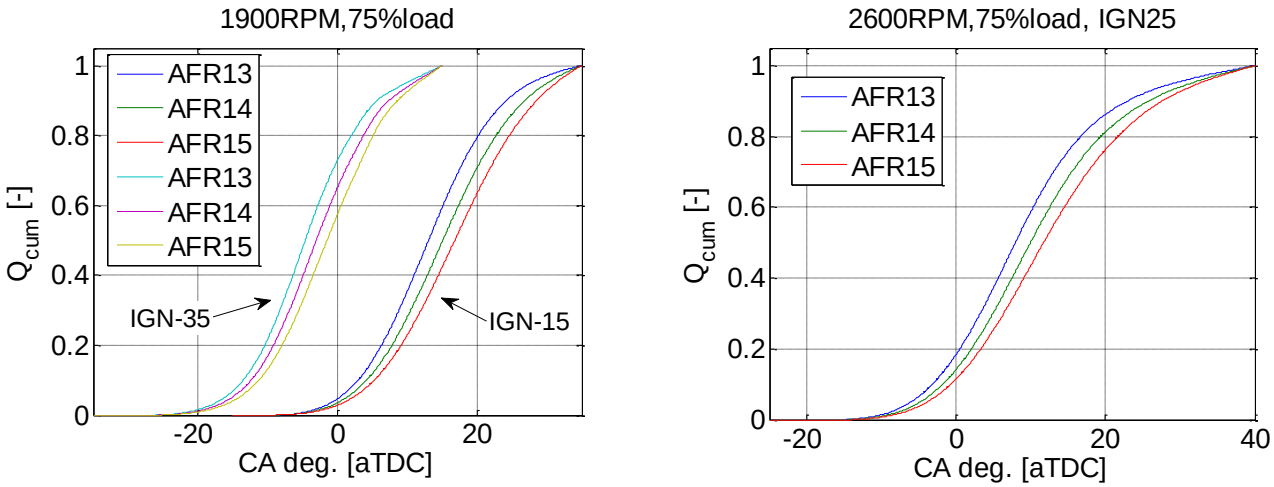

(a) (b)

Figure 5.3 Comparison of calculated cumulative heat release rate using a fixed combustion duration at (a) 1900RPM, 75% load and ignition timing -35 and -15 aTDC and (b) 2600RPM, 75% load and ignition timing -25 aTDC

Finding the most accurate heat release rate is problematic mostly because there is no absolute scale that can determine the accuracy of the calculated heat release rate. The best possible approach to verify the accuracy of heat release calculation is to use a thermodynamic engine model to calculate the in-cylinder pressure and compare its match to the experimental data. Because the thermodynamic engine model is effectively the same as heat release calculation, the model-predicted pressure should be internally consistent with the measured pressure. A Wiebe function curve-fit was performed between CA2 to CA90 to minimize the variation in end of the cumulative heat release rate.

Figure 5.4 shows the cumulative heat release rate (solid line) and its curve-fitted result (dotted line) for different heat release calculation end-angles. The values of 45 and ±5 CA degree were used for comparison. It is seen in the Figure 5.4 that the Wiebe curve-fit matches the

cumulative heat release rate from the initial flame development to CA90 quite well. If the calculated heat release rate is correct, the predicted in-cylinder pressure should match the experimental pressure, based on the assumption of internal consistency. The model-predicted and experimentally collected in-cylinder pressure of two different AFRs are seen in Figure 5.5. It is seen in the Figure 5.5 that the pressure increase during the compression and combustion period and the location of the peak pressure are reasonably well matched with the calculation window of either 45 or 50 CA degree. The large differences after the end angle of the heat release calculation are mostly due to the heat transfer, which is over-estimated by the Woschni correlation.

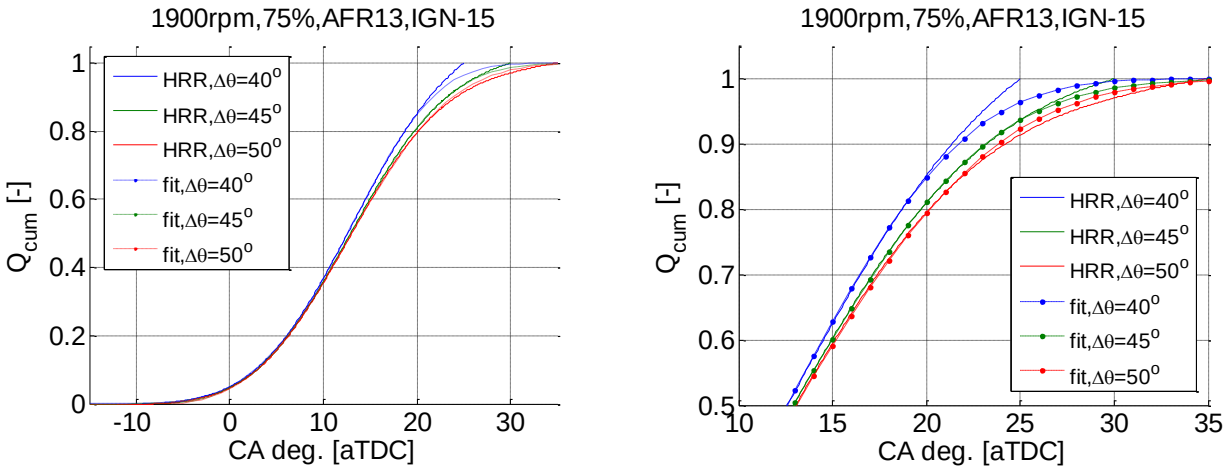

(a) (b)

Figure 5.4 Calculated and curve-fitted cumulative heat release rate at 1900RPM, 75% load, AFR13 and ignition timing -15 aTDC

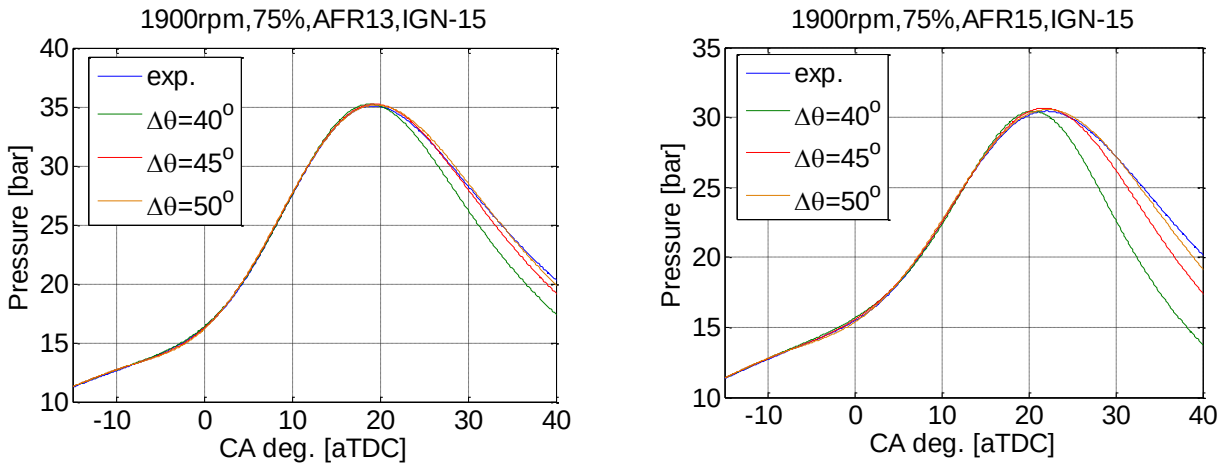

(a) (b)

Figure 5.5 Experimental and model predicted in-cylinder pressure at 1900RPM, 75%, AFR13 and 15 and ignition timing -15 aTDC

Figure 5.6 and Figure 5.7 show experimental and model-predicted cylinder pressure at operating conditions with different AFR, ignition timing and engine speed. To allow the same time duration, the fixed calculation window was determined proportional to the engine speed, i.e., 50 and 60 CA degrees at 2200RPM and 2600RPM, respectively. It is shown in Figure 5.6 (a) and (b) that the best match of the peak pressure value and location were achieved when the heat release calculation window was between 45 and 50 CA degrees. Figure 5.7 also shows a reasonable match of the in-cylinder pressure, however, the location and value of the peak pressure are not exactly matched for any fixed combustion durations. Unmatched peak pressure implies that using a fixed combustion duration cannot calculate an accurate heat release rate over the range of operating conditions with different combustion development speed.

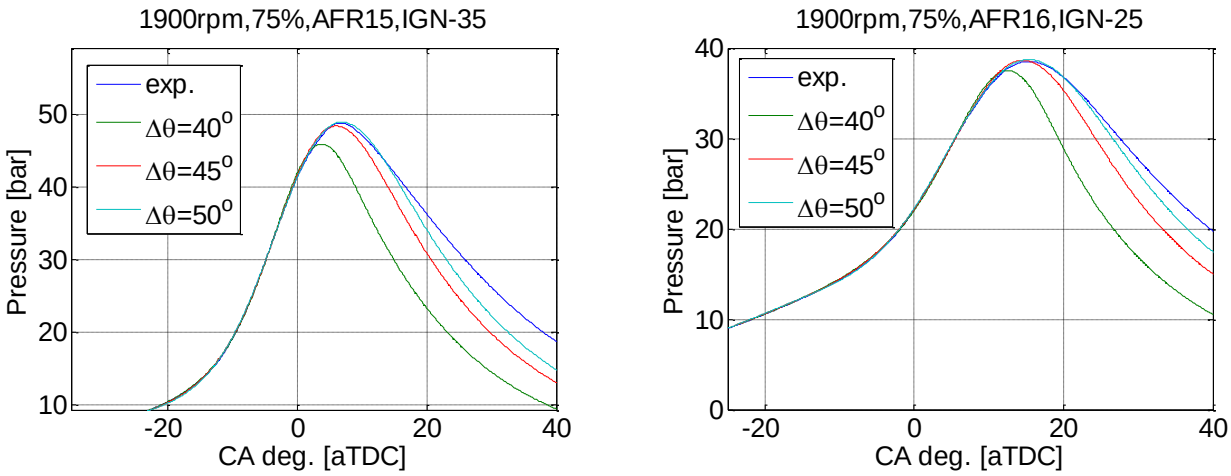

(a) (b)

Figure 5.6 Experimental and model predicted in-cylinder pressure at different AFRs and ignition timings

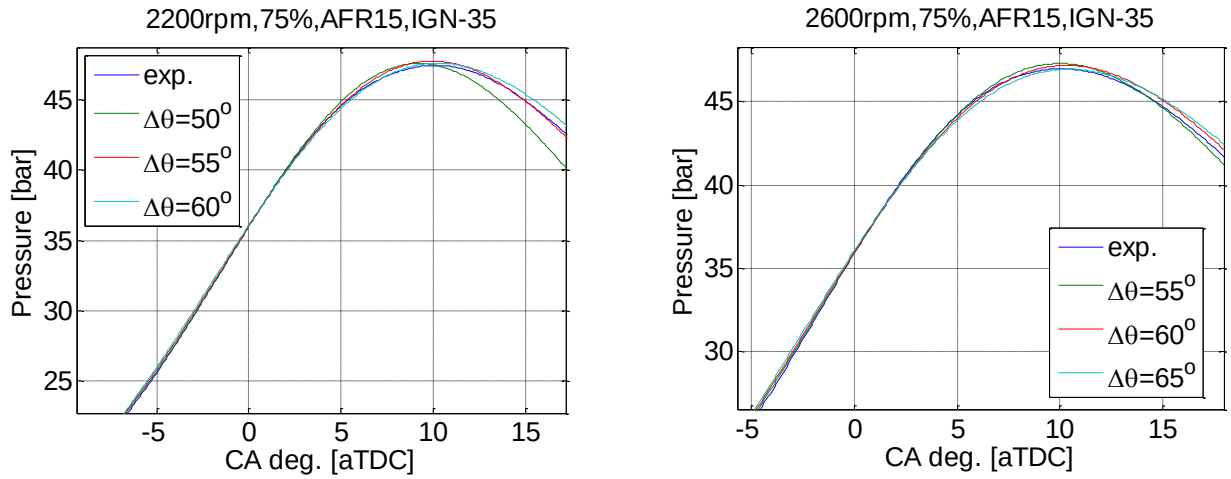

(a) (b)

Figure 5.7 Experimental and model predicted in-cylinder pressure at different engine speeds and ignition timings

5.3 Adjusted Heat Release Calculation Window

5.3.1 Approximate Heat Release Rate Calculation

To adjust the calculation window size for each operating condition, the approximate methods of calculating the heat release rate suggested by Marvin [79] and Rassweiler and Withrow [80] were used to estimate the end angle. This method was developed in the early engine-development era to calculate the pressure increase only due to the combustion based on the fact that in-cylinder pressure data show a polytropic behavior. The cumulative burn fraction is calculated as shown in equations (5.7) and (5.8)

$$y_{1,approx.} = \frac{p-p_i}{p_f-p_i} = \frac{pV^n-p_iV_i^n}{p_fV_f^n-p_iV_i^n} \tag{5.7}$$

$$y_{2,approx.} = \frac{p-p_i}{p_f-p_i} = \frac{p^{1/n}V-p_i^{1/n}V_i}{p_f^{1/n}V_f-p_i^{1/n}V_i} \tag{5.8}$$

where p_i, p_f, V_i and V_f are the pressures and volumes at the start and the end of combustion, and n is the polytropic exponent. Because the combustion is not a constant volume process, the pressure terms should be corrected to their top dead center (TDC) equivalent values assuming the polytropic compression as, $p_{TDC}V_{TDC}^n = pV^n$. The polytropic exponent was found by fitting the pressure-volume data during the compression.

Figure 5.8 shows calculated heat release results obtained using the approximate methods and the detailed method of equations (5.1) - (5.6). A number of different values for the end angle of the detailed heat release calculation are shown. Brunt and Emtage [81] suggest an end angle 10 crank angle degrees past the point that has the maximum value of $pV^{1.15}$. The heat transfer multiplier was calculated independently for each different calculation end angle to match the

energy balance. The detailed heat release calculation using different end angles closely match the approximate heat release results up to the mass burn fraction of 0.85, and then separated based on the calculation window size. The difference between the detailed and the approximate heat release calculation was close to a constant from the early flame development to the mass burn fraction of 0.85, which is the range that the heat transfer plays less significant role. The optimal end angle of heat release calculation is affected largely by the accurate estimation of the heat transfer during the end of combustion. No convincing evidence of an optimal determination of the calculation window was found by simply comparing the heat release rate at the end of combustion between the approximate heat release and the detailed heat release calculation.

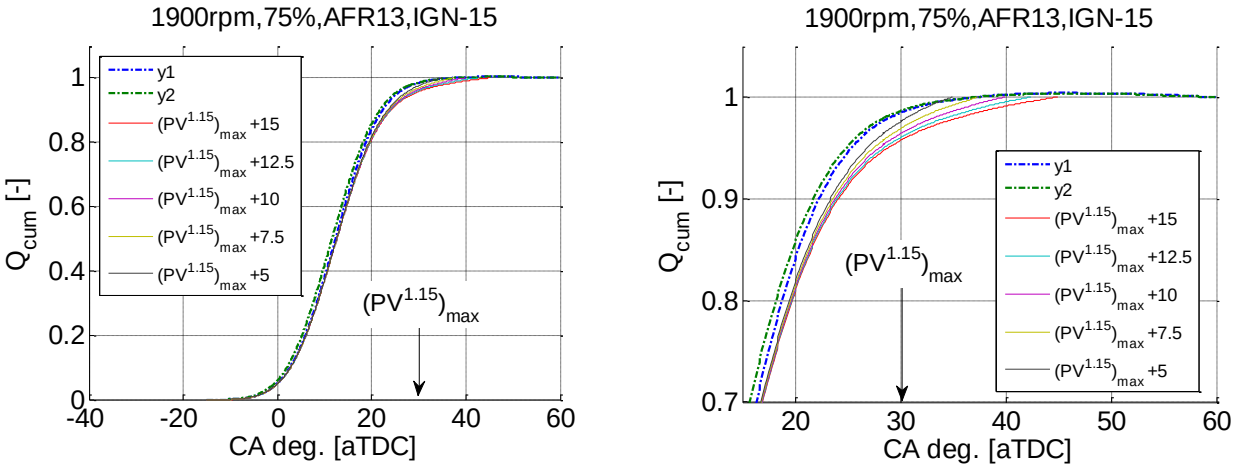

(a) (b)

Figure 5.8 Comparison of the calculated heat release rate between approximate and detailed method at 1900RPM, 75% load, AFR13 and ignition timing -15 aTDC

5.3.2 Optimized Heat Release End Angle Determination

A strong linear correlation was found when comparing the timing of CA90, determined by the approximate method, to the maximum value of $pV^{1.15}$ suggested by Brunt and Emtage [81]. Figure 5.9 shows the correlation between these two parameters for 80 different operating conditions,

including 4 speeds, 3 engine loads, 3 AFRs and 3 different ignition timings, and included no knock to severe knock conditions. The ensemble averaged in-cylinder pressure was used for each operating conditions. The linear correlation found is stated as equation (5.9). The coefficient of determination (R^2) value for the correlation was 0.9834. The strong linear correlation implies the fact that the maximum value of $pV^{1.15}$ may be a feasible way of determining the end angle of heat release calculation for different speeds of combustion.

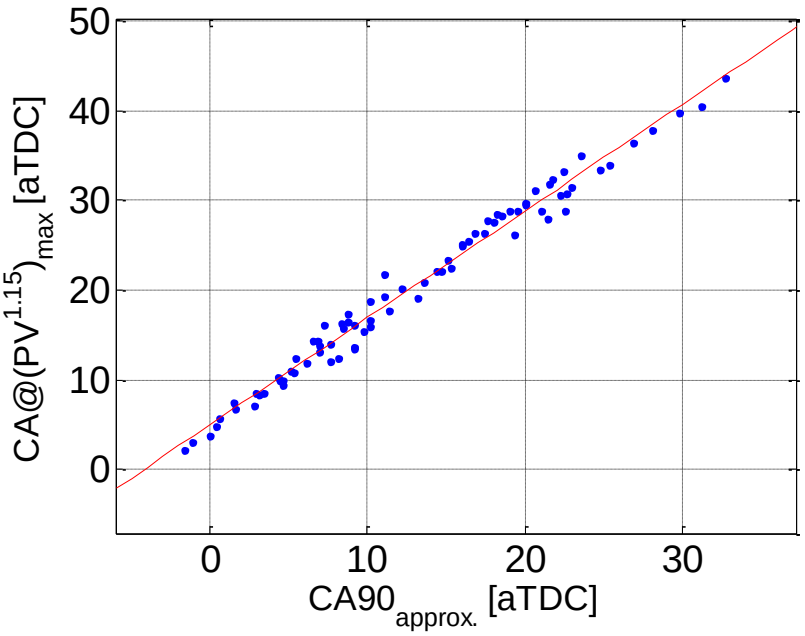

Figure 5.9 Linear correlation between $CA90_{approx.}$ and $(PV^{1.15})_{max}$

$$(CA)_{@(pV^{1.15})_{max}} \approx 1.189 * (CA90)_{approx.} + 5.035\ CA\ deg. \quad (5.9)$$

Figure 5.10 compares the correlation of using different exponents to find crank angle at maximum value of pV^q and the CA90 calculated from the approximate method. It is seen in the Figure 5.10 that the value of q=1 shows a good correlation with a higher R^2 value compared to using the value of 1.15, which was originally suggested by Brunt and Emtage [81].

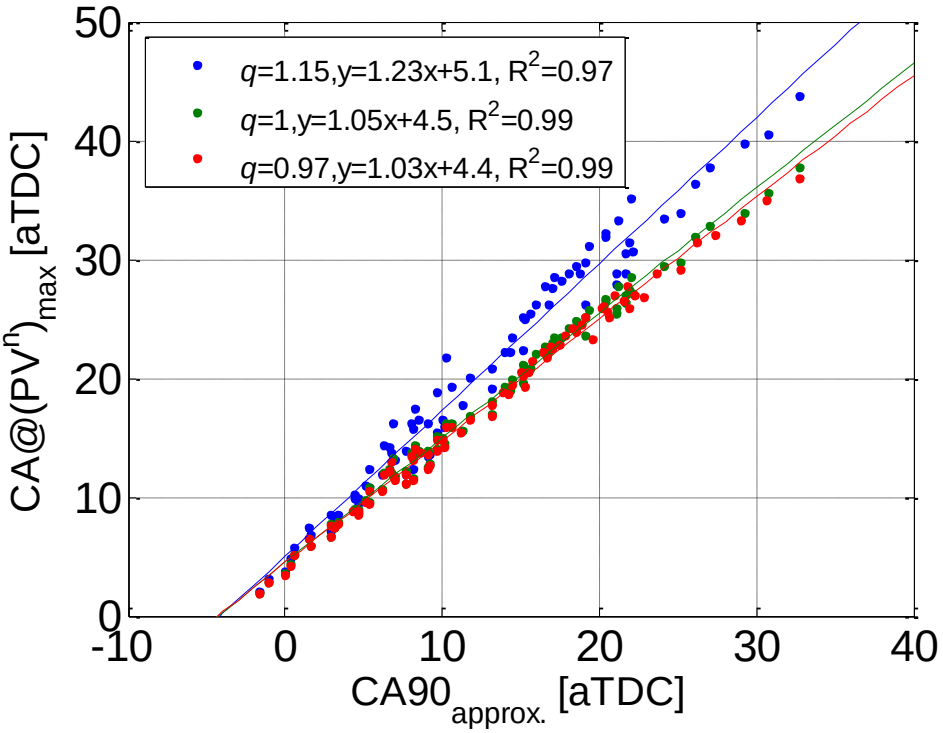

Figure 5.10 Comparison of the exponent value and its correlation to $CA90_{approx.}$

Another parameter that should be optimized is the offset value, which is the time duration between the crank angle at the maximum value of pV^1 and the predicted end angle of the heat release calculation. A Wiebe function was used to define an end angle to avoid uncertainty and bias of predicting heat transfer during the end of combustion. This assumes that the Wiebe function characterizes combustion profile well and therefore, ideally, the combustion profile during the end of combustion will be close to the cumulative heat release rate predicted by Wiebe function parameters. The Wiebe parameters were curve-fit to the cumulative heat release rate data from CA3 to CA80. The end angle of a combustion from the Wiebe function parameters was predicted as the timing when the mass burned fraction reached to 99.9% (or CA99.9). Figure 5.11 shows the results for a range of different offsets from the crank angle at the maximum value of pV^1. It is seen in the Figure 5.11 that the same offset suggested by Brunt and Emtage matches the

end angle of combustion, determined by the Wiebe function parameters well. The adjusted end angle of the heat release calculation window is seen in equation (5.10). The accuracy of using the adjusted end angle will be investigated for ensemble averaged and single-cycle heat release calculations in the next two sections.

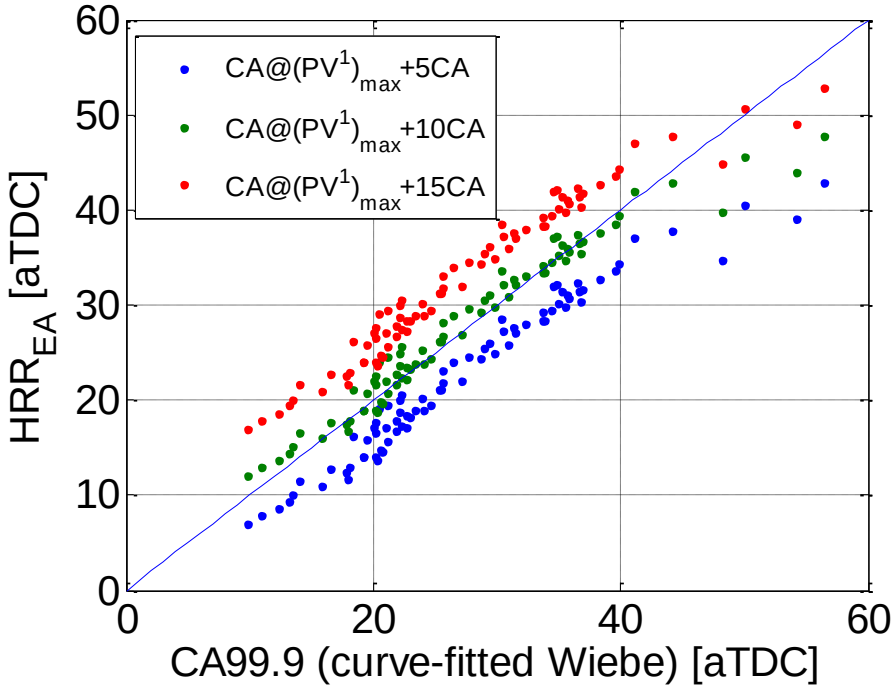

Figure 5.11 Comparison of the offset to determine end angle of heat release calculation

$$HRR_{EA} = CA@(PV^1)_{max} + 10\ CA\ deg. \tag{5.10}$$

5.3.3 Analysis on Ensemble Averaged Heat Release Rate

The optimized end angle of heat release calculation method from the previous section was used to determine a single value from ensemble averaged pressure for each operating conditions. Figure 5.12 compares the experimental and model-predicted pressure using the fixed (45°) and optimized calculation window. It is seen in Figure 5.12 that the predicted in-cylinder pressure

using the adjusted end angle matches the experimental data marginally better than the fixed end angle case. This implies that the calculated heat release rate using the fixed end angle are biased by inaccurate window size.

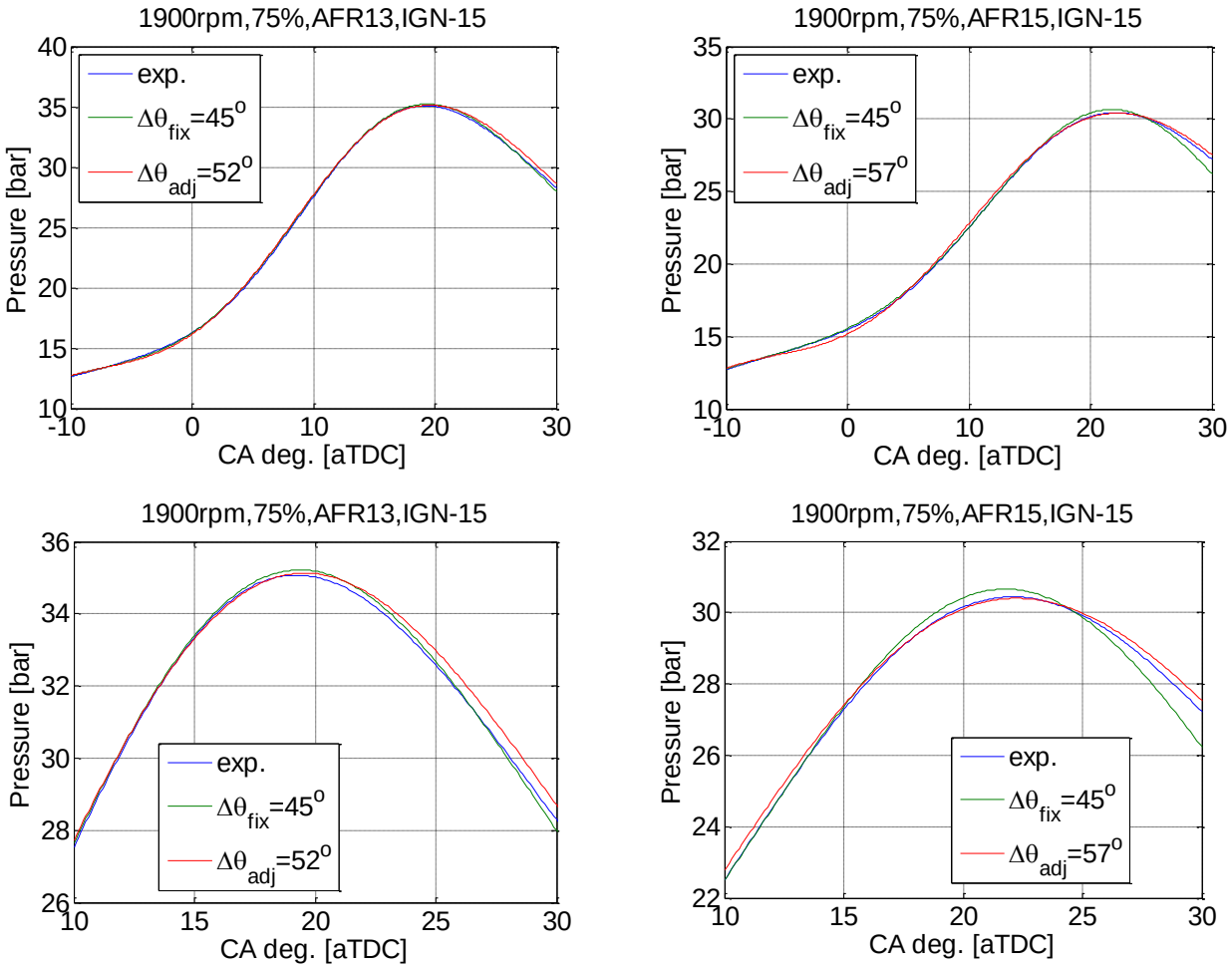

(a) (b)

Figure 5.12 Experimental and model predicted in-cylinder pressure of fixed and adjusted end angle of heat release calculation at 1900RPM, 75% load, AFR 13 and 15 and ignition timing -15 aTDC

Figure 5.13 shows in-cylinder pressure comparison at different AFRs and ignition timings. It is seen in Figure 5.13 that the fixed calculation window case over-estimated the heat transfer multiplier due to a shorter heat release calculation window size, which resulted in large differences

during the expansion stroke. For a range of operating conditions, the adjusted end angle of heat release calculation showed a better match to experimental in-cylinder pressure than the fixed end angle.

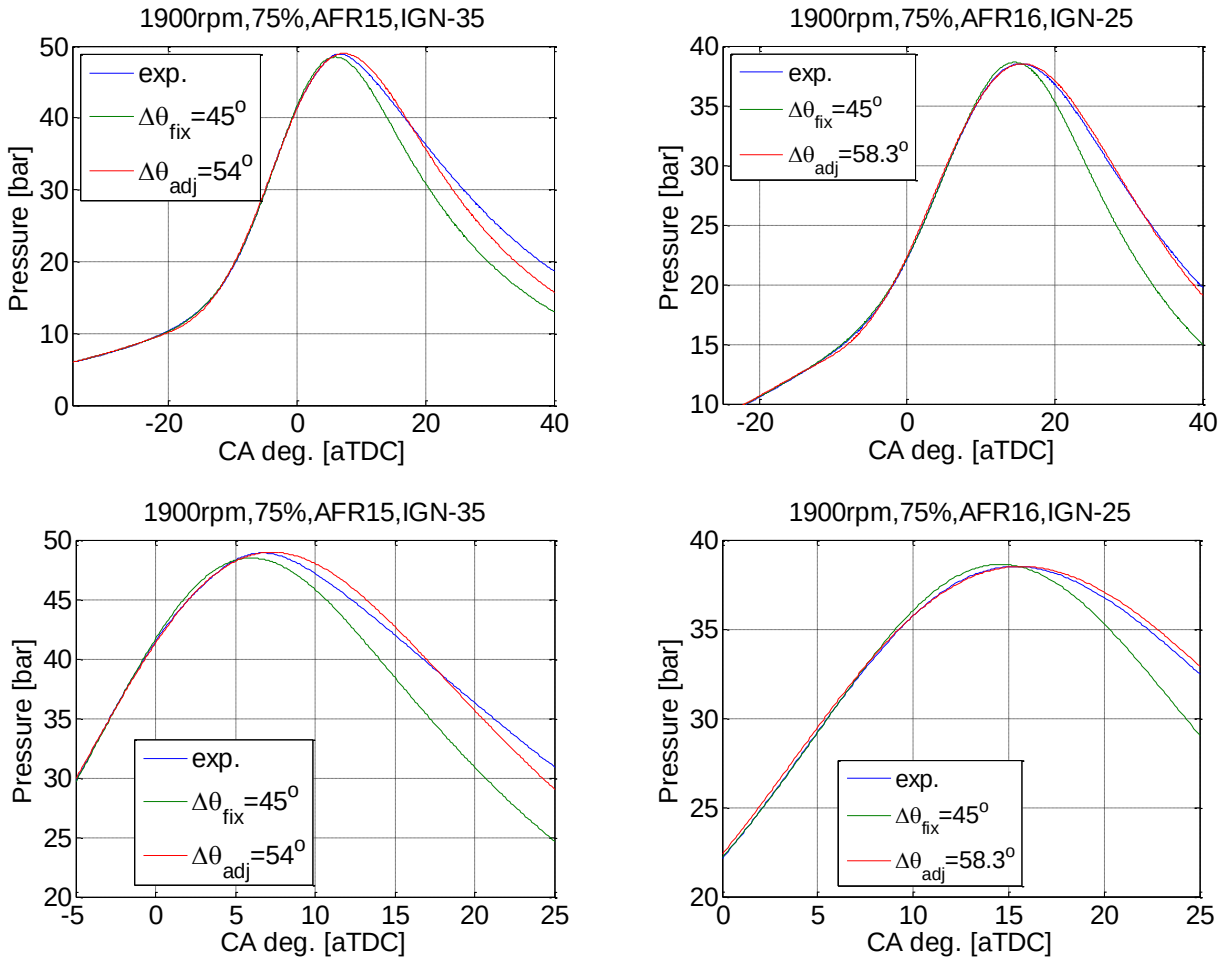

(a) (b)

Figure 5.13 Experimental and model predicted in-cylinder pressure of fixed and adjusted end angle of heat release calculation at 1900RPM, 75%, AFR15 and ignition timing -35 aTDC and AFR16 and ignition timing -25 aTDC

5.3.4 Analysis of Single-cycle Heat Release Rate

The heat release calculation end angle and the heat transfer multiplier determined from the ensemble averaged cylinder pressure were applied to each single cycle to calculate the heat release rate. Figure 5.14 (a) shows the cumulative heat release from single-cycle data (cycle #3) and its curve-fitted results using both fixed and adjusted end angle of heat release calculation. A large difference between the detailed heat release calculation and curve-fitted result at the end of combustion is seen in the Figure 5.14 (a). The linearly increasing cumulative heat release seen for the adjusted end angle case (green solid line in Figure 5.14 (a)) at the end of combustion implies that the adjusted end angle is retarded from what it should be. Figure 5.14 (b) shows the in-cylinder pressure comparison between experiment and two different end angles. It is seen in Figure 5.14 (b) that both end angles of the heat release calculation are not at the correct value that would predict an accurate in-cylinder pressure. The optimal combustion duration would be in between 45 and 54 crank angle degrees to match the peak pressure value and phasing.

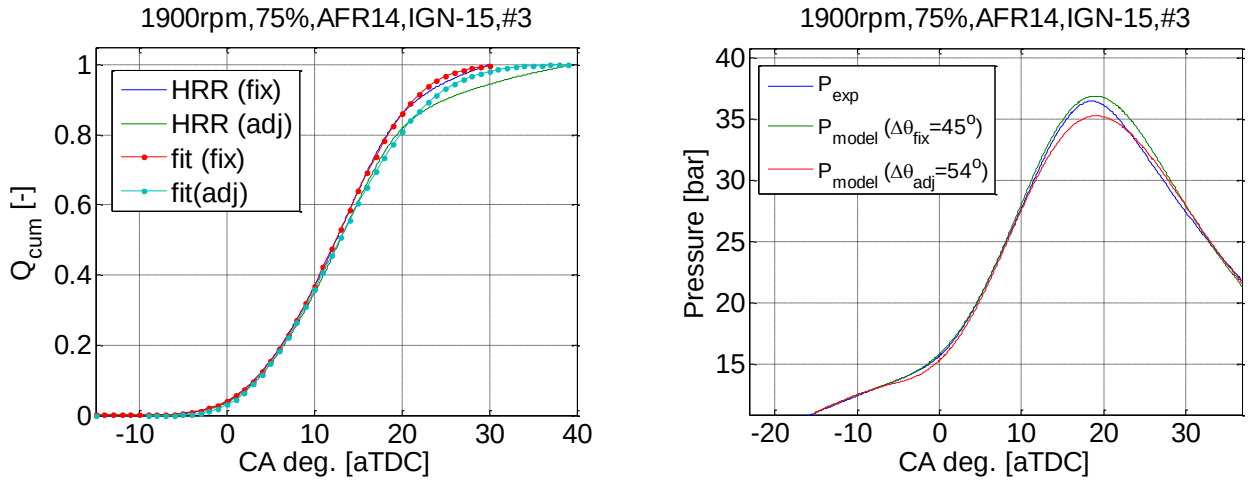

(a) (b)

Figure 5.14 Calculated and curve-fitted cumulative heat release rate and in-cylinder pressure at 1900RPM, 75% load, AFR14 and ignition timing -15 aTDC

Calculating accurate heat release rate significantly affects the thermodynamic conditions at knock onset. Figure 5.15 shows cumulative heat release and its curve-fitted results for both fixed and adjusted end angle of heat release calculation (a) and measured and the thermodynamic engine model predicted in-cylinder pressure (b) for a single cycle. The MAPO knock intensity was measured as 3.5 bar. The difference of heat release end angle calculation between fixed and adjusted combustion duration was relatively small, 3 crank angle degree, which is the reason why a similar cumulative heat release rates are seen between fixed and adjusted end angle. It is seen in the Figure 5.15 (a) that the calculated cumulative heat release rate are significantly affected by the engine knock even though the low-pass filtered pressure data were used to avoid bias of the pressure oscillations. A rapid increase right after the knock onset (open circle) is a signature of an autoignition of the end-gas, which is followed by the linear and slow burning from 3 aTDC to the end of combustion. It is a reasonable assumption that without knock, the cumulative heat release would be close to the curve-fitted profile from knock onset to the end of combustion. With this perspective, the curve-fitted Wiebe function profile and knock onset, which is determined as described in Chapter 4, will be used to determine the unburned mass fraction of fuel at knock onset. This is the reason why calculating an accurate heat release in knock condition is critical for further knock investigation. It is seen in Figure 5.15 (a) that the difference of cumulative mass burn fraction between heat release calculation and curve-fit is about 0.04, which is about half of the full range of unburned mass fraction at knock onset for the same operating condition. Ideally, the unburned mass fraction at knock onset determined from both heat release calculation and the curve-fit should be close to each other, if the calculated heat release is accurate. An inaccurate result of heat release calculation is also seen in Figure 5.15 (b); the thermodynamic engine model-predicted in-cylinder pressure for both calculation windows are not well matched to the

experimental pressure. In conclusion, using a single end angle for the heat release calculation, determined from the ensemble averaged pressure, does not give accurate heat release results for each individual cycle when large cyclic variability exists.

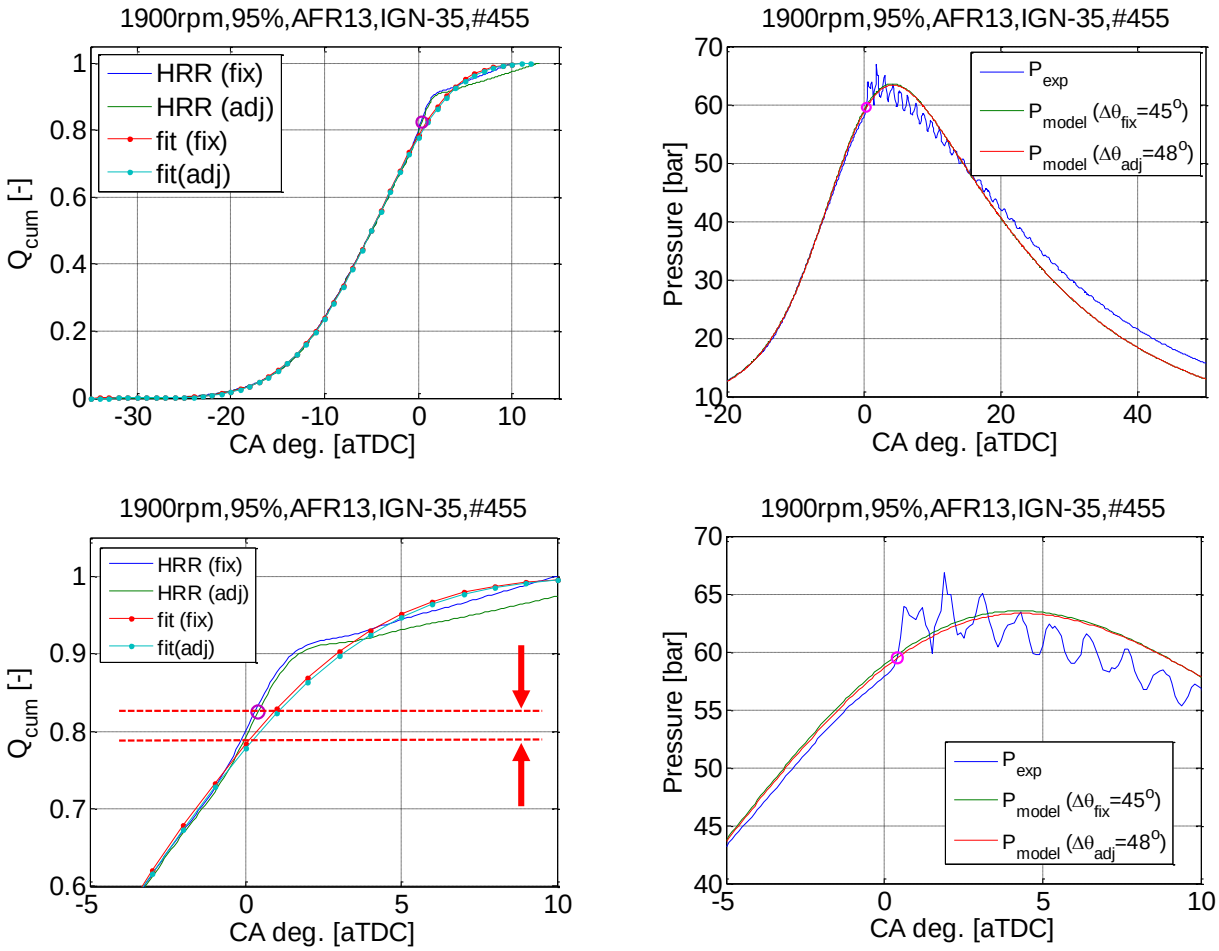

(a) (b)

Figure 5.15 Calculated and curve-fitted cumulative heat release rate and in-cylinder pressure at 1900RPM, 95% load, AFR13 and ignition timing -35 aTDC

5.4 Individual Cycle Heat Release Calculation

5.4.1 Pressure and Volume-based End Angle Determination

The optimized end angle for the heat release calculation, discussed in Chapter 5.3.2, was applied to each individual cycle to improve the accuracy of the heat release calculation. Figure 5.16 show a comparison of experimental single-cycle in-cylinder pressure to model-predicted pressure using an ensemble averaged and individually adjusted end angle. The heat transfer multiplier determined from the ensemble in-cylinder pressure was used for the ensemble averaged end angle calculation, while the heat transfer multiplier was determined individually for each cycle for the individually adjusted end angle. It is seen in the Figure 5.16 that the early pressure development, the location and the value of the peak pressure for both average and individual end angle of heat release calculation are different. The use of individually adjusted end angles for the heat release (equation (5.10)) generally showed a reasonable match to the calculated in-cylinder pressure, however, inaccuracies in the location and value of the peak pressure can be found in the calculated in-cylinder pressure as seen in Figure 5.16.

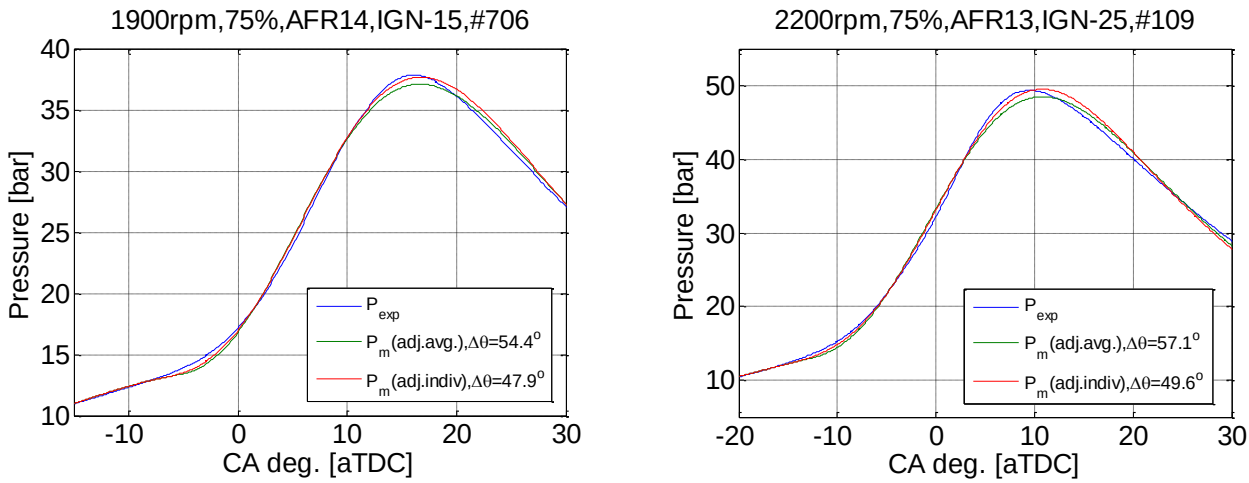

(a) (b)

Figure 5.16 Experimental and model predicted in-cylinder pressure of ensemble averaged and individually adjusted end angle of heat release calculation at 1900RPM, 75% load, AFR14 and ignition timing at -15 aTDC and 2200RPM, 75% load, AFR 13 and ignition timing -25aTDC

5.4.2 Wiebe Function-based End Angle Determination

Another method to find the optimal end angle for the heat release calculation, based on the Wiebe function, was investigated. The approach was based on the assumption that the Wiebe function characterizes the combustion profile well and the combustion profile at the end of combustion will be predicted reasonably, if the cumulative heat release rate until the end of combustion is well characterized by the Wiebe function. The optimal end angle of the heat release calculation was determined at the minimum value of sum squared errors between calculated and Wiebe function curve-fitted cumulative heat release rate.

Figure 5.17 shows the cumulative heat release rate (solid lines) and Wiebe function curve-fitted results (dashed lines) for a range of end angles. The range of end angle tested was from 20 crank angle past the point that has the maximum value of pV^1, decreasing in 1 crank angle increments. Only three different end angle are shown in Figure 5.17 for clarity. For a knock-free cycle, the cumulative heat release rate data from CA2 to CA95 was used to curve-fit.

To avoid bias of rapid pressure increase of knock, CA2 to *CA@KO* was used for knocking cycles to curve-fit the cumulative heat release rate. It is shown in the Figure 5.17 that the calculated and Wiebe function curve-fitted cumulative heat release rates match well up to CA80 and separate from CA80 to the end of combustion. The optimal end angle will be the case with minimal differences mostly during the end of combustion.

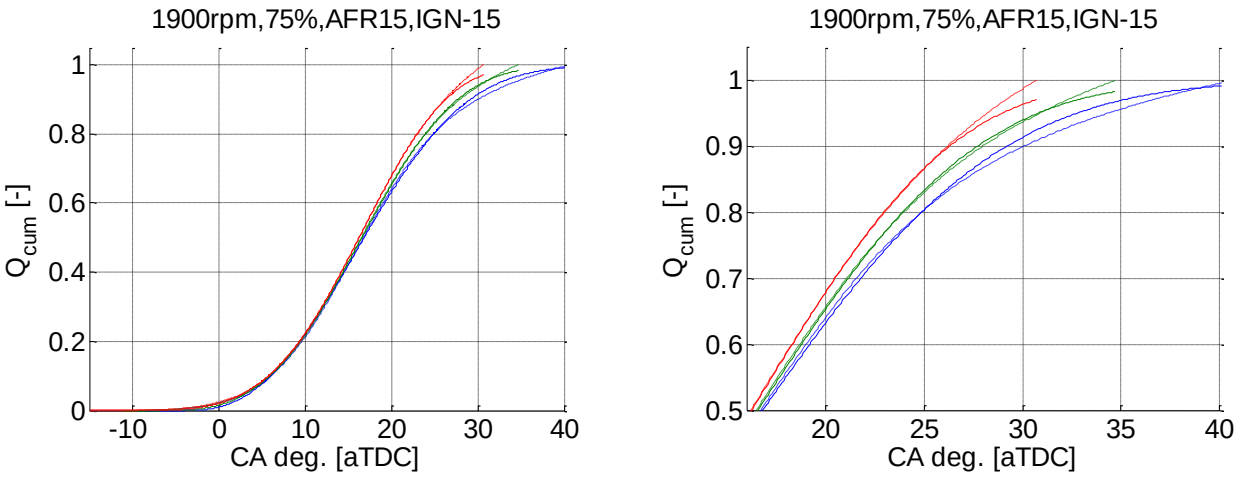

(a) (b)

Figure 5.17 Comparison of cumulative (solid) and Wiebe function curve-fitted (dashed) cumulative heat release rate for different end angle at 1900RPM, 75% load, AFR15 and ignition timing at -15 aTDC

The optimal end angle of heat release calculation was determined by finding the minimum sum squared error values calculated as shown in the equation (5.11). Figure 5.18 (a) shows the sum squared error values as a function of the end angle of the heat release calculation. To calculate the sum squared error values in the equal number of data points, the calculated and curve-fitted cumulative heat release rate data were spline fitted to the same 50 data points for a range of end angle. Figure 5.18 (b) shows the comparison of experimental and model-predicted in-cylinder pressure calculated by using an individually adjusted and Wiebe function-based end

angle of heat release calculation. The Wiebe function parameters and heat transfer multiplier for each end angle were calculated individually. It is shown in the Figure 5.18 (b) that the pressure calculated by using the Wiebe function-based end angle (red) matches the experimental pressure (blue) from the initial combustion development to the peak pressure well, while a pressure disagreement around TDC and at the peak pressure are seen by the individually adjusted end angle (green) case.

$$SSE = \sum_{CA2}^{CA95\ or\ CA@KO}(Q_{cum,calc} - Q_{cum,Wiebe})^2 \quad (5.11)$$

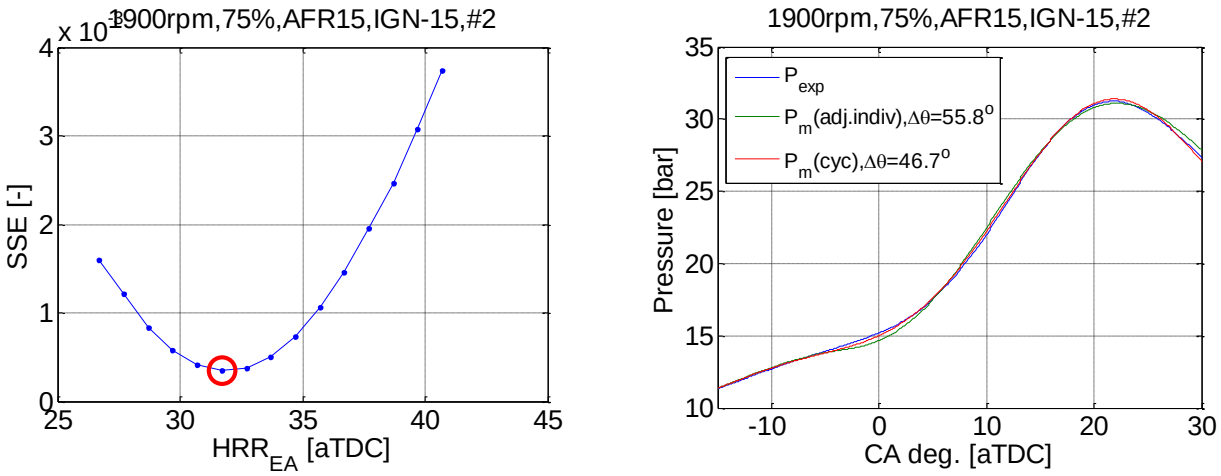

(a) (b)

Figure 5.18 (a) Determination of Wiebe function-based end angle and (b) Experimental and model predicted in-cylinder pressure using individually adjusted and Wiebe function-based end angle of heat release calculation at 1900RPM, 75%, AFR15 and ignition timing -15 aTDC

Figure 5.19 shows comparisons of experimental and model-predicted in-cylinder pressure using ensemble averaged, individually determined and the Wiebe function-based end angle for the heat release calculation for the same cycles previously discussed in the Chapter 5.4.1 (see Figure 5.16). It is seen in Figure 5.19 that the initial pressure development, rapid increase and the location and value of the peak pressure were best matched with the end angle determined by

the Wiebe function-based method (P_{cyc}) for two different operating conditions. Figure 5.20 shows the cumulative heat release rate (a) and in-cylinder pressure (b) at the operating condition with severe knock. Two cycles with significantly different combustion phasing were chosen to verify the accuracy of Wiebe function-based end angle of heat release calculation. Knock onset for each cycle are marked as red open circles. It is seen in the Figure 5.20 (a) that a good match between detailed cumulative heat release rate and the rate characterized by the Wiebe function parameters was found for both cycles from ignition to knock onset. The calculated cumulative heat release rates after knock onset are significantly affected by the rapid pressure increase, which is detached from the curve-fitted cumulative heat release rates. It is seen in the Figure 5.20 (b) that predicted in-cylinder pressure matches well from ignition timing to knock onset for both cycles.

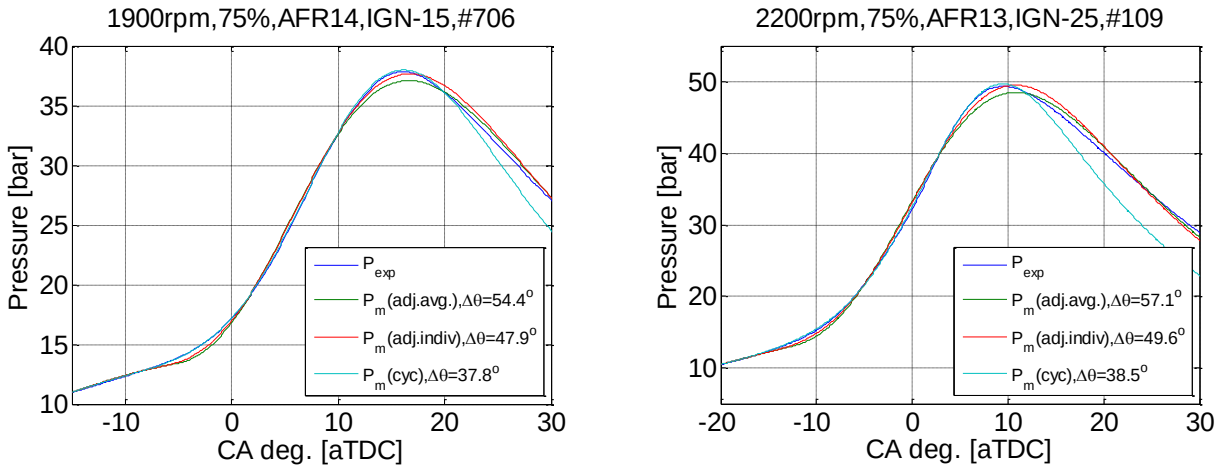

(a) (b)

Figure 5.19 Experimental and model predicted in-cylinder pressure using ensemble averaged, individually adjusted and Wiebe function-based end angle of heat release calculation

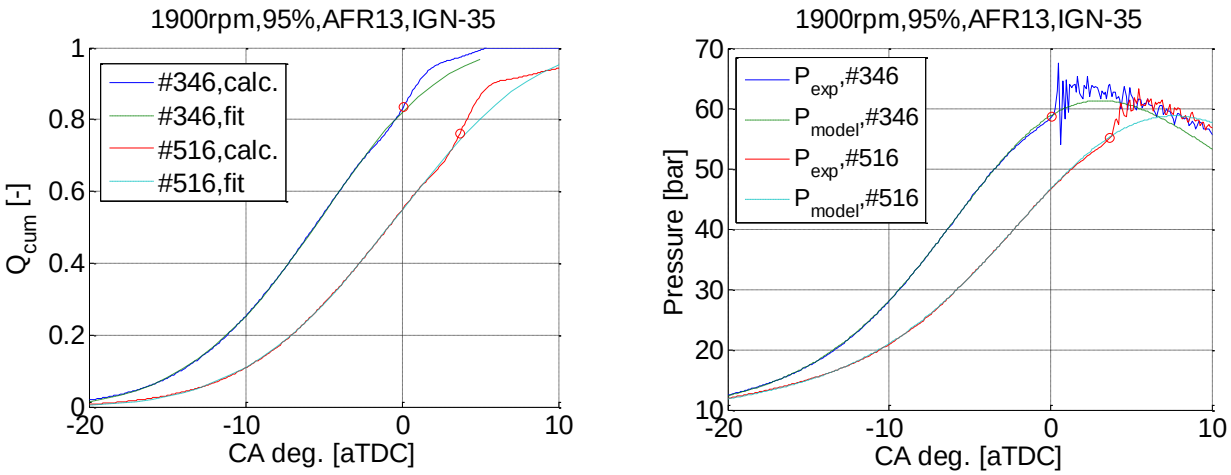

(a) (b)

Figure 5.20 (a) Calculated and curve-fitted cumulative heat release rate and (b) experimental and model predicted in-cylinder pressure comparison at 1900RPM, 95% load, AFR13 and ignition timing -35 aTDC

5.5 Heat Release Calculation Results

The unburned mass fraction at knock onset data was determined by using the new knock onset detecting method described in Chapter 4 and heat release rate calculation method discussed in Chapter 5. To minimize noise and filtering effects on the determination of the unburned mass fraction at knock onset, the cumulative heat release rate calculated by the curve-fitted Wiebe function parameter method outlined in section 5.4.2 was used.

Figure 5.21 show the correlation between the MAPO knock intensity and unburned mass fraction at knock onset determined by using Wiebe function-based (a) and ensemble averaged value of pressure and volume-based (b) end angle of heat release calculation at two different operating conditions. A significant difference of the correlation between two different methods of determining end angle is seen in the Figure 5.21. Assuming the severity of knock would be highly correlated with the energy that is released at knock onset, a reasonable correlation is seen in the Figure 5.21 (a) that maximum MAPO knock intensity increases as the value of unburned mass fraction at knock onset increases, while the highest MAPO values are found near the middle of unburned mass fraction range seen in the Figure 5.21 (b). A more detailed discussion and the knock intensity correlation will be discussed in Chapter 7.

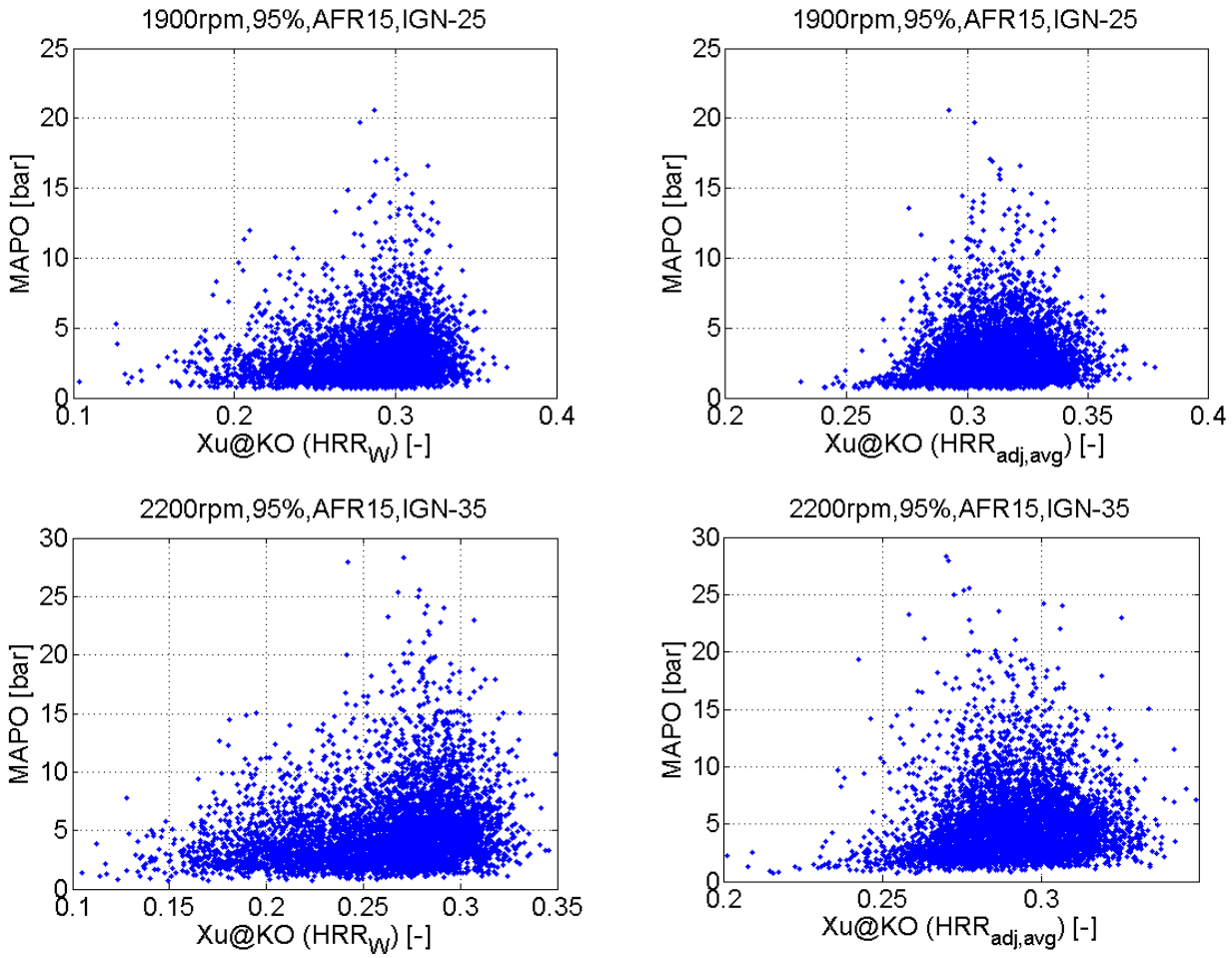

(a) (b)

Figure 5.21 Unburned mass fraction determined by ensemble averaged and Wiebe function-based end angle heat release rate calculation and MAPO knock intensity correlation

Chapter 6 Cyclic Variation Model

Cyclic variation is largely a result of random turbulent motion during flame development, and the subsequent flame propagation. Modeling the turbulent fluctuations and not just a statistical representation of them, however, requires a large amount of computational time. Instead of modeling all of the physics, a simple model that characterizes the overall combustion profile, in which turbulent effects are already included, is pursued to predict the statistical distribution of a large number of cycles. The Wiebe function is the most widely used functional form to simulate the burn rate [73]. In this research, mass burn fractions calculated from experimental results were curve-fitted to the Wiebe function. It was found that the Wiebe function parameters were inter-related, and this inter-relation is used to provide a set of randomly generated Wiebe function parameters that correctly characterize the cyclic variation. A universal cyclic variation model was developed to generate a set of Wiebe function parameters at a given operating condition with a reasonable accuracy.

6.1 Wiebe Function Curve-fit

6.1.1 Wiebe Function and Curve-fit

The averaged mass burn fraction data, calculated from the ensemble averaged in-cylinder pressure, listed as X_b in equation (6.1) and its crank angle in radians is used to find four Wiebe function parameters: b, m, θ_{ig} and θ_{comb}. The Wiebe function parameters were initialized as b=4, m=2.25, θ_{ig} as ignition timing and θ_{comb} as 45 crank angle degrees for 1900 RPM cases. The value of b=4 corresponds with the mass burn fraction of 0.9816 at completed combustion, and m=2.25 corresponds with the burn fraction 0.5 at the maximum burning rate as discussed in the Chapter

2.3. The curve-fitted Wiebe function parameters were determined by using MATLAB function *lsqcurvefit* with the *Levenberg-Marquardt* algorithm, which is also known as the damped least-squares method. There were no upper or lower bounds placed on the Wiebe function parameters. The cumulative heat release rate data from CA2 to CA90 were used to avoid biases associated with the data during the early flame development and at the end of combustion for a knock-free cycle. For a cycle with knock, CA2 to the mass burn fraction at knock onset was used to avoid biases in the pressure data after knock onset. The best-fit parameters for the ensemble averaged mass burn fraction for the case described are listed in Table 6-1. The best-fit Wiebe function is shown as a solid line in Figure 6.1, and shows a good agreement with the experimental mass burn fraction; the Wiebe function is able to correctly model the burn rate of a normal SI combustion event

$$X_b = 1 - \exp\left[-b\left(\frac{\theta-\theta_{ig}}{\theta_{comb}}\right)^{m+1}\right] \tag{6.1}$$

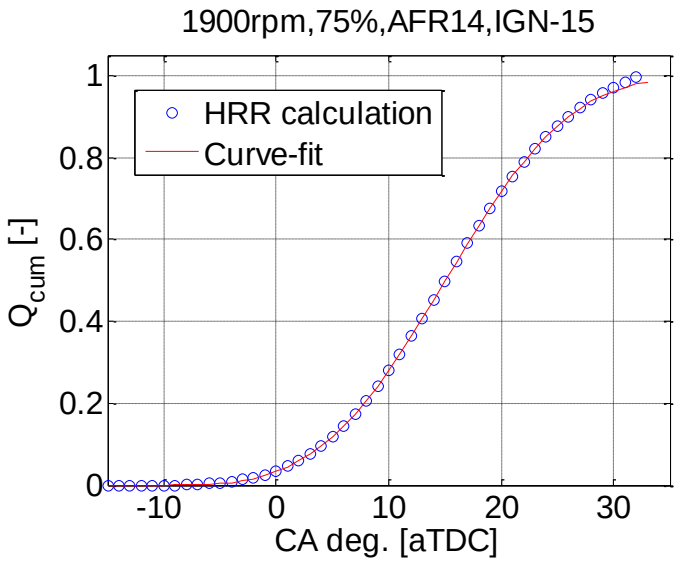

Figure 6.1 Average mass burn fraction and curve fitted Wiebe function at 1900 RPM, 75% load, AFR 14 and ignition timing -15 aTDC

Table 6-1 Curve-fitted Wiebe function parameters at 1900 RPM, 75% load, AFR 14 and ignition timing -15 aTDC

Wiebe function parameter	Value
b [-]	4.03
m [-]	1.97
Θ_{ig} [aTDC]	-8.33
Θ_{comb} [CA deg.]	42.62

6.1.2 Suitability of Wiebe Function for Irregular Cycles

The Wiebe function characterizes a normal combustion profile well. For a cycle that varies significantly compared to the ensemble averaged data, the calculated heat release rate will be significantly different. The ability of a curve-fitted Wiebe function to model a cycle with an irregular pressure development will be assessed.

Irregular cycles have a significantly different curve-fitted Wiebe function parameters. Figure 6.2 (a) shows the heat release rate and in-cylinder pressure comparison for two consecutive cycles. The Wiebe function parameter m for cycle #794 showed the maximum value at the given operating condition (from total 1,000 cycles). It is seen in Figure 6.2 (a) that cycle #794 is a slower developing cycle and the $CA@_{dXbmax}$ is later than cycle #795. It was discussed in Chapter 2.3 (equation 2.60), $CA@_{dXbmax}$ is only a function of the Wiebe function parameter m. To match the overall combustion profile when m is large, θ_{ig} should be advanced further and θ_{comb} should be increased. Table 6-2 shows that the curve-fitted Wiebe function parameters m and θ_{comb} for cycle #794 are significantly higher than the value of the ensemble average case, and θ_{ig} is advanced even before the physical ignition timing. It is shown in the Figure 6.2 (b) that the thermodynamic engine model-predicted pressure is not matched well with the experimental data between -10 aTDC to 5 aTDC for the cycle #794, while cycle #795 shows a good match over all crank angles. Based on the inter-relation between the Wiebe function parameters, setting a threshold for one Wiebe

function parameter could effectively identify the irregular cycles. A threshold value of 10 CA degrees before the ignition timing for θ_{ig} will be used to exclude irregular cycles in the analysis of Wiebe function parameter distribution. With this constraint, it was found that the Wiebe function was able to capture a wide range of irregular combustion events.

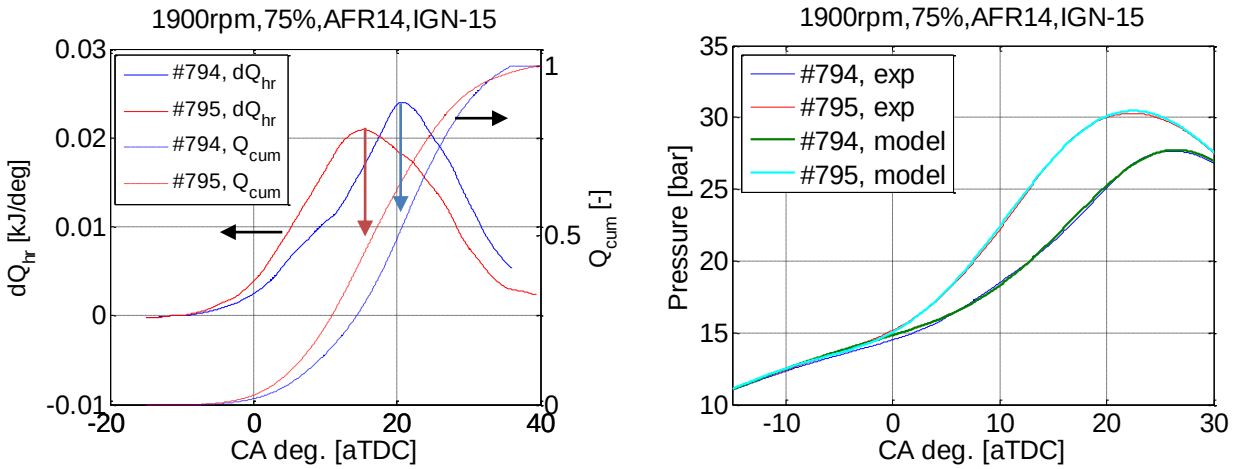

(a) (b)

Figure 6.2 Heat release rate and cumulative data and in-cylinder pressure comparison between experiment and the model calculation at 1900RPM, 75% load, AFR14 and ignition timing at -15 aTDC

Table 6-2 Curve-fitted Wiebe function parameters of cycles #794 and #795 at 1900RPM, 75% load, AFR14 and ignition timing at -15 aTDC

	b [-]	*m* [-]	Θig [aTDC]	Θcomb [CA deg.]
#794	3.9824	5.8235	-31.3594	66.5839
#795	4.0125	2.0804	-8.5315	44.7133
Ensemble Avg.	4.0049	2.2754	-9.9140	42.5534

6.1.3 Single-Cycle Wiebe Function Parameters

Probability density functions (PDFs) of the best-fit Wiebe function parameters are plotted in Figure 6.3 for the fitting the range of CA2 to CA90 for 5,000 consecutive cycles. The Wiebe function parameter *b* shows a much smaller range compared to the other parameters, which suggests that using the Wiebe function parameter *b* calculated from the ensemble averaged pressure can reduce the number of parameters required to characterize each cycle. As discussed in Chapter 2.3, the Wiebe function parameter *b* is closely related to the value of cumulative heat release rate at the end of combustion. It is a reasonable conclusion that the cyclic variation would have a minimal effect on the value of Wiebe function parameter *b*.

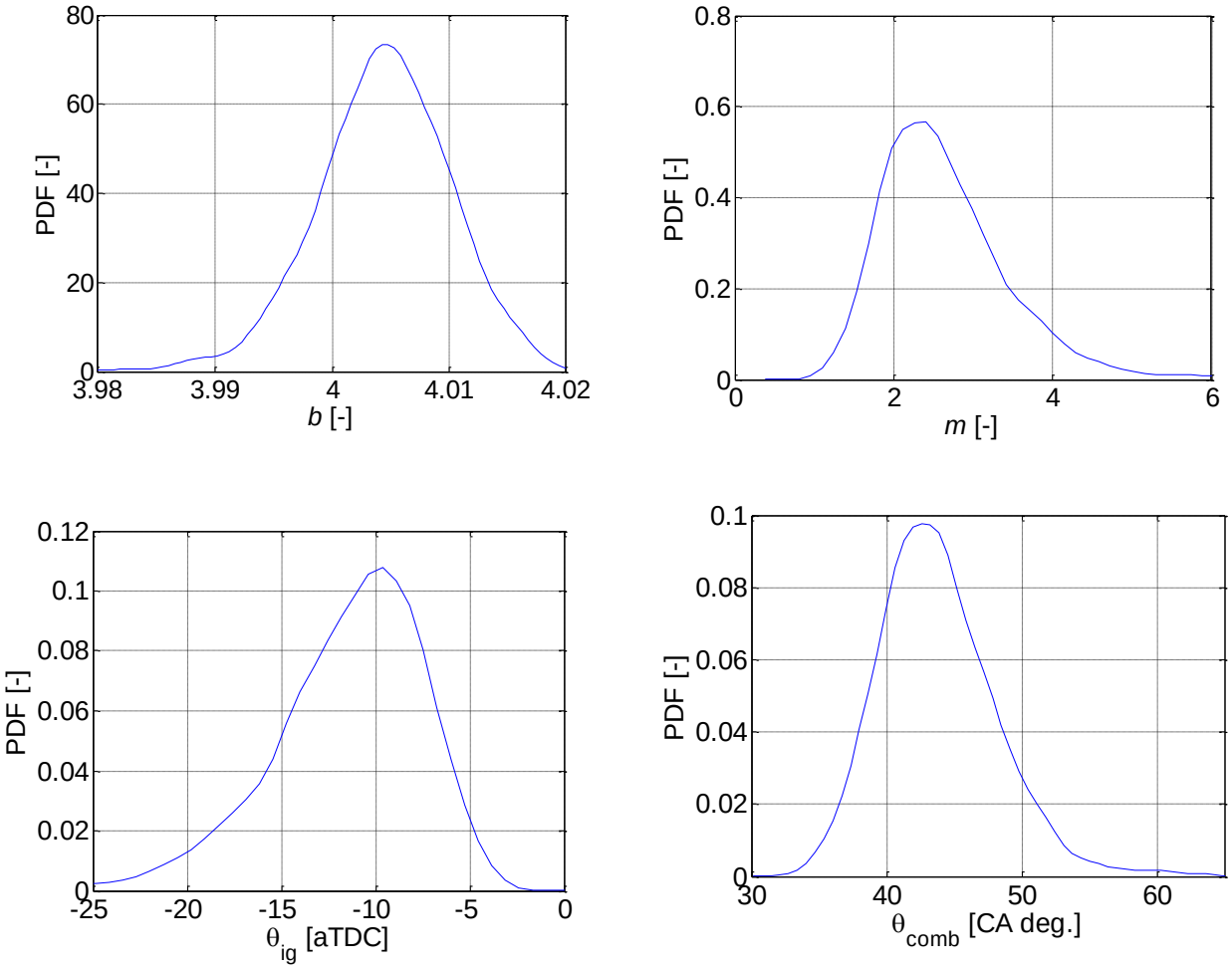

Figure 6.3 Distribution of the curve-fitted Wiebe function parameters at 1900RPM, 75%, AFR14 and IGN-15 aTDC

A comparison of the four-parameter and three-parameter Wiebe function (by using the ensemble averaged Wiebe function parameter *b*) fits was performed using the in-cylinder pressure calculated by the thermodynamic engine model. CA10, CA50 and CA80 calculated from the heat release analysis of the calculated in-cylinder pressure for four- and three-parameter Wiebe function are plotted in Figure 6.4 to verify the accuracy of using a fixed value of *b*. Figure 6.4 shows that there are no significant differences between using four- or three-parameter Wiebe function to

characterize the combustion profile of each cycle. CA10, CA50 and CA80 between the model and experimentally calculated values are reasonably well matched for 5,000 consecutive cycles.

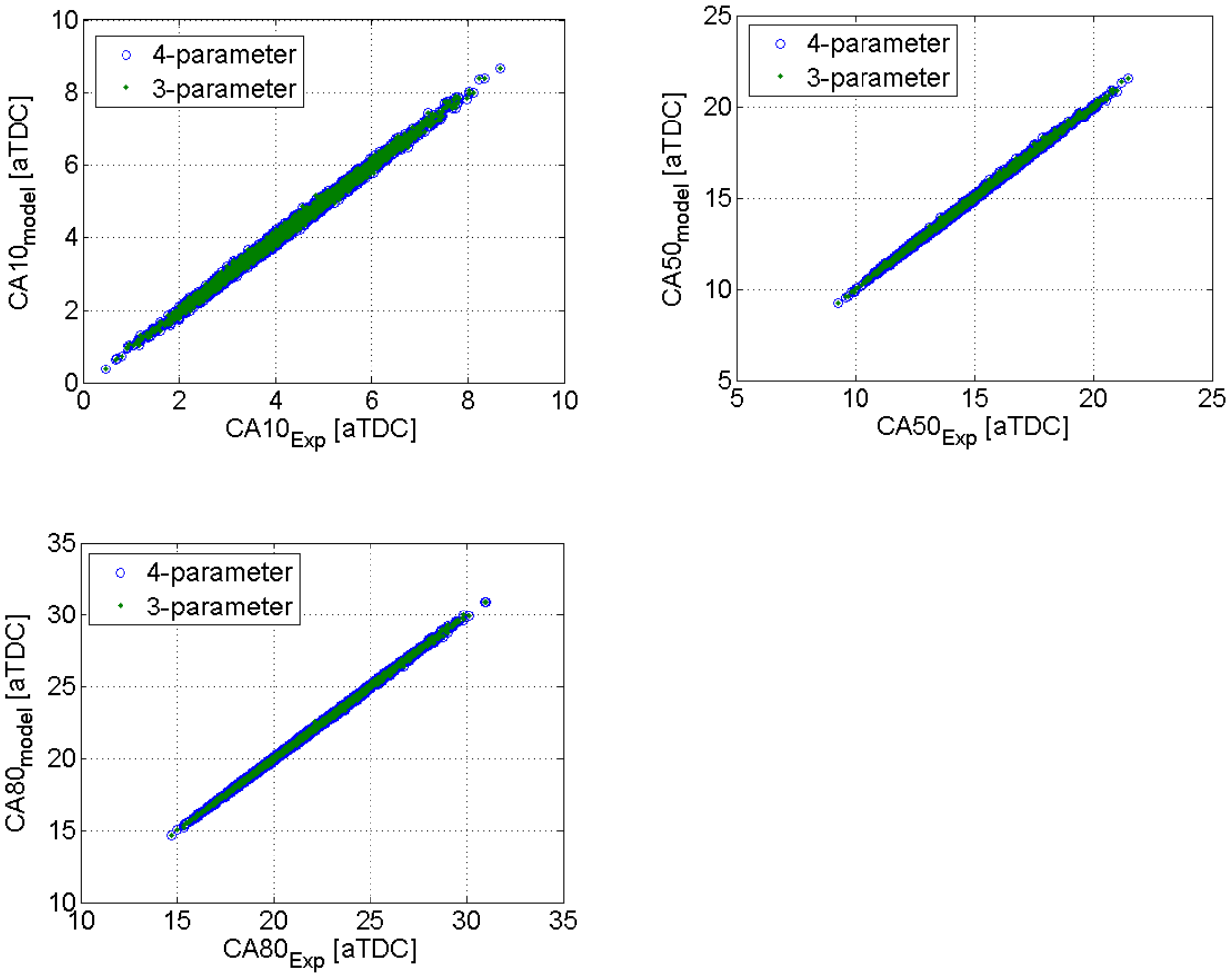

Figure 6.4 CA10, CA50 and CA80 comparison between the thermodynamic engine model and experimental results at 1900 RPM, 75% load, AFR14 and ignition timing at -15 aTDC

6.1.4 Wiebe Function Curve-fit Results

CA10, CA50 and CA80 results calculated by the thermodynamic engine model for different operating conditions are plotted in Figure 6.5. The model and experimental results for different

ignition timing, AFRs and load were well matched with the differences less than 2 crank angle degrees.

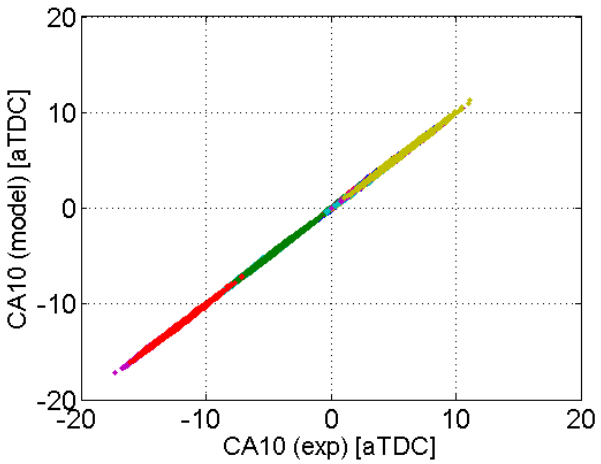

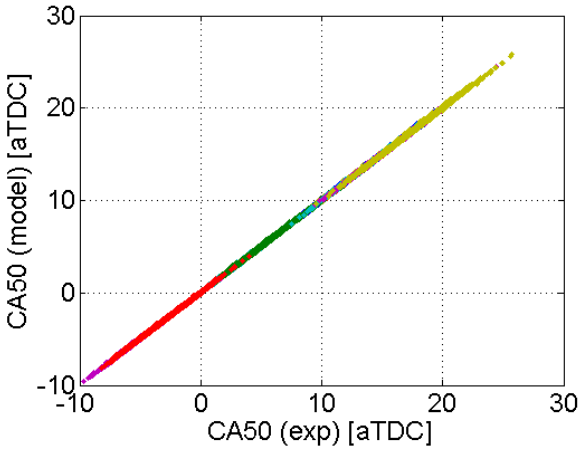

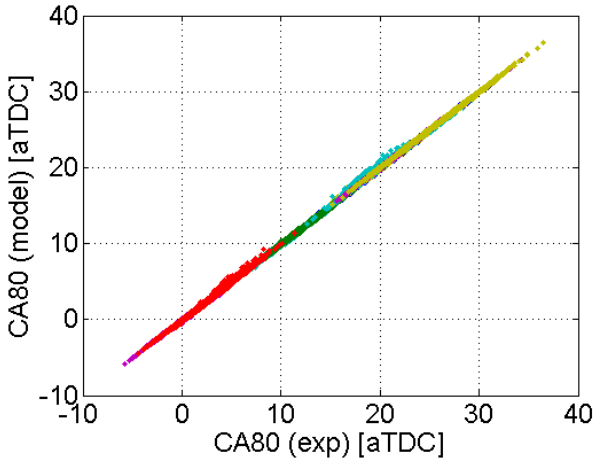

Load [%]	AFR [-]	Ignition [bTDC]
95	13	15
85	13	15
75	13	15
75	13	25
75	13	35
95	14	15
85	14	15
75	14	15
75	14	25
75	14	35
95	15	15
85	15	15
75	15	15

Figure 6.5 CA10, CA50 and CA80 results between experimental and the model results at 1900RPM with change of load, AFR and ignition timing. Colors of symbols represents each operating conditions listed in the table.

6.2 Monte-Carlo simulation

6.2.1 Inter-related Wiebe Function Parameters

The Wiebe function parameters are constrained by the equation 6.1 to find the best fit (minimum residual value) to the experimental mass burn fraction. For a slow-burning cycle at the given operating condition, m and θ_{comb} should be larger so that the mass burn fraction decreases relative to the ensemble averaged cycle. Unlike m and θ_{comb}, θ_{ig} should be increased since the numerator in the exponential term of the Wiebe function should be larger to result in a smaller mass burn fraction, which leads to the slow burning cycle. This suggests that there is a correlated relationship between the Wiebe function parameters and that just randomly choosing values from distributions like those shown in Figure 6.3 will be inadequate. The curve-fitted Wiebe function parameters of 5,000 consecutive cycles are plotted in Figure 6.6, as a function of θ_{ig}. A positive correlation between m and θ_{comb} and θ_{ig} can be seen in Figure 6.6.

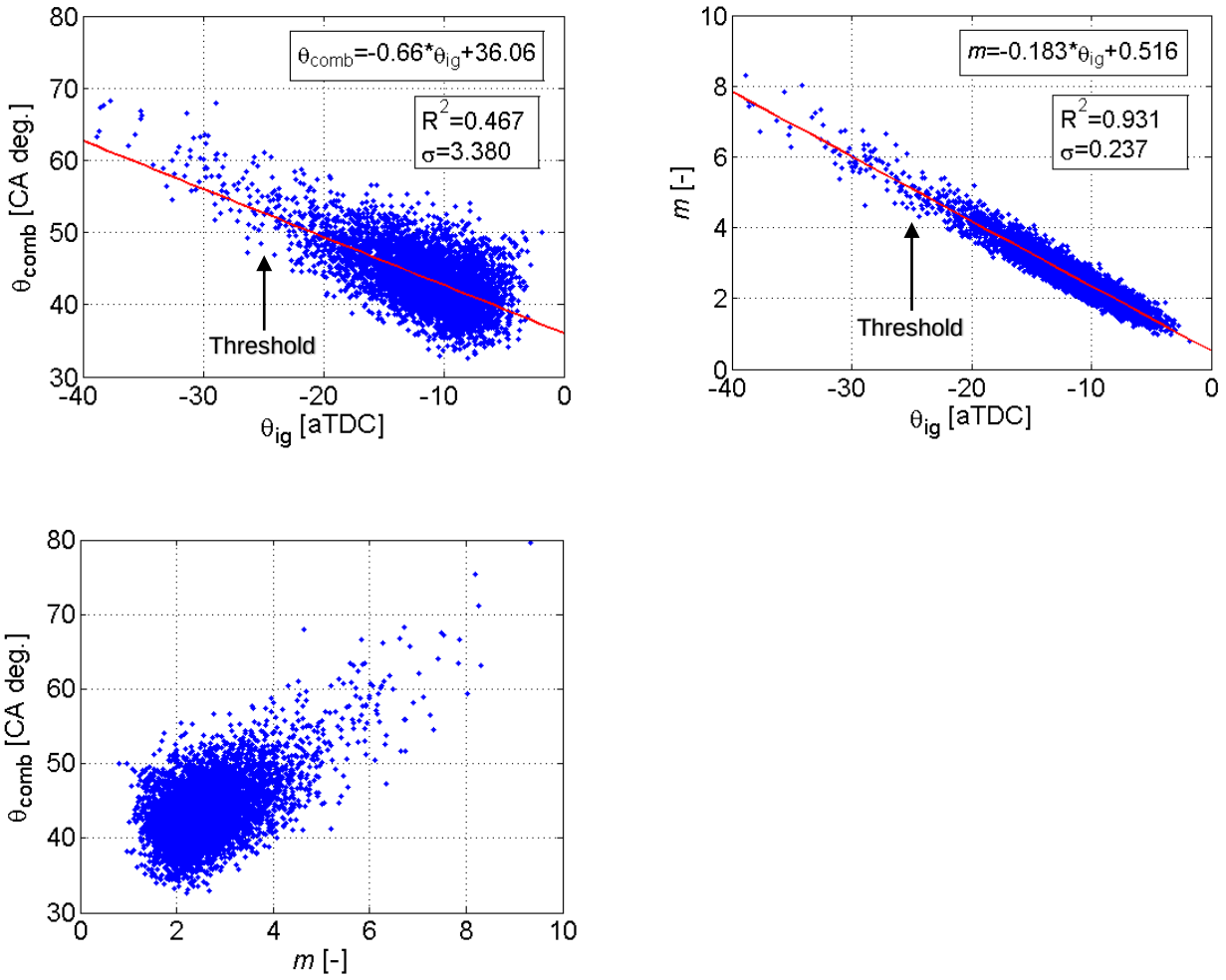

Figure 6.6 Inter-relation between the curve-fitted Wiebe function parameters and their linear correlation at 1900 RPM, 75% load, AFR14 and ignition timing at -15 aTDC

6.2.2 Wiebe Function Parameter Generation for Monte-Carlo Simulation

To randomly select a set of Wiebe function parameters, θ_{ig} is first selected randomly from its cumulative density function (CDF) as shown in Figure 6.7. A threshold value of 10 crank angle degrees advanced from ignition timing was used to avoid including highly irregular cycles. The inclusion of the threshold value resulted in eliminating 94 cycles from the 5,000 consecutive cycles. The number of cycles excluded was about 5% for most operating conditions; advanced operating

conditions with severe knock conditions could have up to 10%. The parameters m and θ_{comb} are then calculated based first on the linear fit to θ_{ig} see Figure 6.6.

Figure 6.8 shows the variation of the Wiebe function parameters m and θ_{comb} about the nominal value defined by the linear fit to θ_{ig} (solid), and a normal distribution fitted PDF (dashed) for a range of operating conditions. It is shown in the Figure 6.8 that the variation of the parameters m and θ_{comb} to the linear fit to θ_{ig} follows a Gaussian distribution.

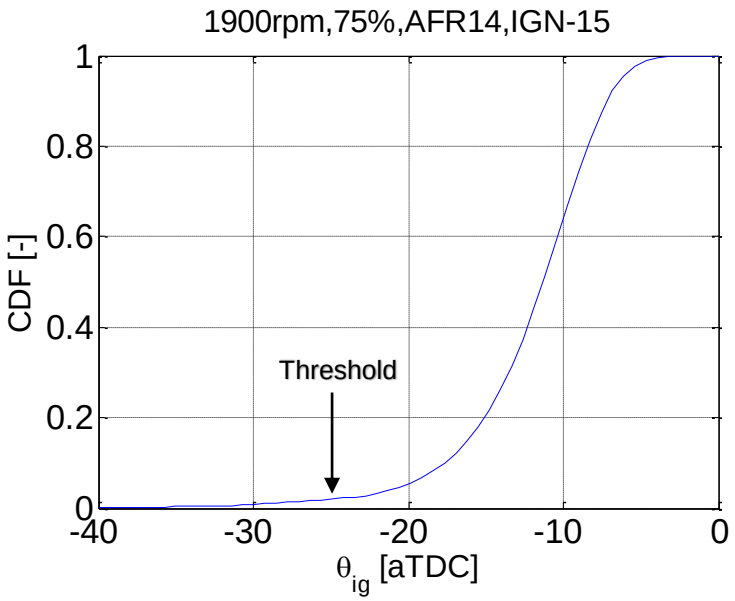

Figure 6.7 CDF of curve-fitted Wiebe function parameter Θig at 1900 RPM, 75% load, AFR14 and ignition timing -15 aTDC

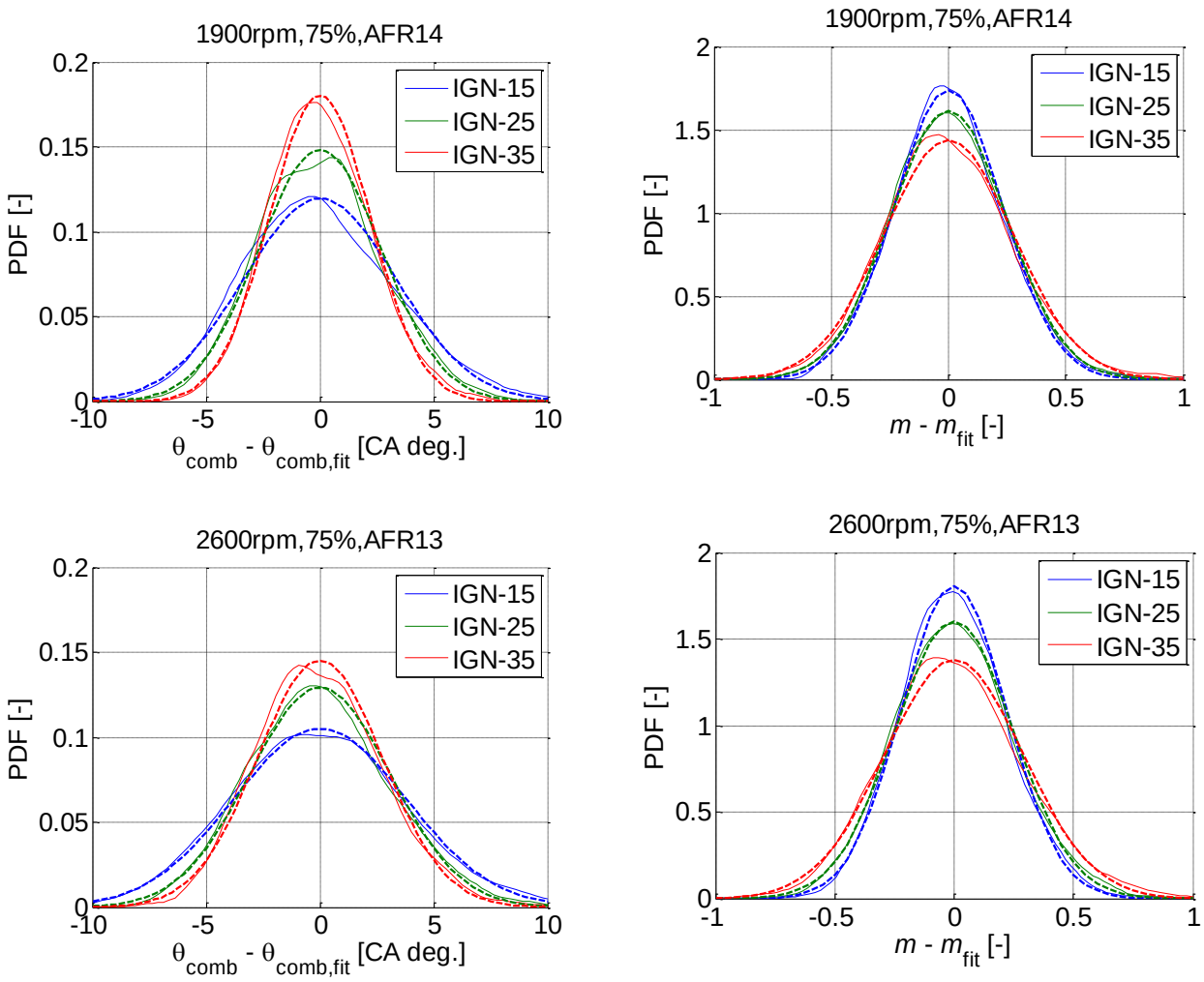

Figure 6.8 Variation of the Wiebe function parameter m and θ_{comb} and normal distribution fitted PDF calculated from the linear fit to θ_{ig}

The values of m and θ_{comb} for the operating condition of Figure 6.6 were found after randomly selecting θ_{ig} as described above using

$$m = -0.183 * \theta_{ig} + 0.516 + \text{normrnd}(0,\ 0.237) \tag{6.2}$$

$$\theta_{comb} = -0.660 * \theta_{ig} + 36.06 + \text{normrnd}(0,\ 3.380) \tag{6.3}$$

where *normrnd* is the MATLAB function for randomly choosing from a Gaussian distribution.

Figure 6.9 shows a comparison of the experimental Wiebe function parameters and those randomly generated by using the Monte-Carlo simulation. The number of randomly generated set of Wiebe function parameters shown in the Figure 6.9 were 8,000 cycles. It is seen in Figure 6.9 that the distribution and probability of the randomly generated Wiebe function parameters are well matched to the curve-fitted parameters that characterizes the combustion profile at the given operating condition.

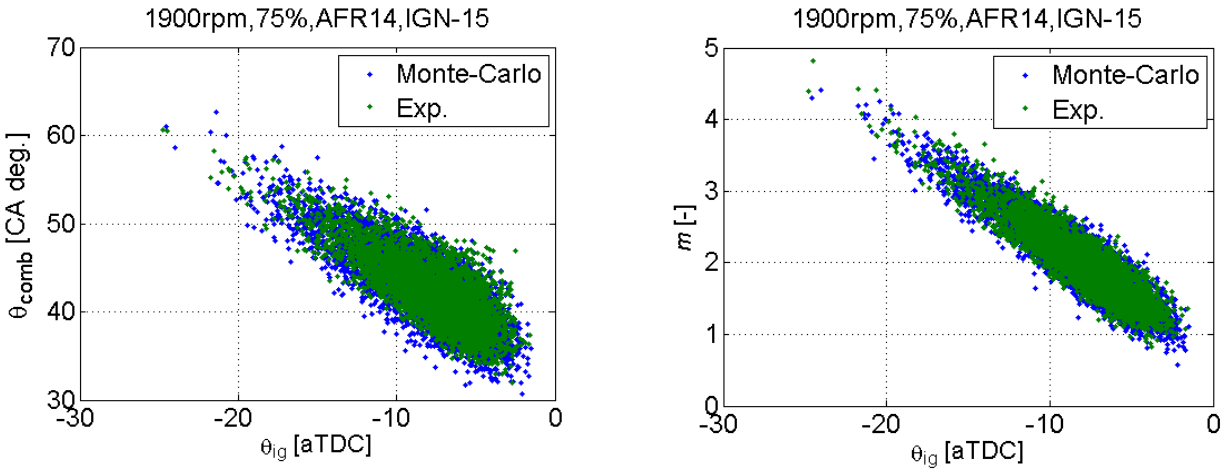

(a) (b)

Figure 6.9 Comparison of Wiebe function parameter between curve-fitting experimental data and randomly generated from Monte-Carlo simulation of 8,000 cycles at 1900RPM, 75% load, AFR14 and ignition timing -15 aTDC

6.2.3 Cyclic Variation Model Results

In-cylinder pressure were calculated for an advanced and retarded spark timing case using the cyclic variation model coupled with the Monte-Carlo simulation approach for different numbers of samples. CA10 and CA50 were determined through heat release analysis of the calculated pressure. PDFs of CA10 and CA50 for these randomly generated cycles are plotted in Figure 6.10. The maximum number of randomly generated Wiebe function parameters was 8,000; convergence

was achieved with approximately 2,000 random selections. The PDFs of CA10 and CA50 are well matched to the experimental results for the two different ignition timings. The retarded spark timing case was mostly non-knocking cycles and the advanced case included intermediate engine knock for number of cycles.

The cyclic variation at the given operating condition, from non-knocking cycle to knocking cycle, was effectively characterized using the 3-parameter Wiebe function. The calculation time to predict in-cylinder pressure of 8,000 cycles was 200 seconds using a desktop computer.

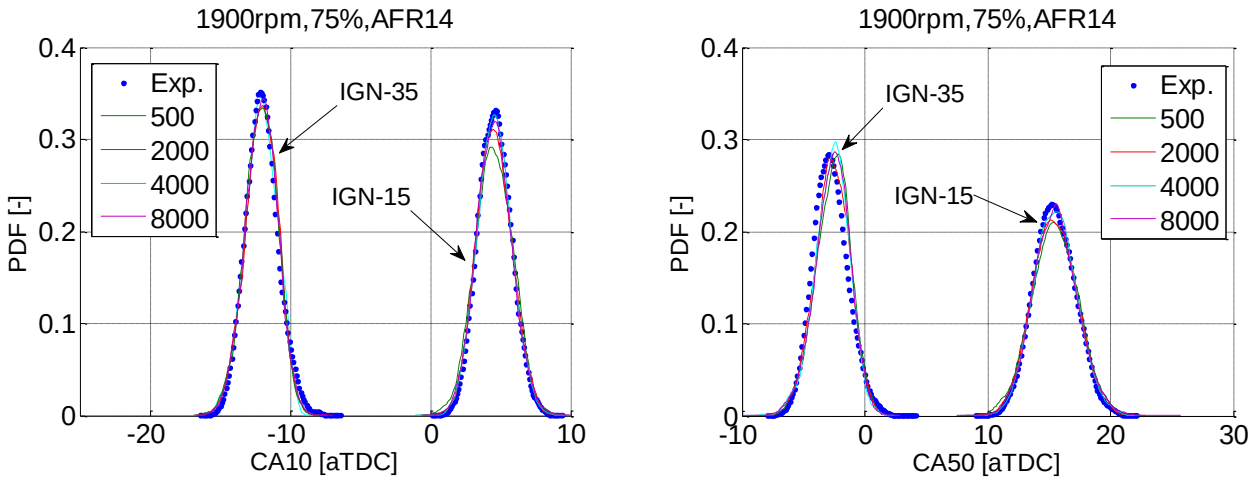

(a) (b)

Figure 6.10 PDFs of CA10 and CA50 at 1900 RPM, 75% load, AFR14 and ignition timing -15 and -35 aTDC from different number of Monte-Carlo simulation

6.3 **Universal Cyclic Variation Model**

The results from 80 different operating conditions were used to find correlations for building a more universal cyclic variation model, i.e., one that did not require experimental data as an input. Figure 6.11 shows the linear fit of $\Delta\theta$ and m to θ_{ig} for operating conditions with 4 different speeds, 3 different loads, 3 different AFRs and 3 different ignition timings. The slope and offset of the

linear fit were investigated to find a universal correlation to the operating conditions. No significant correlations were found with RPM, load and AFR for both slope and offset. The ignition timing showed a weak correlation to the slope for both $\Delta\theta$ and m, and strong correlations were found for the offset of the linear correlation. Wiebe function parameter θ_{ig} corresponds with the timing of initial flame development, which should be generally determined by the ignition timing. It is a reasonable conclusion to find the correlation to predict the slope and offset as a function of the ignition timing.

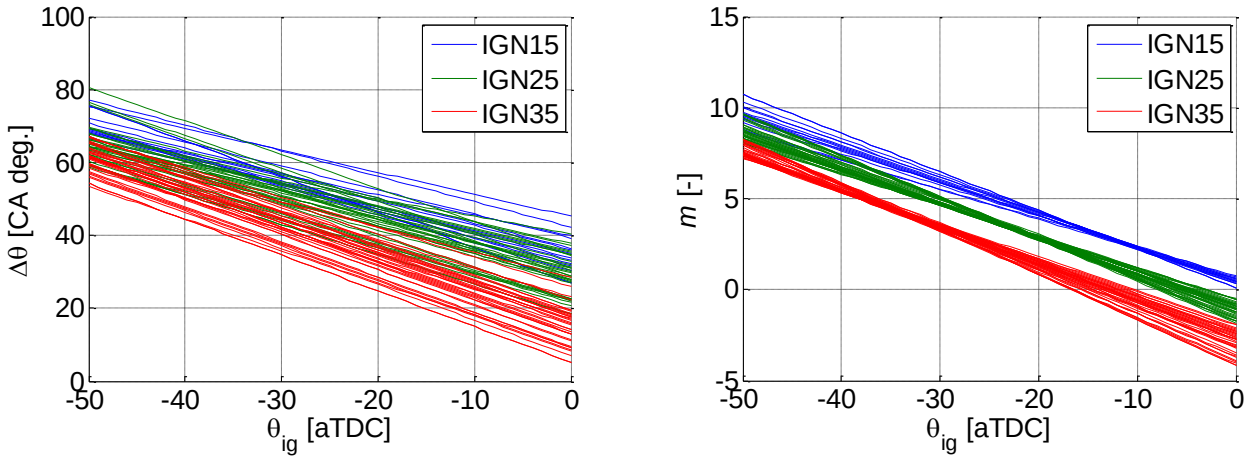

(a) (b)

Figure 6.11 Linear fit of Wiebe function parameters $\Delta\theta$ and m to θ_{ig}

A "Universal" distribution of θ_{ig} was determined from 80 different operating conditions. The Wiebe function parameter θ_{ig} values more than 10 CA degrees advanced from the ignition timing were excluded. Figure 6.12 shows the PDF and CDF of θ_{ig} normalized by subtracting the ignition timing. The universal PDF of normalized θ_{ig} (magenta) was determined by curve-fitting all data using a generalized extreme value (GEV) distribution. The values of μ and σ found for the GEV distribution were 7.924 and 4.622. A good agreement for both the PDF and CDF is seen between

the universal distribution of the normalized θ_{ig}, determined by the GEV distribution, and ignition timing -25 and -35 aTDC in Figure 6.12. The retarded ignition timing case at -15 aTDC showed a 3 CA degrees shift of the PDF location. The value of θ_{ig} can be randomly selected from the universal distribution and then shifted based on the ignition timing of the each operating condition.

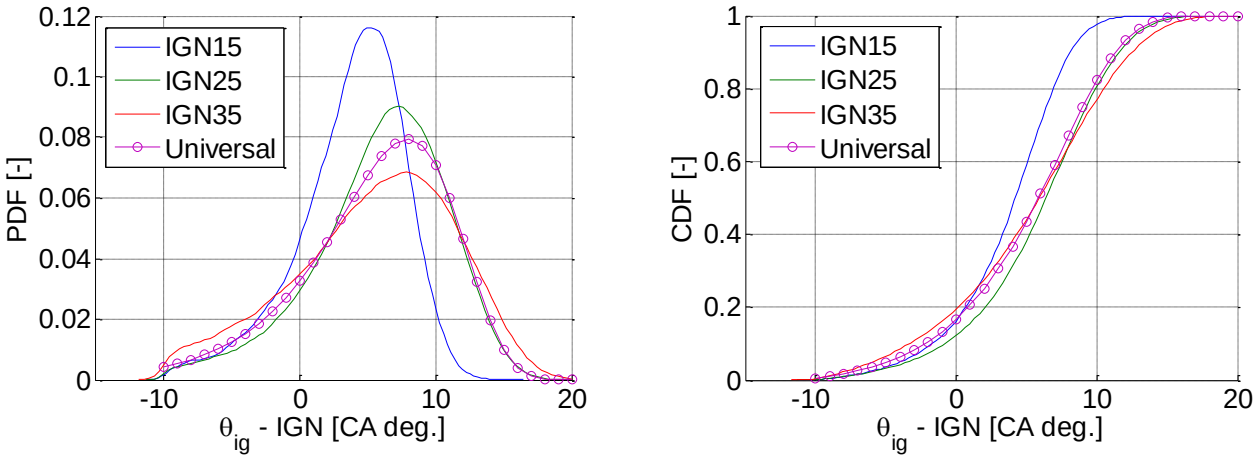

Figure 6.12 Universal PDF and CDF distribution of duration between θ_{ig} and ignition timing

Coefficients and correlations found from the linear fit of Wiebe function parameters to determine $\Delta\theta$ and m as a function of θ_{ig} are listed in Equations (6.4) and (6.5). All coefficients to determine the slope and offset of the linear fit were found as a function of the ignition timing. The ensemble averaged value of the slope between $\Delta\theta$ and θ_{ig} was used, because no significant correlation was found between any operating parameters. To add randomness in $\Delta\theta$ and m, a normal distribution of the difference between linear fit and $\Delta\theta$ and m values were assumed as discussed in section 6.2.2. The standard deviation of $\Delta\theta$ was determined as an average value of 80 different operating conditions, since the deviation only showed a weak correlation to engine speed. The standard deviation of m was linearly fit as a function of the ignition timing.

$$\Delta\theta = -0.8011 * \theta ig + (0.991 * IGN + 51.65) + normrnd(\mu_{comb}, \sigma_{comb}) \quad (6.4)$$

$$m = (0.0013 * IGN - 0.162) * \theta ig + (0.161 * IGN + 2.928) + normrnd(\mu_m, \sigma_m) \quad (6.5)$$

$$\mu_{comb} = 0,\ \sigma_{comb} = 3.4 \quad (6.6)$$

$$\mu_m = 0,\ \sigma_m = -0.0068 * IGN + 0.1188 \quad (6.7)$$

To verify the accuracy of the universal cyclic variation model, an operating condition that was not included in finding the coefficients listed in equations (6.4) - (6.7) was used to compare the distribution of Wiebe function parameters. Figure 6.13 (a) shows the comparison of the correlation between $\Delta\theta$ and θ_{ig} by finding the linear fit from the curve-fitted (green) and universally predicted (red) results. The maximum differences of the $\Delta\theta$ offset, between directly fitted and universally predicted, was about 5 CA degrees in the range between -35 to -15 aTDC, where most cycles exist, was seen in Figure 6.13 (a). Figure 6.13 (b) - (d) shows a comparison of the PDF of Wiebe function parameters between curve-fitted data and Monte-Carlo results of 5,000 random selections. It is shown in the Figure 6.13 that the location and width of PDFs for m and θ_{ig} are reasonably well matched. The location of $\Delta\theta$ is differ by 3 ~ 4 CA degrees, which corresponds with the difference in the offset shown in Figure 6.13 (a).

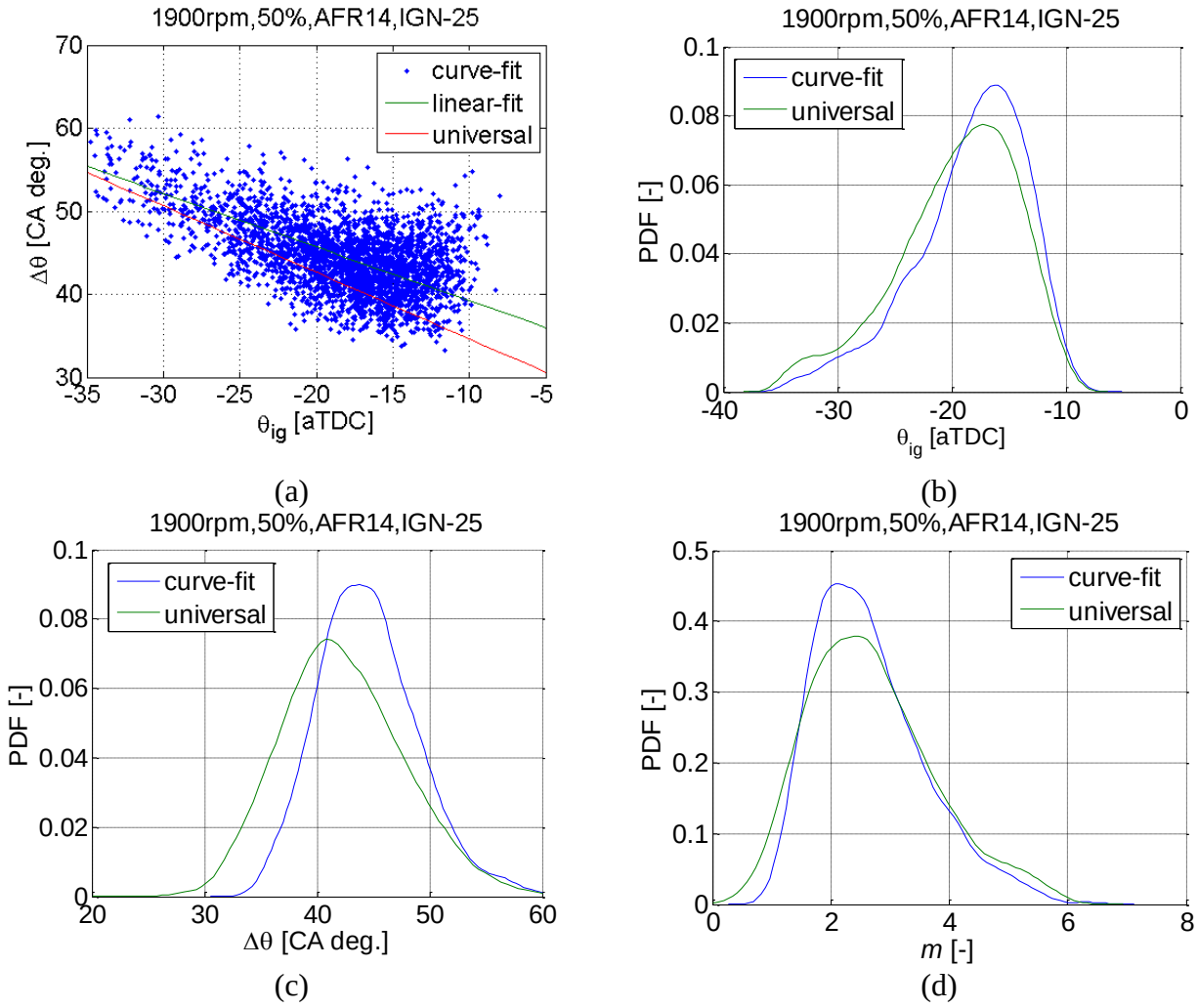

Figure 6.13 Universal cyclic variation model predicted Wiebe function parameters at 1900RPM, 50% load, AFR14 and ignition timing at -25 aTDC

To assess the accuracy of the universal cyclic variation model, CA10 and CA50 were calculated from the Wiebe function parameters. Figure 6.14 shows PDF of CA10 and CA50 calculated from experimental results and the Monte-Carlo simulation for different number of random selections. It is seen in Figure 6.14 that the predicted distribution was converged at 2,000 random selections. The widths of the CA10 and CA50 distribution were well predicted, however, the timing of the predicted PDFs for both CA10 and CA50 differed by 3 ~ 4 CA degrees, which matches with the differences of $\Delta\theta$ seen in Figure 6.13 (c).

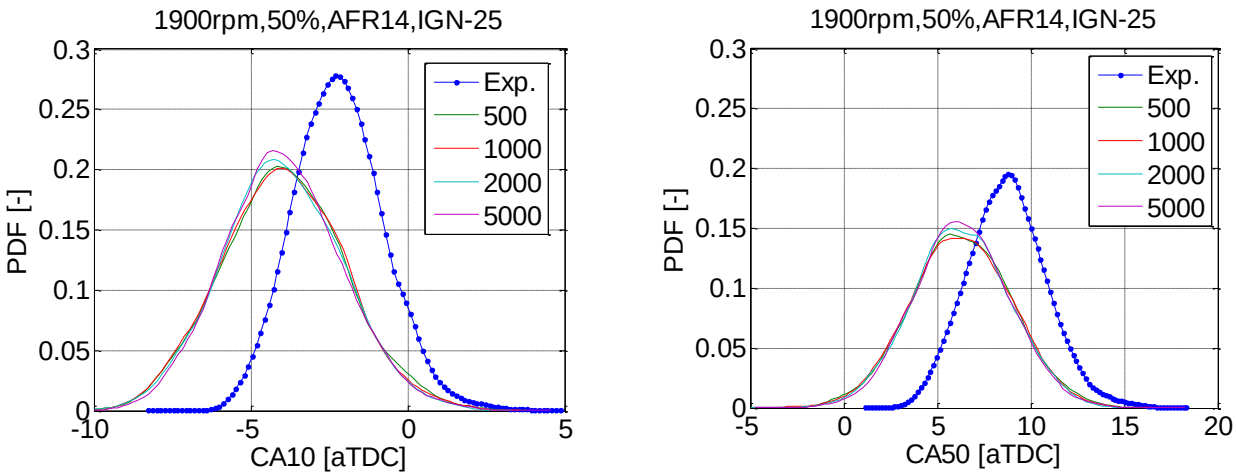

Figure 6.14 PDF of CA10 and CA50 comparison between experiment and universal cyclic variation model for different number of Monte-Carlo simulation at 1900RPM, 50% load, AFR14 and ignition timing at -25 aTDC

A multiple regression of the parameters was tested to enhance the accuracy of predicting the $\Delta\theta$ as a function of θ_{ig}. Figure 6.15 show PDFs of CA10 and CA50 predicted by adding engine operating parameters, AFR, load and RPM to perform multiple regressions. Only the offset of the linear correlation between $\Delta\theta$ and θ_{ig} was determined from the multiple regression and the same coefficients were used as listed in equations (6.4) - (6.7). It is shown in Figure 6.15 that by adding more parameters in the multiple regression, the location of the PDF matches the experimental results better. The offset for the linear correlation between $\Delta\theta$ and θ_{ig} can be predicted accurately by performing a multiple regression for operating parameters, however, the coefficients will be bounded with the experimental data and there will be no significant advantage of predicting the cyclic variation at an arbitrary condition with increased coefficients, which are best fitted to the experimental data.

(a)

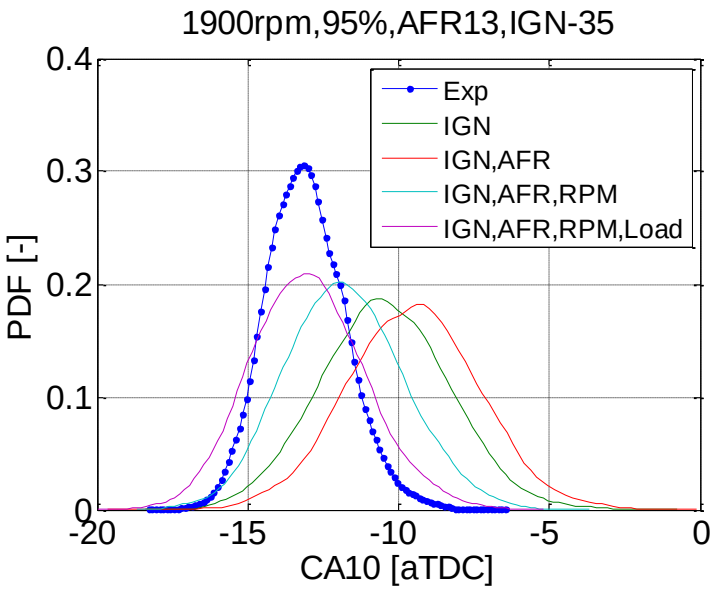

(b)

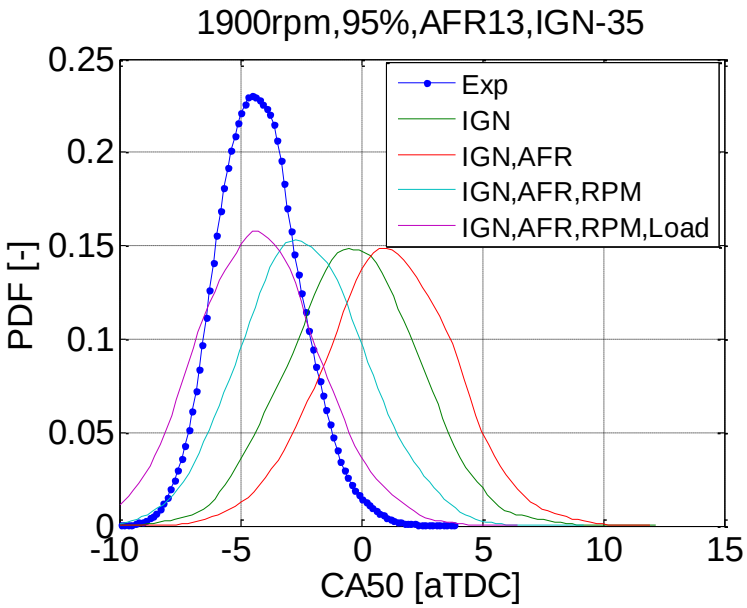

Figure 6.15 PDF of CA10 and CA50 calculated by using multiple regression of operating parameters at 1900RPM, 95% load, AFR13 and ignition timing at -35 aTDC

Figure 6.16 show comparison of the distribution of CA10 and CA50 by using equations (6.4) - (6.7), which used coefficients as a function of the ignition timing for 2,000 random selections. Reasonable distributions were predicted from the universal cyclic variation model. Most operating conditions showed differences in the location of the PDF less than 2 CA degrees and the largest difference was about 10 CA degrees.

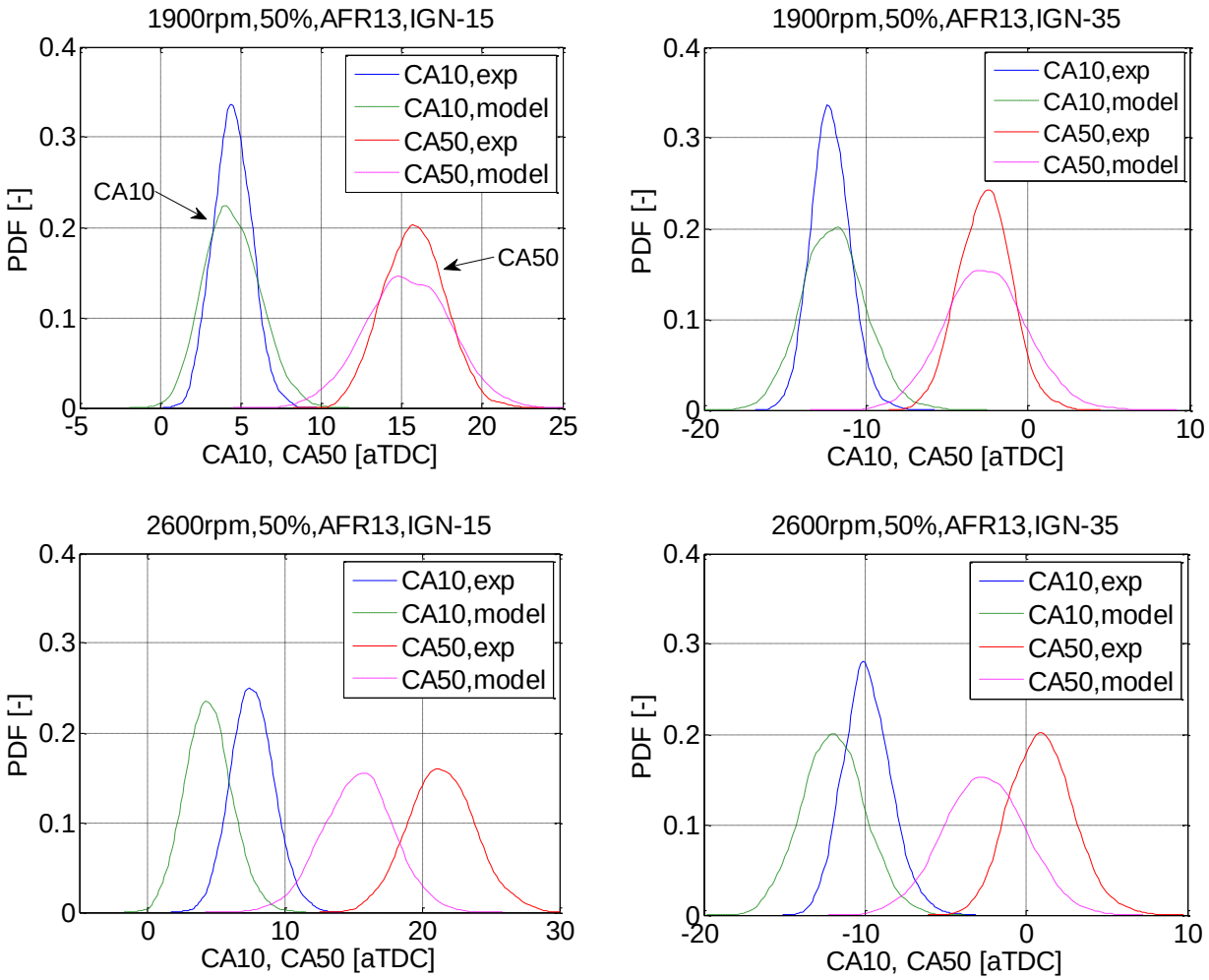

Figure 6.16 PDF of CA10 and CA50 comparison between experiment and the cyclic variation model predicted results

Chapter 7 Knock Model

7.1 Knock Onset Model

Two different knock onset models are compared: an ignition-integral model and the direct integration of a reduced chemical kinetic mechanism. The ignition delay of the ignition-integral model was calculated by using both a simple empirical correlation and a lookup table of ignition delays pre-computed using the reduced mechanism. The cyclic variation model discussed in Chapter 6 was coupled with the knock models to calculate the distribution of the knock and compared with the experimental results.

7.1.1 Knock integral method

The simplest method to predict the onset of knock is the knock-integral model introduced by Livengood and Wu [46]. This model is used widely for predicting the timing of knock with reasonable accuracy [48, 82-84]. The knock integral shown in equation (7.1) relies on the (time-varying) ignition delay for the current thermodynamic state of the end gas mixture. Two different methods were investigated to calculate ignition delay, τ_{ig}.

$$\int_{t=0}^{t_i} \frac{1}{\tau_{ig}} dt = 1 \tag{7.1}$$

7.1.1.1 Correlation-based ignition delay calculation

A correlation for ignition delay method was suggested by Douaud and Eyzat [47]. The correlation for τ_{ig} is given by

$$\tau_{ig} = A\left(\frac{ON}{100}\right)^{m} p^{n} \exp\left(\frac{B}{T}\right) \tag{7.2}$$

where τ_{ig} is in [ms], the pre-exponential A = 17.68, the pressure exponent, n = -1.7 for pressure in [atm], the Arrhenius constant B = 3800 for temperature in [K], ON is the octane number of the fuel, which was 85 for the experiments and the octane number exponent, m = 3.402 was used.

The ignition delay calculated by the correlation-based method is plotted in Figure 7.1 as solid lines as a function of inverse temperature for a range of pressure. Ignition delay at a constant pressure is only a function of temperature.

7.1.1.2 Lookup table ignition delay calculation

The second method used for calculating the ignition delay of the end gas was a lookup table approach using the results of a reduced kinetic calculation. The ERC-PRF kinetic mechanism[5], which includes 155 reactions and 45 species, was used to calculate the ignition delay of a constant pressure reactor over a range of temperature (500 < T < 1300 K) and pressure (1 < p < 70 bar). The ignition delay data were compiled in a lookup table, and for each step in the numerical integration of the knock integral, a value of τ_{ig} was interpolated from the table. This lookup table method was introduced to better account for the chemical effects in calculating the ignition delay compared to the simple correlation-based ignition delay.

The ignition delay for the same temperature and pressure range was interpolated from the lookup table and plotted as dotted lines in Figure 7.1. The Negative Temperature Coefficient (NTC) behavior is clearly seen during the intermediate temperature regime. The calculated ignition delay in the intermediate temperature regime (700 < T [K] < 900) using the correlation and the lookup table are reasonably well matched. However, in the high-temperature regime, which is to the left of the separation points depicted by the red solid line, there is a considerable disagreement both in the magnitude and the trend relative to temperature.

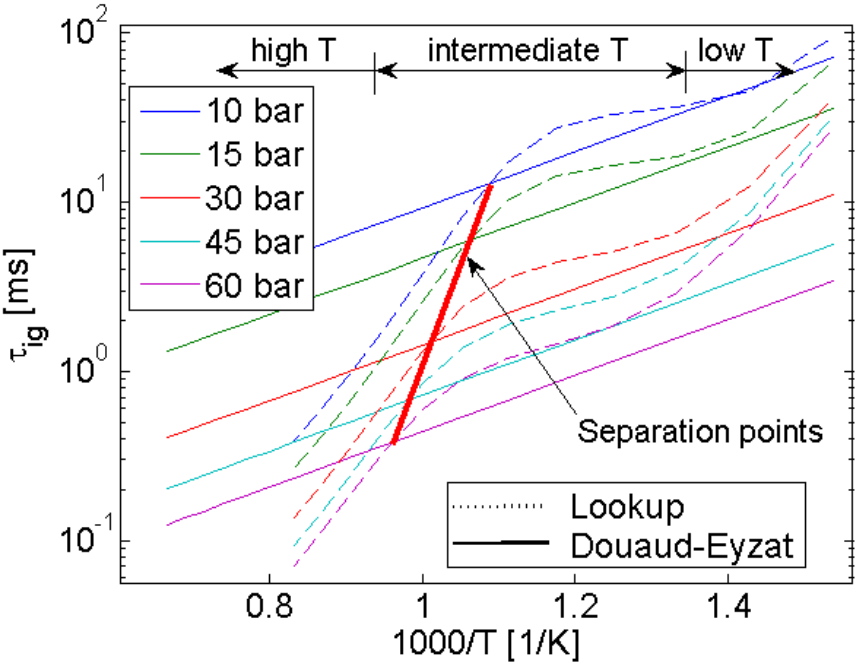

Figure 7.1 Ignition delay calculated by Douaud-Eyzat correlation and the detailed kinetic mechanism

7.1.2 Direct kinetic calculation method

A more comprehensive method of calculating the onset of knock in the end gas was to directly integrate a kinetic mechanism under the end gas thermodynamic conditions. The calculations were performed using the open-source kinetic solver Cantera [85] and the ERC-PRF mechanism. A reactor was defined to have the estimated initial gas composition and temperature, and the measured in-cylinder pressure at IVC. The reactor was effectively compressed by the in-cylinder gases, i.e. the cylinder pressure was imposed on the reactor by adiabatically adjusting its volume. The change in composition and temperature were calculated by the Cantera solver.

The thermodynamic conditions calculated by the direct kinetic model are plotted in Figure 7.2. The volume of the reactor is defined at the IVC timing by arbitrarily setting the mass as unity, and therefore does not have unit. It can be seen that as the cylinder pressure increases the reactor

volume decreases and then auto-ignites. This autoignition of the end-gas can be seen as a rapid increase in both the reactor volume and temperature around 1 crank angle aTDC. To define the ignition time, both the point of maximum temperature rise rate and the point of minimum reactor volume were investigated. Figure 7.3 shows the knock onset calculated by the direct kinetic calculation method using the two different definitions of ignition as a function of the measured knock onset timing. It is seen that the maximum temperature rise rate ignition point lags the point defined by the minimum volume method by approximately 2 crank angle degrees. A non-linear correlation was seen for the maximum temperature rise rate determined knock onset at retarded ignition timing cases. It was found that minimum volume point gave results that were closer to the experimental values, and therefore the minimum reactor volume was taken as the ignition time for all of the data shown below.

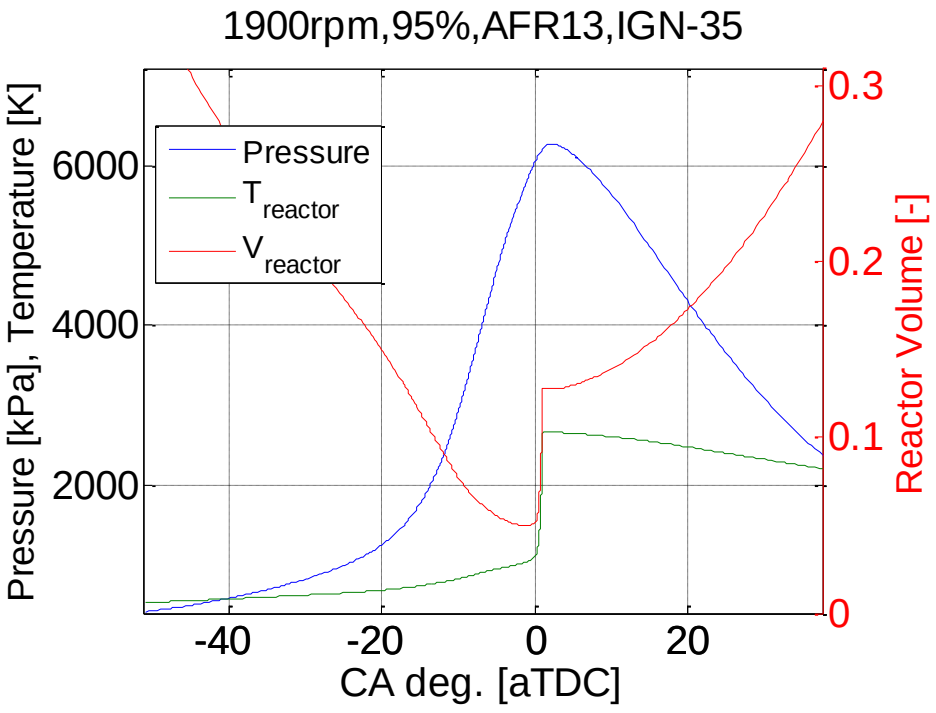

Figure 7.2 Direct end gas kinetic calculation results at 1900 RPM, 95% load, AFR13 and ignition timing -35 aTDC

(a)

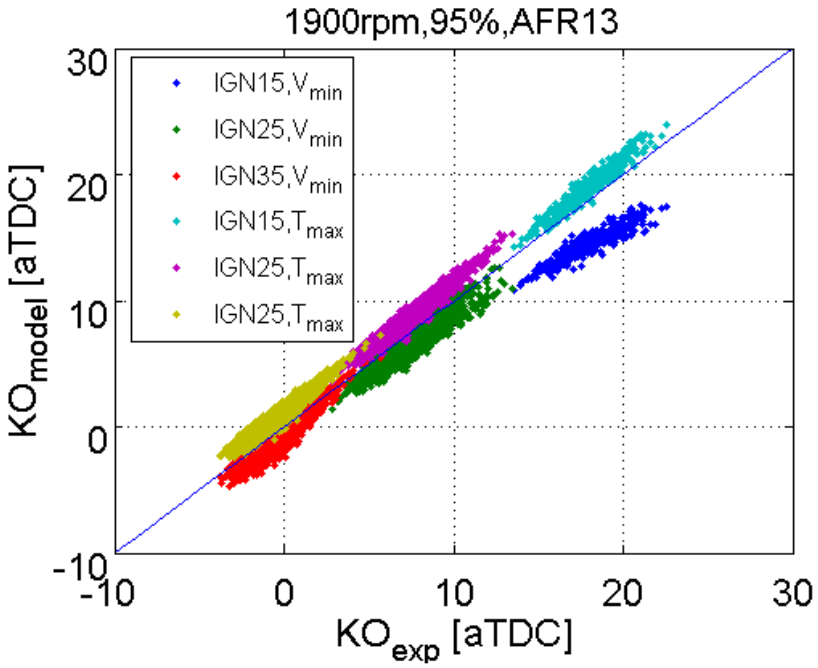

(b)

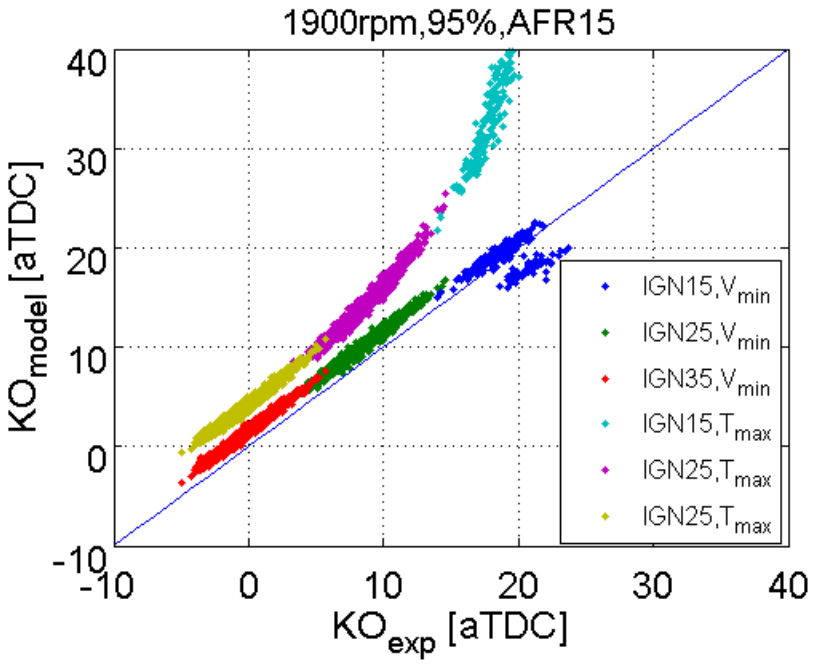

Figure 7.3 The direct end gas kinetic model knock onset defined by the maximum temperature rise rate and the minimum reactor volume.

7.1.3 Knock onset results

A comparison of the knock onset calculated by the model and measured experimentally is shown in Figure 7.4 for the three knock calculation methods discussed above. The experimental knock onset is defined by the method discussed in Chapter 4. Every data point in Figure 7.4 represents a different engine cycle; there are fewer data points for retarded ignition timing cases compared to the advanced timing cases because fewer cycles satisfied the MAPO > 1 [bar] criterion.

In Figure 7.4 it can be seen that the model-predicted knock onset for all three methods shows a good agreement with the experimentally measured knock onset, with a variation of just a few crank angles. The correlation-based knock onset prediction shows good agreement with the measured knock onset and closely matched the 1:1 line. The correlation-based knock-integral method, shown in Figure 7.4 (a), shows slightly more disagreement than the lookup table knock-integral method, especially at the retarded ignition timing cases. The direct kinetic calculation results show a well matched slope of the trend line, but was offset approximately 2 crank angles from the measured data and show more scatter at the retarded ignition timing cases.

Overall, all three methods predicted the knock onset reasonably well. The correlation-based knock-integral method, however, is the most computationally efficient method. The direct kinetic calculation method provides the most detailed thermodynamic conditions for every time step, but was slightly inaccurate in knock prediction. The direct kinetic calculation method, however, is less favorable for a Monte-Carlo simulation because of its relatively large amount of computational resources and time. The good agreement between the correlation-based and lookup table-based knock-integral is somewhat surprising given the large differences shown in Figure 7.1. The reason for this agreement is that the end gas thermodynamic state always stays in the intermediate

temperature regime where the correlation-based and lookup table-based ignition delay show good agreement. In Figure 7.5, the ignition delay trace of the end-gas mixture is plotted for an ensemble averaged in-cylinder pressure at 1900 RPM, 95% load, AFR13 and ignition timing of -35 aTDC for which all 1,000 cycles were found to knock experimentally. As a result, there is no significant advantage of calculating ignition delay by using the detailed chemical kinetic mechanism for knock-integral calculation compared to the relatively simple correlation-based knock integral.

a)

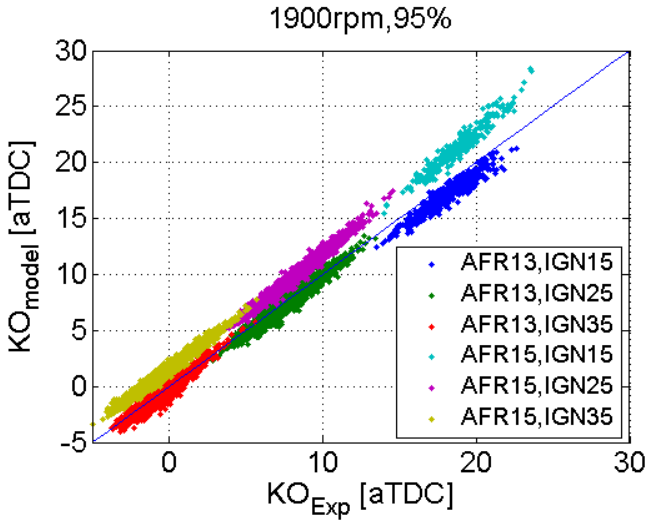

b)

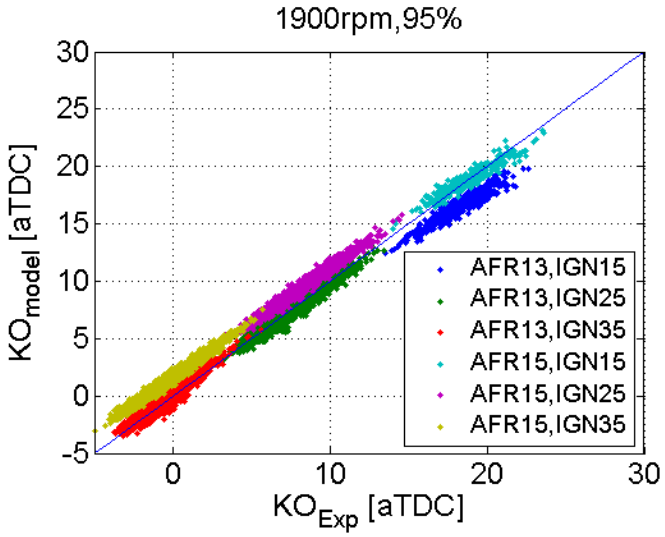

c)

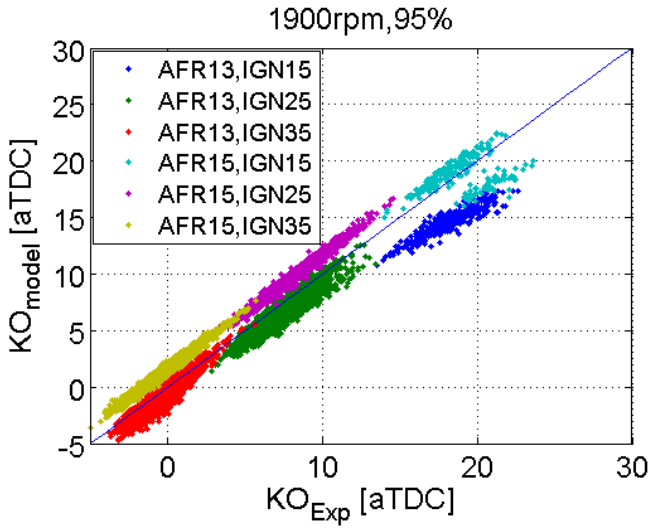

Figure 7.4 Comparison of knock calculation models a) correlation-based knock integral method, b) lookup table knock integral method, c) direct kinetic calculation method.

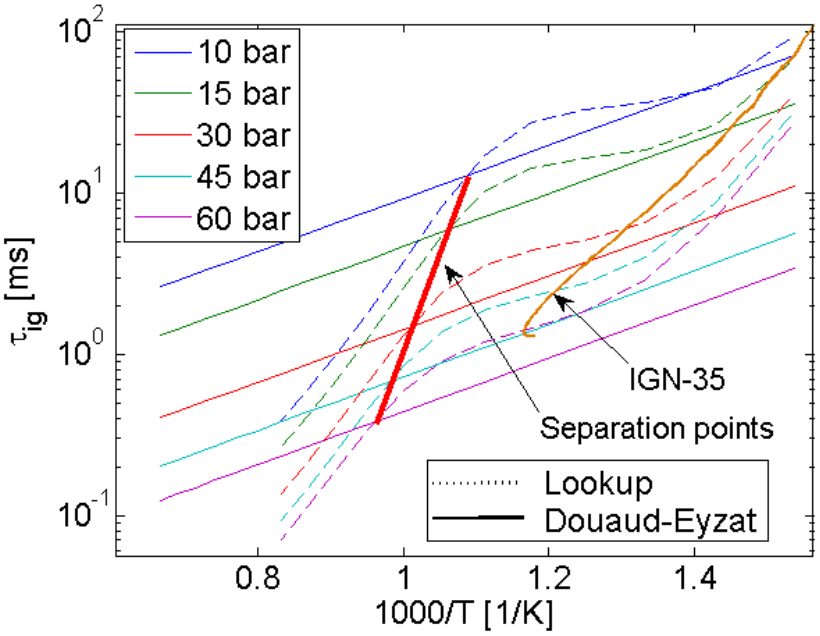

Figure 7.5 Ignition delay trace of the end-gas mixture at 1900 RPM, 95% load, AFR13 and ignition timing -35 aTDC

7.1.4 Monte-Carlo Knock Calculations

The cyclic variation model discussed in Chapter 6 was coupled with the correlation-based knock-integral and direct kinetic calculation models to predict the distribution of knock onset. The probability density function of the knock onset predicted by the correlation-based knock-integral and the direct knock calculation methods are shown in Figure 7.6 along with experimentally measured PDFs. The curve-fitted Wiebe function parameters and its single linear fit was used to randomly generate a set of Wiebe function parameters. Overall, there is a good agreement between the simulated and the measured PDFs for both knock onset calculations over the range of ignition timings. The predicted knock onset determined by the direct knock calculation is seen to precede the measured data by about 2~3 CA degrees. For all ignition timings, the width of the knock onset

distributions are well captured by the model. Convergence of the model-predicted PDF was accomplished with 1,000 randomly selected cycles.

The computational time required for the two Monte-Carlo simulations differed significantly. For the correlation-based knock-integral method, a 3,000-cycle simulation required 40 seconds on a desktop computer, while the direct calculation method required more than 7 hours on the same computer. Given that the accuracy of the two models was comparable, the advantages of using the correlation-based knock-integral method are apparent.

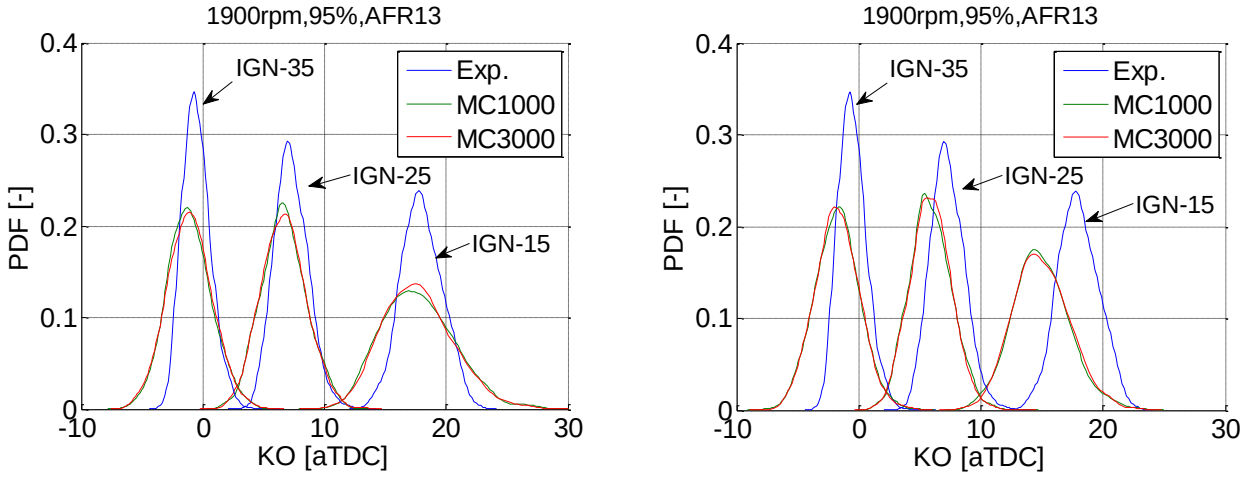

(a) (b)

Figure 7.6 Calculated knock onset results using (a) the correlation-based knock-integral method and (b) direct knock model for different ignition timings at 1900 RPM, 95% load and AFR13. The number of cycles simulated was varied according to the legend.

A coupled knock onset model using the universal cyclic variation and the correlation-based knock-integral models predicted results are compared to Wiebe function random generation from parameters linear fit and measured knock onset in Figure 7.7. It is seen in the Figure 7.7 that the location of the PDF predicted from the universal cyclic variation model differ by 3~5 CA degrees,

which was seen in the Figure 6.15. For all conditions, the width of the knock onset distributions are well captured by the universal cyclic variation model.

(a)

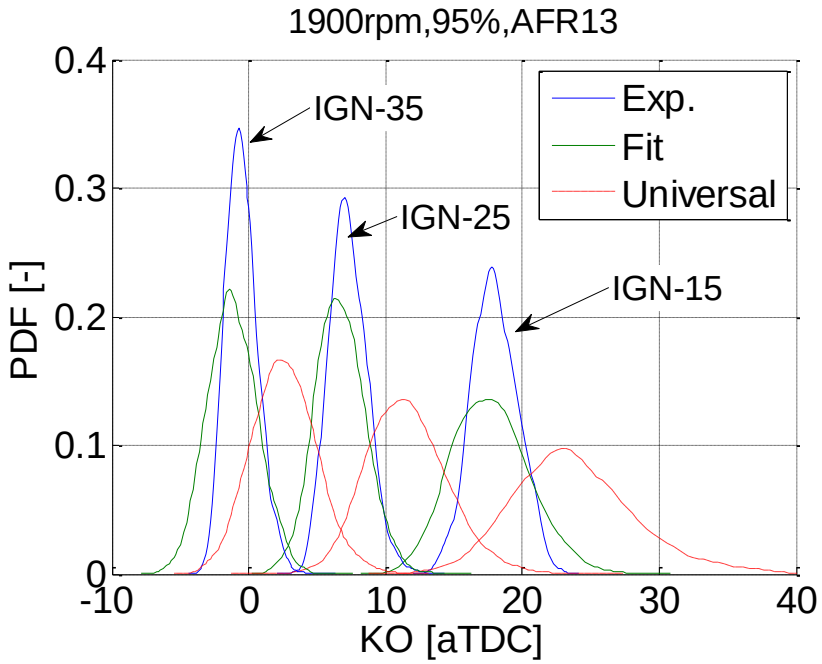

(b)

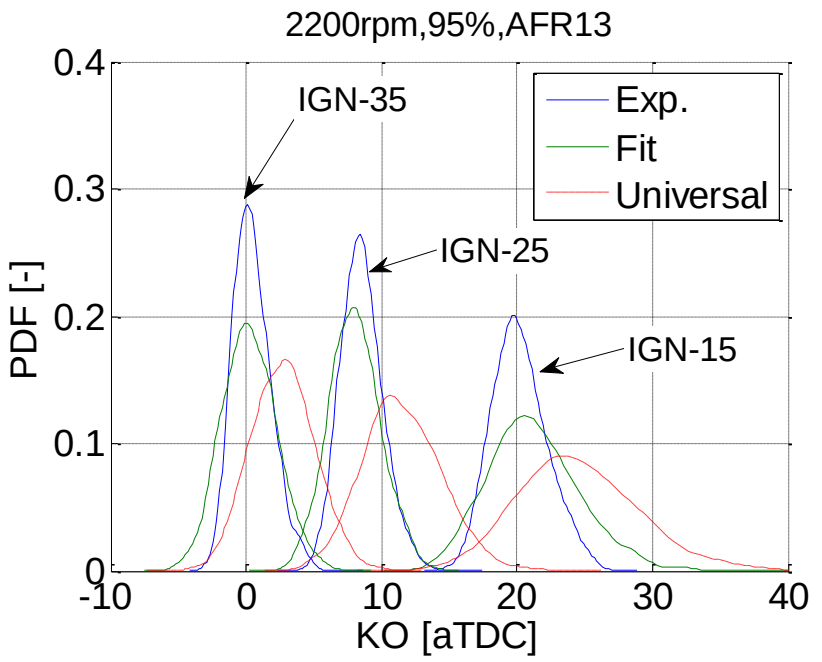

Figure 7.7 Calculated knock onset results using the correlation-based knock-integral method between (a) linear fit and (b) the universal cyclic variation model

7.2 Knock Intensity Model

Knock intensity correlations are investigated: an energy-based and volume expansion-based knock intensity. A stochastic approach of finding the upper-limit knock intensity cycles were investigated to avoid biases in pressure measurement during knock. Volume expansion-based pressure rise based on the blast wave theory and acoustic was investigated for the upper-limit knock intensity cycles to predict the distribution of the knock intensity and compared with the experimental results.

7.2.1 Simple Knock Intensity Correlations and Measurement Limit

One would expect the severity of the autoignition, quantified by measuring the amplitude of pressure oscillation, to be a strong function of the energy that is released at knock onset. Therefore, the simplest knock intensity correlation can be found by comparing the fuel energy available at knock onset to the measured knock intensity. Figure 7.8 (a) shows the correlation between unburned mass fraction at knock onset and the MAPO knock intensity for 5,000 cycles. It is seen in Figure 7.8 (a) that no unique correlation was found between the two parameters. Figure 7.8 (b) shows the PDF of MAPO knock intensity for all of the cycles, which shows close to log-normal distribution. The most probable MAPO knock intensity was about 2.5 bar, 78% cycles fall between 1 and 5 bar MAPO, and the maximum measured knock intensity was about 27 bar. The range of MAPO knock intensity at the unburned mass burn fraction at knock onset 0.25 was about 20 bar. It is clear that the unburned mass fraction at knock onset, which is determined by the accurate knock onset and heat release calculation, cannot predict knock intensity for each individual cycle.

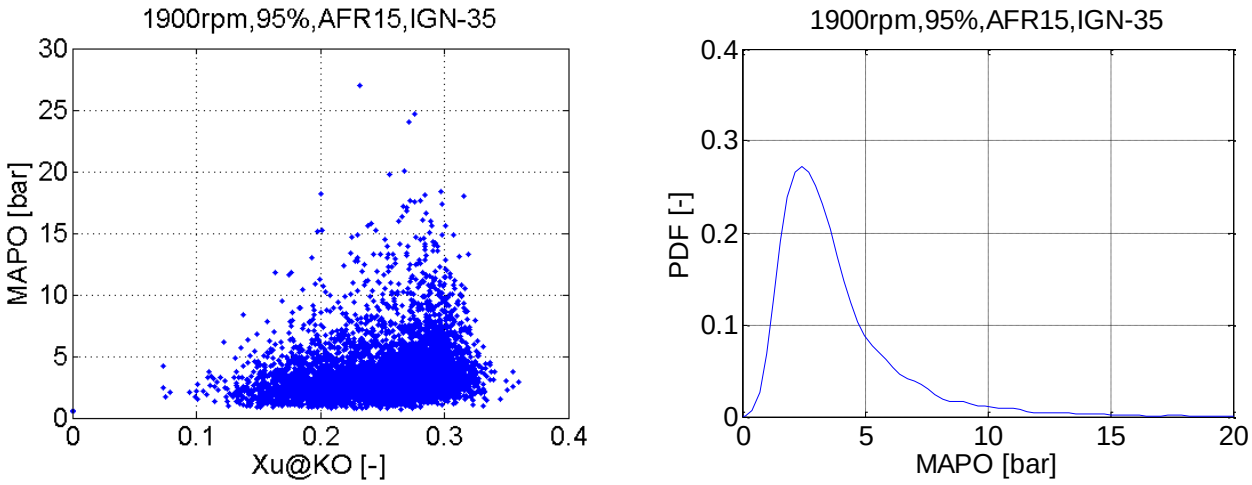

(a) (b)

Figure 7.8 Knock intensity vs. unburned mass fraction at knock onset and PDF of MAPO at 1900RPM, 95% load, AFR15 and ignition timing -35 aTDC

A large range of knock intensity for a similar unburned mass fraction at knock onset could be a result of limitations in the pressure oscillation measurement. By solving the wave equation in a cylindrical coordinates, it can be seen that the pressure field is a combination of different oscillation modes; the majority of the wave energy induced by the autoignition is typically contained in the first circumferential mode. At the center of the circumferential mode, a relatively low pressure oscillation will be measured [20, 22, 23, 84]. Pressure measurements using multiple transducers show that the maximum pressure oscillation was always measured at the transducer location close to the cylinder wall, and the minimum oscillations were captured at the center of the cylinder bore. This implies that the accuracy of measuring the maximum pressure oscillation using a single pressure transducer could be limited because of the randomness of the location of each cycle's hot spot, where the initial autoignition occurs.

Figure 7.9 compares the raw data, low- and high-pass filtered in-cylinder pressure of three different cycles and is similar to Figure 1.3. Cycle #4729, which showed severe knock intensity,

was chosen as a baseline. Cycles #3047 and #3074 were found to have the minimal sum-squared error from spark ignition to knock onset compared to the cycle #4729 from total 5,000 cycles at the same operating condition. It is shown in Figure 7.9 that the in-cylinder pressure development from ignition to knock onset for three cycles are almost identical, while the high-pass filtered data shows significant differences in the pressure oscillations from 1.9 to 20.1 bar. It is a reasonable assumption that the thermodynamic condition at the same crank angle between those cycles will be similar. The thermodynamic conditions at knock onset are listed in Table 7-1, using the thermodynamic engine model and the heat release calculation described in Chapters 3 and 5. The differences shown are in comparison to cycle #4729. The large differences in measured MAPO values for cycles #3047 and #3074 proves that the measured knock intensity values does not depend only on thermodynamic conditions at knock onset. There are 2 possibilities (1) we don't measure correctly, (2) the measurements are correct and we do not understand the physics. We can't be conclusive about which is right.

(a)

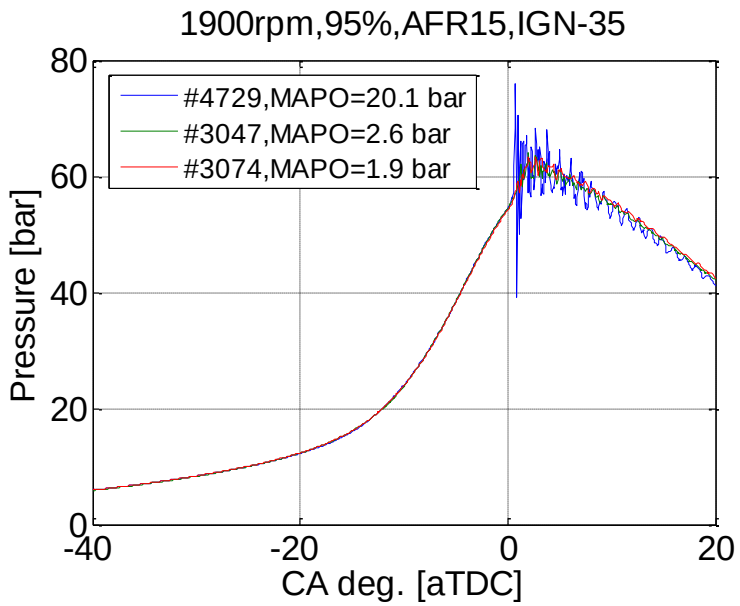

(b)

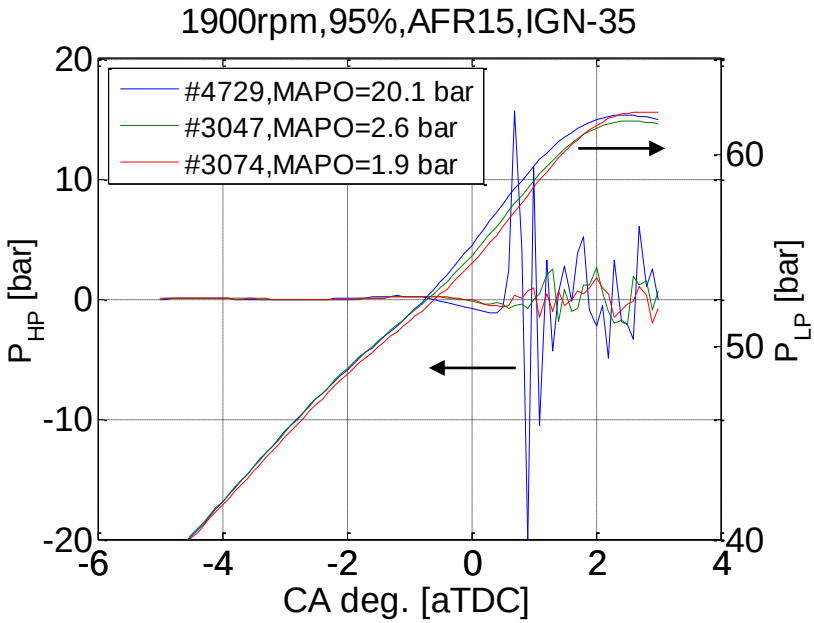

Figure 7.9 In-cylinder pressure comparison (raw, low- and high-pass filtered) between three cycles with similar pressure development at 1900RPM, 95% load, AFR15 and ignition timing -35 aTDC

Table 7-1 Comparison of thermodynamic conditions at knock onset for the same cycles from Figure 7.9

Cycle No.		#4729	#3047	Differences	#3074	Differences
KO	[aTDC]	0.45	0.90	+0.45 CA deg.	0.50	+0.05 CA deg.
MAPO	[bar]	20.09	2.64	-17.45 bar	1.97	18.12 bar
AEPO	[kPa^2]	56.41	57.48	-1.90%	55.59	1.45%
Xu@KO	[-]	0.285	0.262	8.07%	0.287	-0.70%
Vu@KO	[cm^3]	2.98	2.69	9.73%	3.01	-1.01%
Teg@KO	[K]	889.30	889.80	-0.06%	889.80	-0.06%
T_{isen}@KO	[K]	2181.00	2226.10	-2.07%	2162.10	0.87%

7.2.2 Knock Intensity Distribution and Stochastic Approach

A new approach based on the statistical distribution of knock intensity was employed in this work. The highest MAPO cycles for a given unburned mass fraction at knock onset were assumed to capture the full knock intensity, and were used to scale the knock intensity distribution. The distribution of MAPO knock intensity was compared for a number of different ranges of unburned mass fraction at knock onset, see Figure 7.10. To include a similar number of cycles in each bin, the range of unburned mass fraction was selected based on the CDF of the MAPO, instead of dividing unburned mass fraction by a constant number. It is seen in Figure 7.10 (b) that close to a log-normal distribution was found for each bin of the unburned mass fraction at knock onset. The most probable point of each distribution moves in direction of increasing MAPO as the unburned mass fraction at knock onset increases, which result in a smaller peak PDF value at the most probable MAPO of each bin; the low-MAPO end of the distribution does not appear to shift with the unburned mass fraction at knock onset.

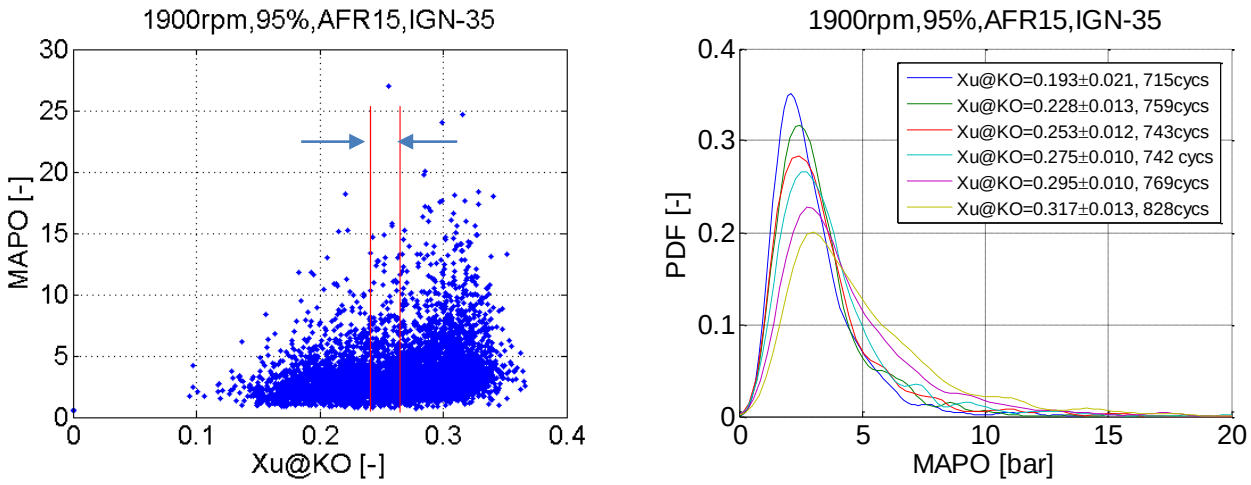

(a) (b)

Figure 7.10 Knock intensity correlation to unburned mass fraction at knock onset and the distribution of MAPO for a range of unburned mass fraction

A simple transformation can be achieved by normalizing each *Xu* bin's knock intensity values by the knock intensity that corresponds to the 95th percentile (KI_{95}). The hope is to make the PDFs of normalized knock intensity self-similar. The normalized distributions are shown in Figure 7.11 for the condition shown in Figure 7.10 (b). It can be seen that the normalized distributions collapse well to a single curve.

To find a universal transformed knock intensity distribution, the same approach was applied for 28 different operating conditions with severe knock, as shown in actual values in Figure 7.12 (a). The knock intensity value ranged up to 20 bar and the maximum value of the PDF varied from 0.25 to 1.75. A simple transformation using the respective KI95 value as a stretch factor was found to transform this large distribution in the MAPO knock intensity PDFs into a nearly self-similar curve, as shown in Figure 7.12 (b). A universal distribution of normalized knock intensity was found by curve-fitting all the transformed knock intensity data using a log-normal distribution. The value of μ and σ were -0.9304 and 0.5322 of the universal distribution plotted as light green in the Figure 7.12 (b).

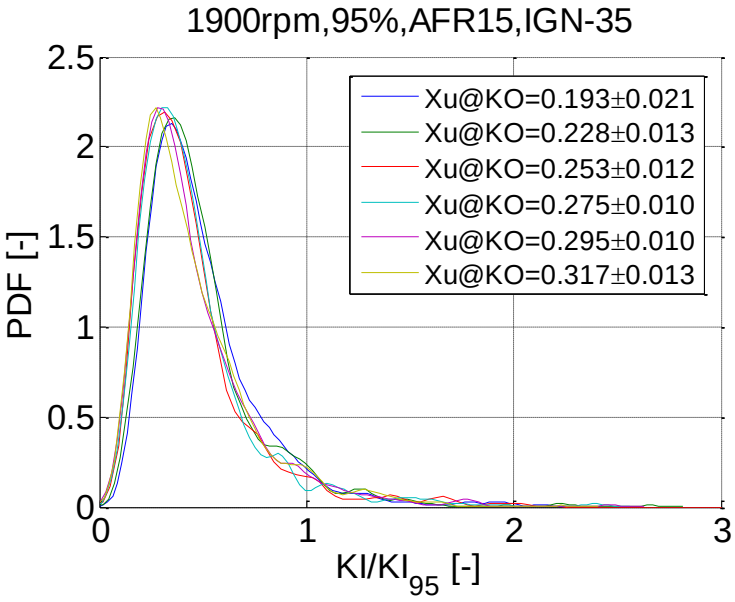

Figure 7.11 Converted PDF of MAPO knock intensity at 1900RPM, 95% load, AFR15 and ignition timing -35 aTDC

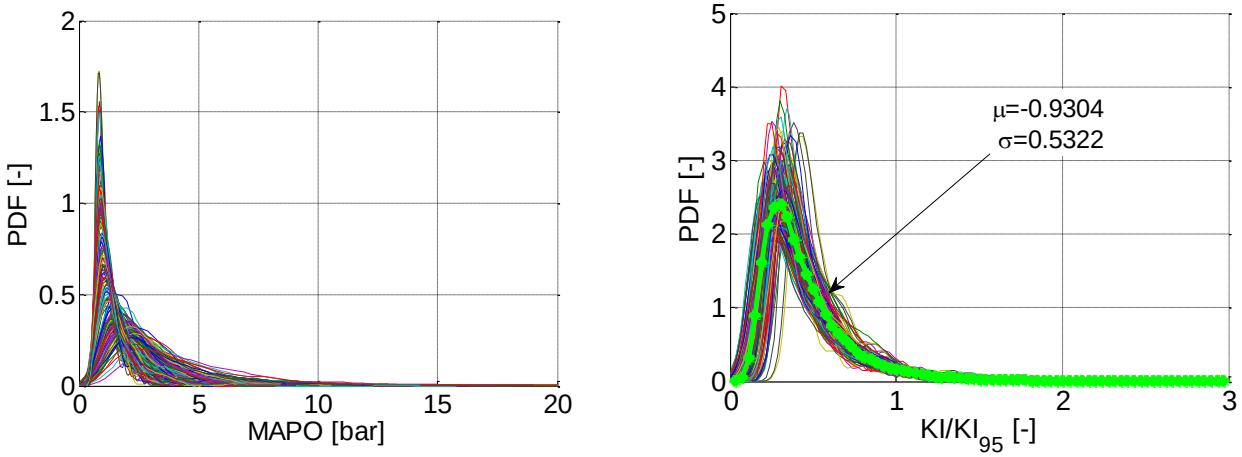

(a) (b)

Figure 7.12 Knock intensity and converted knock intensity distribution of 28 operating conditions and a universal converted knock intensity distribution

Cycles at the upper-limit knock intensity, which corresponds to the KI95 for each bin of the unburned mass fraction at knock onset were identified for different operating conditions. Figure

7.13 shows two different methods of determining the upper-limit knock intensity. First, a relatively simple method of finding 5th largest knock intensity cycle in each bin was selected and compared for a range of operating conditions. The selected cycles are marked as blue open circles in Figure 7.13, which show an unreliable trend due to the randomly distributed knock intensity between each bin. To more reliably find the upper-limit knock intensity cycles, a two-step process was developed. First, all of the cycles were divided into 50 bins based on the unburned mass fraction at knock onset. The cycles that corresponded to the 95th percentile of each bin are shown in Figure 7.13 as a green line. It is seen in the Figure 7.13 that the upper-limit knock intensity includes significant noise due to the large number of bins and the requirement of finding a single cycle from each bin. To reduce the noise in finding the upper-limit knock intensity, a linear regression was performed between unburned mass fraction at knock onset and MAPO knock intensity. The upper-limit knock intensity cycles were determined by finding the minimum differences between this linear correlation and individual cycles in 10 bins based on the unburned mass fraction at knock onset. These closest cycles are shown as the red line in Figure 7.13. It was found that the two-step process determined the upper-limit knock intensity cycles for different operating conditions with better reliability.

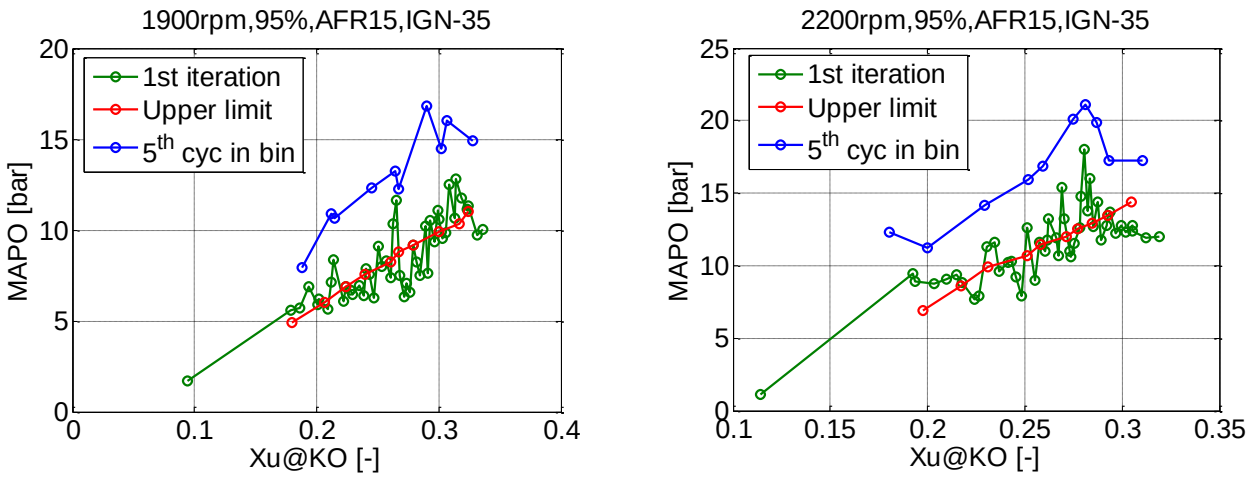

(a) (b)

Figure 7.13 Upper-limit knock intensity determined at 1900 and 2200 rpm, 95% load, AFR15 and ignition timing -35 aTDC

Figure 7.14 (a) shows the correlation between unburned mass fraction at knock onset and MAPO knock intensity of the upper-limit cycles for severe knock cases. A linearly increasing trend for each operating conditions, which was forced by the selection process, is seen in Figure 7.14 (a). The correlation, however, is not unique. Figure 7.14 (b) shows the correlation of the MAPO with the energy available at knock onset, which is found by calculating the unburned fuel mass at each operating condition. For a given engine, this is a more reasonable approach to find a unique correlation to predict knock intensity. The amount of unburned energy at knock onset was calculated using equation (7.3)

$$E_{knock} = \rho_u V_{KO} y_{fu} \eta_c LHV \qquad (7.3)$$

where ρ_u and V_{KO} is the end-gas density and volume at knock onset, y_{fu} is the fuel mass fraction in the end-gas, η_c is the combustion efficiency which is unity for lean and stoichiometric mixtures

but less than unity for rich mixtures, and *LHV* is the fuel's lower heating value. It is shown in Figure 7.14 (b) that the upper-limit knock intensities between operating conditions collapses to several clusters, however, not into a single unique line that can be used to predict the upper-limit knock intensity accurately. Further investigation that involves adding other thermodynamic parameters at knock onset should be performed to find a unique correlation.

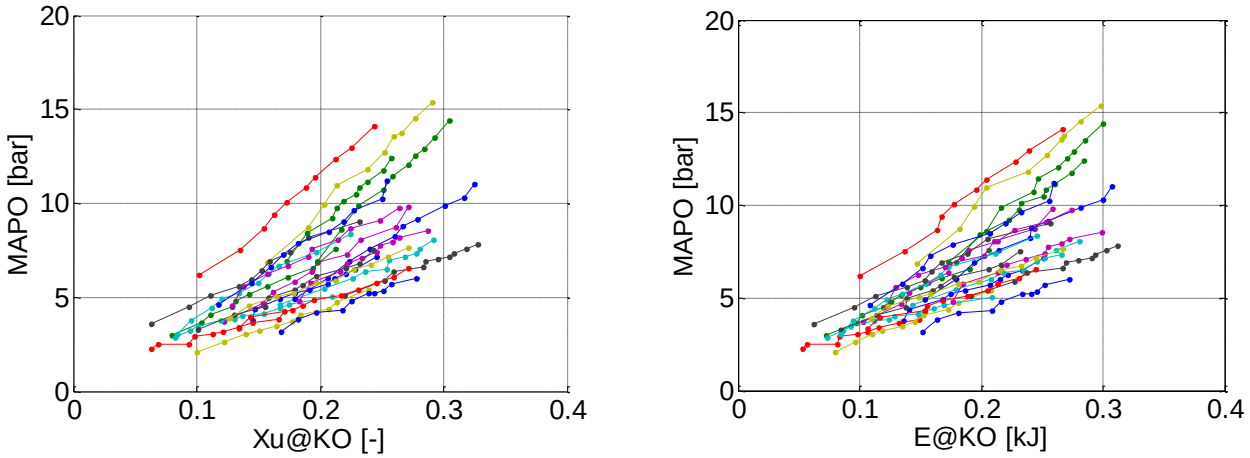

(a) (b)

Figure 7.14 Upper-limit knock intensity cycles and its correlation to (a) unburned mass fraction at knock onset and (b) energy released at knock onset

7.2.3 Knock Intensity Correlations and its Verification to Upper-limit Knock Intensity

Two different knock intensity correlations suggested by Yelvington and Green [39] and Bradley and Kalghatgi [33] were investigated to find a unique correlation for predicting the upper-limit knock intensity. Yelvington and Green's knock intensity correlation compares the ratio of the energy addition by autoignition and volume expansion of the hot-spot to determine a knock limit. Bradley and Kalghatgi's correlation utilizes acoustic theory of pressure increase based on

the relative differences between the spatial distribution of ignition delay and the ignition wave propagation speed.

The energy balance of the autoignition hot spot can be written as equation (7.4) where $\dot{Q}_{ch}$ is the amount of energy that is added to the control volume at the time of knock by autoignition.

$$\mathrm{m}C_v \frac{dT}{dt} = \dot{Q}_{ch} - P\frac{dV}{dt} \tag{7.4}$$

Substituting $\frac{dT}{dt}$ with $\mathrm{mR}\frac{dT}{dt} = \mathrm{P}\frac{dV}{dt} + V\frac{dP}{dt}$ gives,

$$\left(\frac{C_v}{R} + 1\right)\mathrm{P}\frac{dV}{dt} + \frac{C_v}{R}V\frac{dP}{dt} = \dot{Q}_{ch} \tag{7.5}$$

Substituting $\frac{C_v}{R}$ with $\frac{1}{\gamma-1}$ and organize equation (7.5) with respect to $\frac{dP}{dt}$ gives the pressure rise rate as stated in equation (7.6). Note that equation (7.6) is another form of the heat release rate calculation.

$$\frac{dP}{dt} = \frac{\gamma-1}{V_u}\dot{Q}_{ch} - \frac{\gamma P}{V_u}\frac{dV}{dt} \tag{7.6}$$

Yelvington and Green assumed the volumetric expansion rate to be limited by the speed of sound during knocking combustion and determined the value as A^*u_{sound}, where A is a frontal area of the autoignition into the burned mixture. To calculate the volume expansion rate, a simple correlation of $\frac{A}{V} = \frac{1}{L_c}$, where the characteristic length L_C as 0.1 of the size of cylinder bore was used [39]. Substitute volume expansion rate with the characteristic length and divide equation (7.6) by the second term, and one can define

$$\beta = \frac{L_c(\gamma-1)}{\gamma p}\frac{\dot{q}}{u_{sound}} \leq 1 \tag{7.7}$$

where $\dot{q}$ is the volumetric heat release rate.

Figure 7.15 (a) compares the predicted β and MAPO knock intensity at the upper-limit cycles discussed in section 7.2.2. An inverse correlation between the β and MAPO of upper-limit cycles

is shown in Figure 7.15 (a). The value of β is larger than 10, which means that the 1st term in equation (7.6) is about an order of magnitude larger than the 2nd term and the correlation is mostly governed by the energy addition rate and the unburned volume at knock onset. The unburned volume at knock onset was calculated using the ideal gas law and the predicted end-gas temperature and unburned mass fraction at knock onset. The time duration for the autoignition to determine $\dot{q}$ was calculated using the blast wave theory assuming the hot-spot to expand spherically. The calculated time for the autoignition ranged from 2 to 8 μs, which was in the range found from the optical measurement of a gasoline autoignition [86]. However, the accuracy of the predicted volumetric heat release rate using a 0-D model is relatively lower that than using a full-CFD calculation. Also, it is unknown whether assuming the maximum volume expansion rate to be limited at the speed of sound, which was verified to find the viable operating range in an HCCI engine by Yelvington and Green, is valid. The expansion rate here is the material expansion rate as compared to a pressure wave propagation rate.

Figure 7.15 (b) shows the predicted maximum pressure rise using Bradley and Kalghatgi's approach to the upper-limit-knock intensity cycles using equation 2.28 [33]. The value of *r* was determined from the calculated unburned volume at knock onset, assuming a spherical shape and the distance d was determined as $\mathrm{Bore} - 2\mathrm{r}$. The value of σ was determined by calculating the ratio of flame and end-gas temperature from the thermodynamic engine mode. The end-gas temperature was used to predict speed of sound at knock onset. To determine ξ value at knock onset, the autoignition propagation velocity u_a was determined as $\frac{1}{\partial\tau/\partial T} \cdot \frac{1}{\partial T/\partial x}$, where $\frac{\partial T}{\partial x} = -1\left[\frac{K}{mm}\right]$, which was the value Bradley and Kalghatgi used [33]. It is shown in Figure 7.15 (b) that a unique correlation was not found using the approach. The predicted maximum pressure rise values were about an order of magnitude larger than the measured MAPO values. A large

variability of the predicted maximum pressure rise is seen for each operating conditions, which was due to a high noise of the calculated ratio of unburned to burned gas density. The correlation suggested by Bradly and Kalghatgi was investigated to explain developing detonation after the autoignition of a hot-spot. The introduced terms σ and ξ were calculated continuously from the autoignition throughout the whole wave propagation process. In this research, the wave equation was not solved after the autoignition and the accuracy of the spatial distribution and thermodynamic conditions of burned and unburned zones are relatively lower than the full-CFD calculation. Only the thermodynamic conditions at knock onset were determined with high accuracy using a 0-D calculation. Using the thermodynamic conditions at just one time in Bradley and Kalghatgi's correlation is limiting.

$$\frac{\Delta p(t)}{p} = \left[\frac{r\gamma}{d}(\sigma - 1)\left(2\sigma\xi^{-2} + \frac{r}{a}\frac{d\xi^{-1}}{dt}\right)\right]_{t-t_a} \qquad \text{(Equation 2.28)}$$

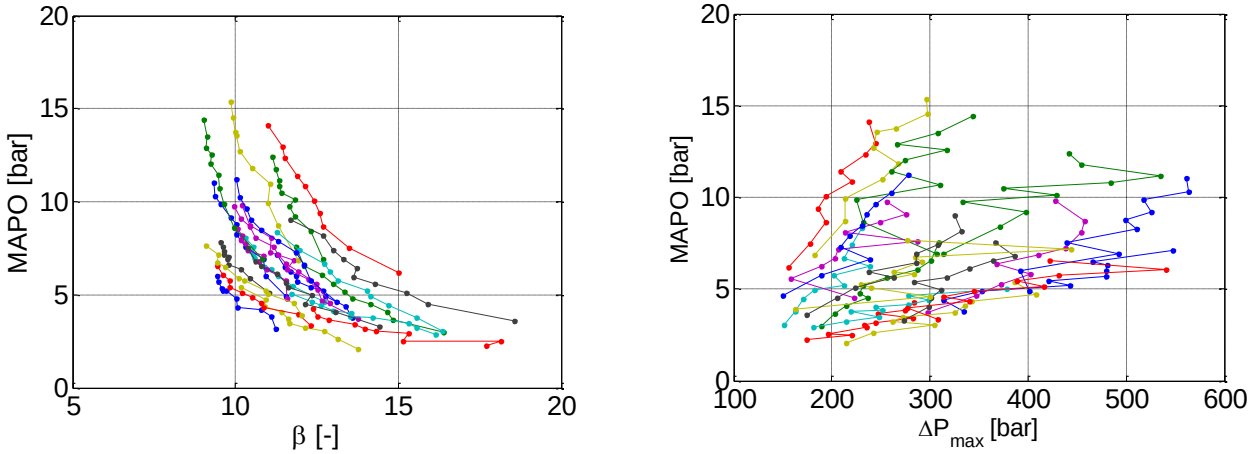

(a) (b)

Figure 7.15 Upper-limit knock intensity correlation using (a) Yelvington and Green and (b) Bradley and Kalghatgi's approach

7.2.4 Volume Expansion-based Upper-Limit Knock Intensity

A new approach of using the blast wave theory and an acoustics-based pressure rise induced by a point source was developed. In this situation, the autoignition zone is taken as the explosion that releases an outwardly propagating pressure (shock) wave, which is considered the 'measured' knock pressure. An analytical expression of a non-dimensional pressure increase due to the autoignition of a hot-spot was developed to find a universal correlation of the upper-limit knock intensity. For an explosion blast wave, one can write

$$\mathrm{r} = \eta_0 \left(\frac{E}{\rho_0}\right)^{1/5} t^{2/5} \tag{7.8}$$

where r is the expanding shock radius, E is the energy release by the explosion, ρ_0 is the ambient density ahead of the shock, t is time and η_0 is a specific heat ratio of air. This can be arranged to solve for time as

$$\mathrm{t} = \left(\frac{R}{\eta_0}\right)^{5/2} \left(\frac{E}{\rho_0}\right)^{-1/2} \tag{7.9}$$

Also for a spherically expanding volume, V, one can find

$$\frac{d^2V}{dt^2} = 4\pi \left(2r \left(\frac{dr}{dt}\right)^2 + r^2 \frac{d^2r}{dt^2}\right) \tag{7.10}$$

where r is the sphere's radius. Consider now the volume enclosed by the expanding spherical shock wave from an explosion. The volumetric expansion rate is found from the derivatives of r with respect to time, which follows from the relations given in equation (7.8) and (7.9) as

$$\frac{dr}{dt} = \frac{2}{5} \eta_0^{5/2} \left(\frac{E}{\rho_0}\right)^{1/2} r^{-3/2} \tag{7.11}$$

and

$$\frac{d^2r}{dt^2} = -\frac{3}{5}\eta_0^{5/2}\left(\frac{E}{\rho_0}\right)^{\frac{1}{2}} r^{-\frac{5}{2}}\frac{dr}{dt} \tag{7.12}$$

By combining the two terms in equation (7.10) for the expanding shock, one finds

$$\frac{d^2V}{dt^2} = 4\pi\left(2r\left(\frac{dr}{dt}\right)^2\right)\left[1-\frac{3}{4}\right] = \pi\left(2r\left(\frac{dr}{dt}\right)^2\right) \tag{7.13}$$

From simple acoustics, the pressure rise, ΔP, associated with a point source expanding volume when measured a distance d away from the source is [38]

$$\Delta P = \frac{\rho}{4\pi d}\left|\frac{d}{dt}\frac{dV}{dt}\right| = \frac{\rho}{4\pi d}\frac{d^2V}{dt^2} \tag{7.14}$$

Substituting equation (7.13) into (7.14) and using (7.11) gives,

$$\Delta P = \frac{\rho}{4\pi d}\left[2r\left(\frac{2}{5}\eta_0^{5/2}\left(\frac{E}{\rho_0}\right)^{1/2} r^{-3/2}\right)^2\right] = \frac{2\eta_0^5 E}{25 d * r^2} \tag{7.15}$$

One can find R and E in terms of the unburned volume at knock onset, V_{KO}, using

$$E = \rho_u V_{KO} y_{fu} \eta_c LHV \tag{7.16}$$

$$r = \left(\frac{3}{4\pi}\right)^{1/3} V_{KO}^{1/3} \tag{7.17}$$

where y_{fu} is the unburned fuel mass fraction in the end gas, η_c is the combustion efficiency which is unity for lean and stoichiometric mixtures but less than unity for rich mixtures, and LHV is the fuel's lower heating value. Combining the relations in equations (7.16) and (7.17) into the pressure rise expression in equation (7.15) one gets

$$\Delta P = \frac{2\eta_0^5 \rho_u V_{KO} y_{fu} \eta_c LHV}{25 d\left(\frac{3}{4\pi}\right)^{2/3} V_{KO}^{2/3}} = \frac{2}{25}\left(\frac{3}{4\pi}\right)^{-2/3} \eta_0^5 \rho_u y_{fu} \eta_c LHV \frac{V_{KO}^{1/3}}{d} \tag{7.18}$$

or in terms of *r* as

$$\Delta P = \frac{2}{25}\left(\frac{4\pi}{3}\right)\eta_0^5 \rho_u y_{fu} \eta_c LHV \frac{r}{d} = \hat{p}\frac{r}{d} \qquad (7.19)$$

where $\hat{p} = \frac{2}{25}\left(\frac{4\pi}{3}\right)\eta_0^5 \rho_u y_{fu} \eta_c LHV$ has units of pressure. It should be noted that the explosion theory is verified for the expansion of product from an explosion measured at distances in the unit of miles instead of an explosion and its expansion in the engine which is a relatively small scale. The physical link between a point explosion and the expanding shock wave and the autoignition event in the engine is admittedly not very strong.

Figure 7.16 shows the non-dimensional upper-limit knock intensity correlation between MAPO/$\hat{p}$ and *r/d*. The effect of including and excluding η_c is compared in Figure 7.16 (a) and (b); no significant advantage of using the η_c term is seen. The pressure was non-dimensionalized by finding the ratio between MAPO knock intensity and predicted pressure $\hat{p}$, using equation (7.19), to $\frac{r}{d}$, which is a ratio between the size of the autoignition hot spot to the distance between the hot-spot to the pressure transducer. The distance between the autoignition hot-spot to the pressure transducer was defined as $bore - 2 \times r$, assuming the maximum pressure oscillation would be measured when the location of hot-spot is opposite the pressure transducer location [20, 22]. It is shown in Figure 7.16 that a unique correlation is not found from the non-dimensional upper-limit knock intensity comparison. Compared to a simple energy-based knock intensity correlation shown in Figure 7.14, almost the same range of the deviation of the knock intensity was found from the non-dimensional upper-limit knock intensity correlation.

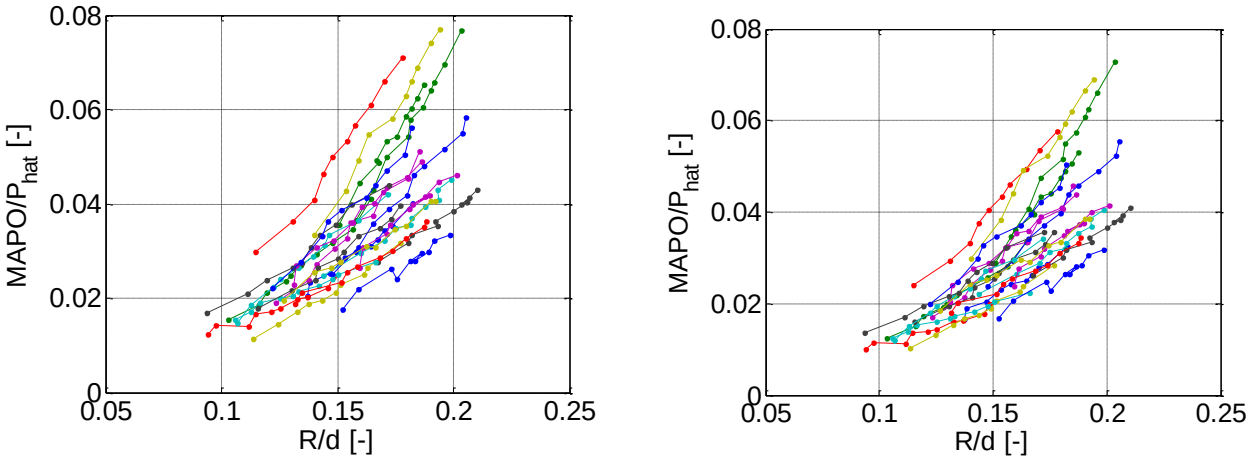

(a) with η_c (b) without η_c

Figure 7.16 Non-dimensional upper-limit knock intensity correlation

Figure 7.17 shows the upper-limit knock intensity correlation calculated by using equation (7.19). It is seen in Figure 7.17 that a much better correlation was found between predicted pressure rise and the measured knock intensity. The deviation of MAPO values at the medium range of the predicted pressure rise was about 3 bar, smaller than 7 bar, which was found for the simple energy-based knock intensity correlation seen in Figure 7.14. No significant advantage of using the η_c was found and the correlation without η_c showed a better collapse to a single line.

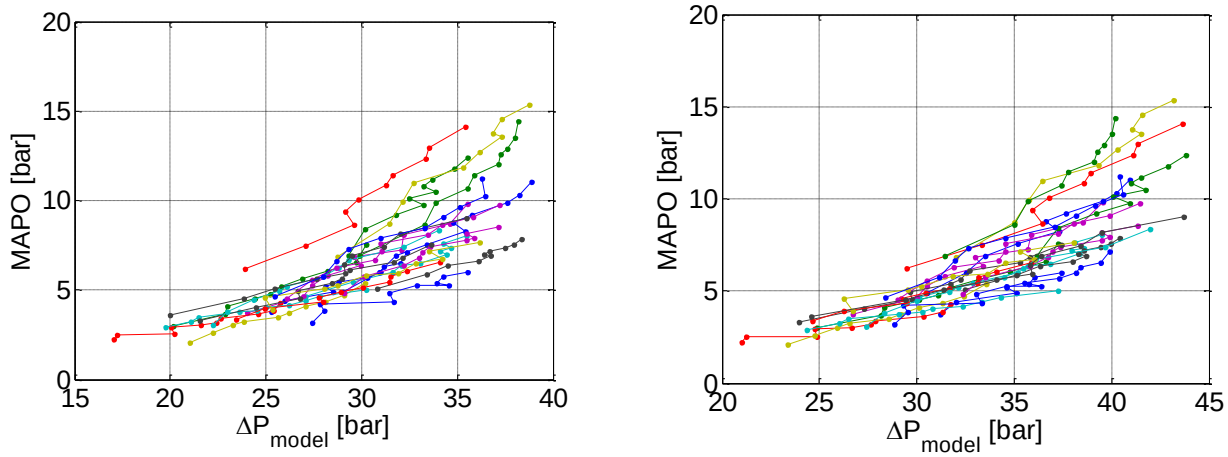

(a) with η_c (b) without η_c

Figure 7.17 Upper-limit knock intensity correlation using volume expansion based approach

The predicted knock intensity, ΔP_{model}, seen in Figure 7.17 (b) was used to develop a correlation for the measured upper-limit knock intensity. Based on the assumption that no knock corresponds to an autoignition hot-spot radius of zero, the correlation was forced to be zero when the predicted ΔP_{model} value is zero. The correlation found to predict upper-limit knock intensity is stated in equation (7.20), and the calculated standard deviation of the correlation was 0.856. Figure 7.18 shows the predicted and measured upper-limit knock intensity and its correlation calculated using equation (7.20).

$$\text{MAPO} = 0.000256 * \Delta P^3 - 0.0086 * \Delta P^2 + 0.1819 * \Delta \text{P} \qquad (7.20)$$

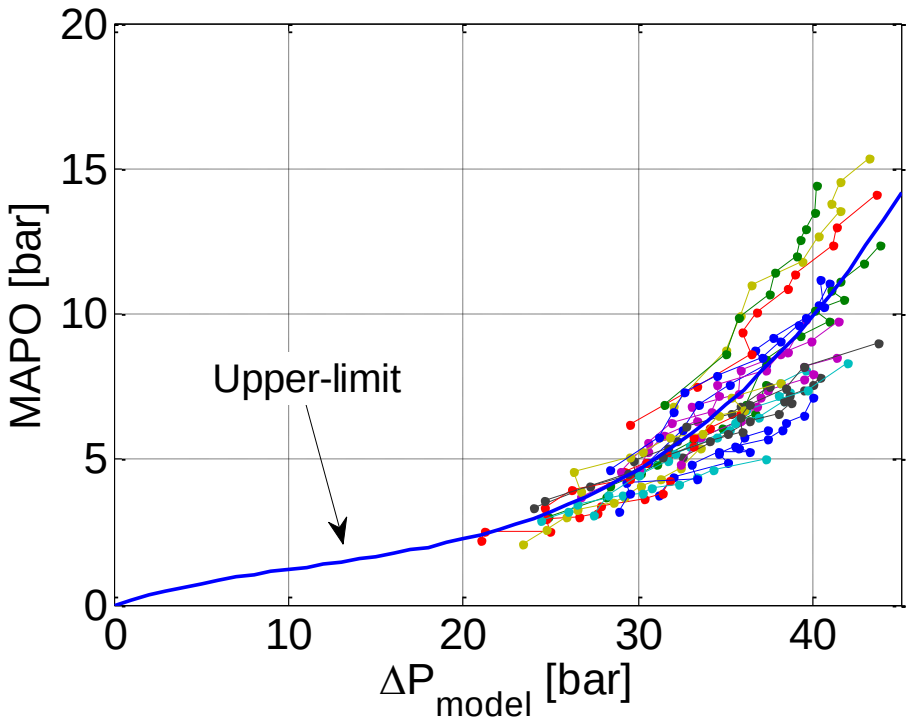

Figure 7.18 Predicted upper-limit knock intensity and its correlation to measured knock intensity for 28 severe knock conditions

7.2.5 Predicted Knock Intensity Distribution

The randomly generated in-cylinder pressure using the universal cyclic variation model will be coupled to knock onset model to determine thermodynamic conditions at knock onset. The data will be used in the knock intensity model to predict ΔP_{model}, and the correlation seen in equation (7.20) will be used to determine upper-limit knock intensities. The universal distribution of normalized knock intensity distribution will be used to randomly calculate knock intensity values.

Figure 7.19 shows predicted upper-limit knock intensity and its PDF compared to the experimental result. The universal cyclic variation model discussed in section 6.3 was used to randomly generate a set of 1,000 Wiebe function parameters to calculate in-cylinder pressure, end-gas temperature and mass burn fraction using the thermodynamic engine model. The knock onset model using a correlation-based ignition delay and the knock integral method, discussed in section 7.1.1.1, was used to determine knock onset of each cycle. The thermodynamic conditions at knock onset were determined and used in the knock intensity model to calculate pressure rise ΔP_{model}, using equation (7.19). The predicted upper-limit knock intensities from the coupled models are plotted as red dots in Figure 7.19 (a). The upper-limit cycles determined as discussed in section 7.2.2 from the experimental data are marked as green open circles in Figure 7.19 (a). It is shown in Figure 7.19 (a) that the range of the unburned mass fraction at knock onset predicted from the universal cyclic variation model matches reasonably well to the experimental result. The PDF of knock intensity was generated using the determined upper-limit knock intensity and the universal distribution of the normalized knock intensity seen in Figure 7.12 (b). The upper-limit knock intensity value was randomly selected for 2,000 sub-cycles from the predicted upper-limit knock intensity and combined with randomly generated normalized knock intensity value using *lognpdf*

function in MATLAB using μ and σ value seen in Figure 7.12 (b). The predicted knock intensity result using the same process of randomly selecting 2,000 sub-cycles of the normalized knock intensity and the upper-limit determined from the experimental data, which is marked as green dots in Figure 7.19 (a), are shown as green solid line in Figure 7.19 (b). The PDF of MAPO shown in Figure 7.19 (b) is the result of all converted MAPO values at the given operating condition. The predicted PDF of MAPO for both experimentally determined upper-limit and use of the universal cyclic variation and upper-limit knock intensity correlation are well matched with the experimentally measured knock intensity distribution.

(a)

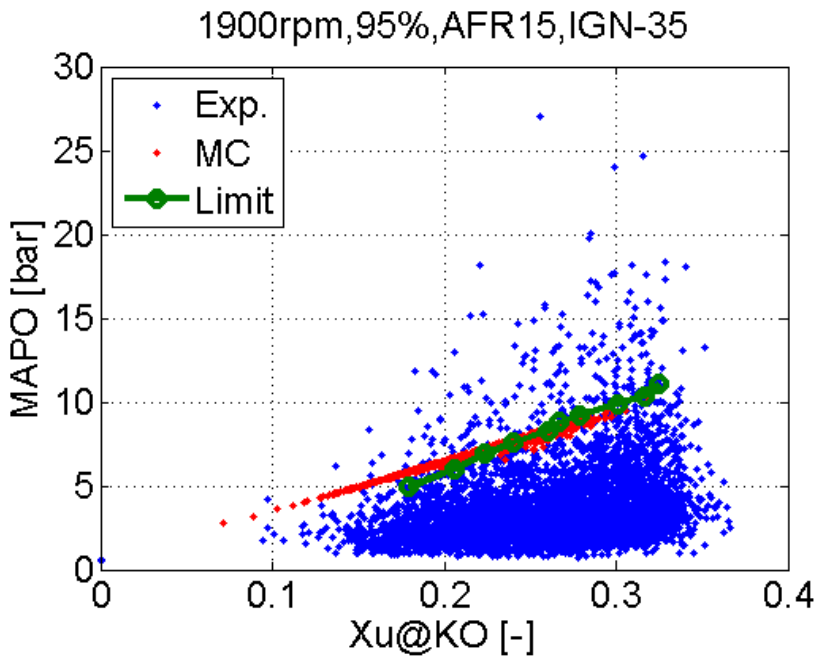

(b)

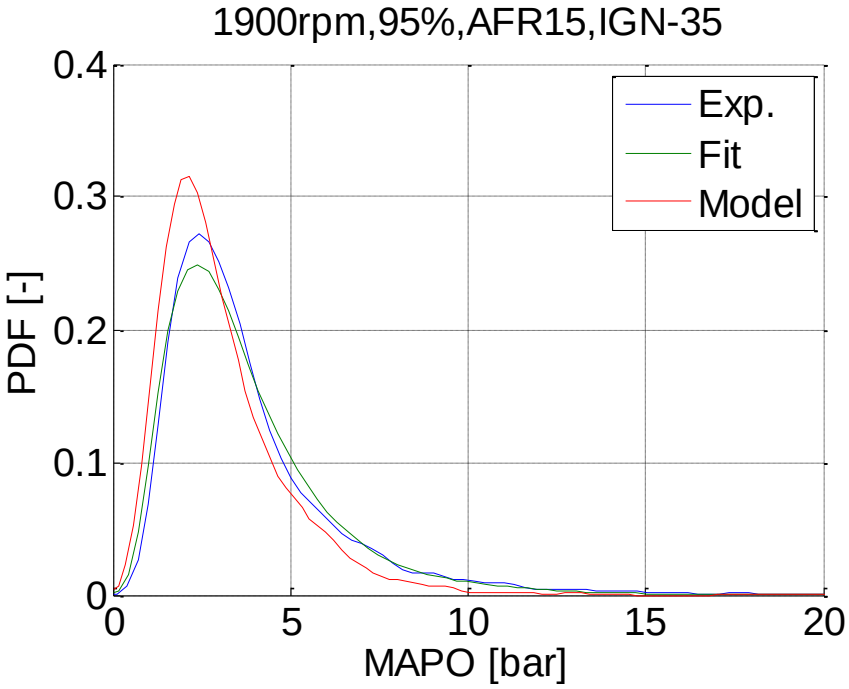

Figure 7.19 (a) Predicted and measured upper-limit knock intensity and (b) PDF of measured (blue) and predicted knock intensity using measured (green) and the cyclic variation model predicted (red) upper-limit at 1900RPM, 95% load, AFR15 and ignition timing -35 aTDC

Figure 7.20 shows the same process and results of predicting the PDF of knock intensity at a different operating condition. Figure 7.20 (a) shows that the range of unburned mass fraction at knock onset predicted by the universal cyclic variation model is higher than the value calculated from the experimental data. As a result, the predicted upper-limit knock intensity using the correlation is higher than the measured upper-limit knock intensity. The predicted PDF of knock intensity using the thermodynamic conditions at knock onset from the universal cyclic variation model predicts higher value of the knock intensity, which is seen in Figure 7.20 (b) as a higher value at the most probable point compared to the PDF from the experimental result.

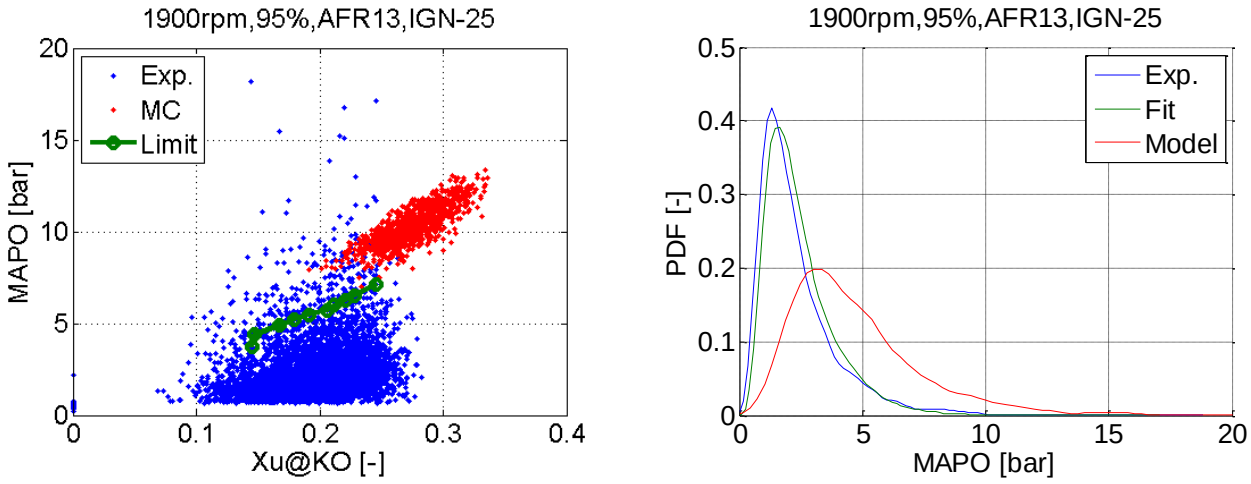

(a) (b)

Figure 7.20 (a) Predicted and measured upper-limit knock intensity and (b) PDF of measured (blue) and predicted knock intensity using measured (green) and the cyclic variation model predicted (red) upper-limit at 1900RPM, 95% load, AFR13 and ignition timing -25 aTDC

The PDF of knock intensity predicted using the universal cyclic variation, thermodynamic engine, knock onset and knock intensity models at four different engine speeds are shown in Figure 7.21. PDF of knock intensity determined directly from the experimental data (blue) and generated by finding the upper-limit from the experimental data (green) and using the universal cyclic

variation model (red) and universal log-normal distribution of the normalized knock intensity were compared in the Figure 7.21. The location and width of the PDF are reasonably well matched and most of the errors were the result of the universal cyclic variation model.

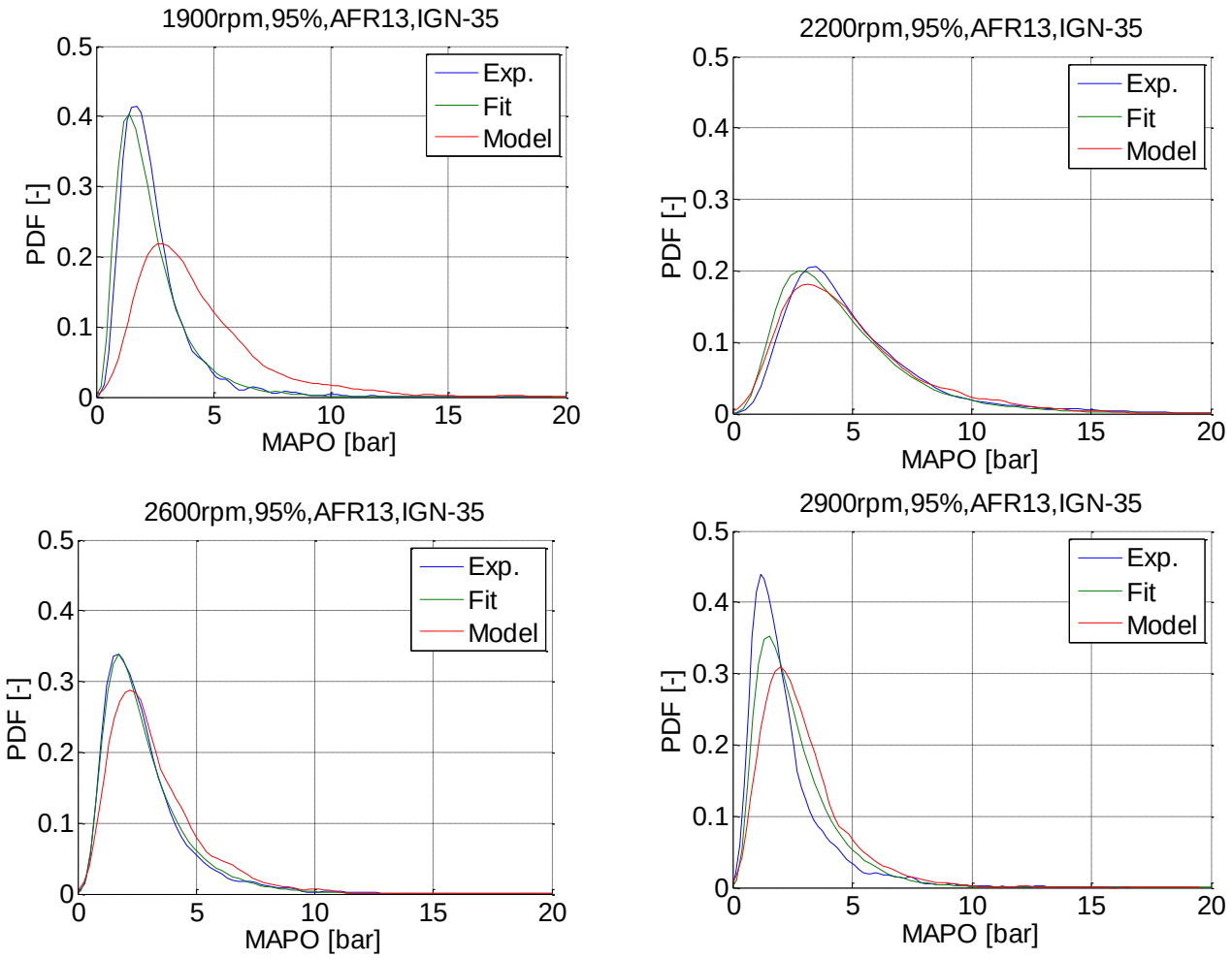

Figure 7.21 PDF of measured (blue) and predicted knock intensity using measured (green) and the cyclic variation model predicted (red) upper-limit

Chapter 8 Conclusions

8.1 Summary

A simple, accurate cyclic variation and coupled knock model were developed to predict the distribution of knock onset and knock intensity. The factors controlling knock onset and knock intensity in spark ignition engine were investigated using experimental data collected from an outboard marine engine. To determine thermodynamic conditions at knock onset accurately, which were used in the knock model, new methods of accurate knock onset determination from the heat release calculation were developed.

A new method of accurate knock onset determination was developed. The method is based on using a new smoothing and median filter to avoid the biases of Butterworth low- and high-pass filter that occur at knock onset. The standard deviation of the noise calculated from the high-pass filtered data prior to knock onset using the new filter was used to set a threshold value of each cycle to determine the most accurate knock onset. The new method detected knock onset of weak, intermediate and severe knock condition with high accuracy compared to TVE or SER methods.

Heat release calculations and the accurate determination of the calculation window size were investigated. For a multi-cylinder engine, the exact amount of fuel and air in any one cylinder is not known with high accuracy, and the most critical parameter for heat release calculation was found to be the end angle of heat release calculation. The in-cylinder pressure calculated using the thermodynamic engine model with the estimated cumulative burn fraction was used to verify the accuracy of the heat release calculation. A window size of fixed duration adjusted to have an end angle determined as 10 crank angle degrees past the point that has the maximum value of pV^1 for the ensemble average pressure cycle was found to be inaccurate for individual cycle analysis. It was found that the end angle needed to be determined for each individual cycle by finding the

minimum error between a Wiebe function and the calculated cumulative heat release; this was verified by re-calculating the in-cylinder pressure.

A simple model that predicts cyclic variation was developed. The model is based on fitting the experimentally measured cumulative rate of heat release to the Wiebe function. It was determined that the Wiebe function parameter *b* did not vary significantly from cycle to cycle and could be fixed with no loss of fidelity, thus only a 3-parameter fit was required. The three Wiebe function parameters showed an inter-relation that needed to be accounted for in the Monte-Carlo model. Coefficients to determine the universal linear fit between the parameters were found. The model required the cumulative distribution function of the ignition angle, from which a value was randomly chosen. The ignition angle was then used to find the combustion duration and Wiebe exponent from linear fits. The distribution around the linear fit was modeled as Gaussian, with the width determined from the experimental spread about the linear fit. The final Monte-Carlo results were found to do a good job of reproducing the cyclic variation of CA10 and CA50.

A simple thermodynamic model was developed to predict end gas temperatures, and the model was coupled to a Monte-Carlo strategy to include the effect of cycle-to-cycle variations. Three different knock calculation methods were evaluated to determine knock onset. The correlation knock-integral approach used a simple four-parameter ignition delay correlation and the Livengood-Wu integral, and was found to be as accurate as the other models and significantly less computationally intensive. The knock-integral method using ignition delay data from a constant-pressure kinetic simulation compiled into a lookup table was also tested. A direct integration of a detailed kinetic mechanism was also investigated, and the results were shown to trend reasonably to the experimental results, but were the least accurate. The direct integration and correlation-based

knock-integral methods were coupled to a Monte-Carlo calculation procedure to predict the distribution of knock onset, and a statistical comparison with experimental results was favorable.

It was proved that the measured knock intensity values does not depend only on the thermodynamic conditions at knock onset that cycles with similar in-cylinder pressure development showed large differences in MAPO values. A stochastic knock intensity model necessarily predict the distribution of knock intensity was developed, and the model was coupled to a Monte-Carlo simulation to predict the distribution of knock intensity. The distribution of knock intensity for a small range of the unburned mass fraction at knock onset can be transformed into a near single distribution using the upper-limit as a normalizing factor. A new approach of calculating the volume expansion rate using the blast wave theory and acoustics that predicts the pressure rise induced by a point source explosion was developed. The upper-limit knock intensity for a range of operating conditions and its correlation to the predicted pressure rise was found. The predicted upper-limit and the universal distribution of the normalized knock intensity distribution were coupled to a Monte-Carlo calculation to predict the distribution of knock intensity and a good match between the experimental results was found.

8.2 Future Work

Future work for this study will include adding more pressure transducers to measure the pressure oscillation at different locations. The bias of the underestimated knock intensity can be avoided from multiple transducer measurements. The time duration between different locations can be used to determine the wave travelling speed and the location of the hot-spot can be identified using triangulation. The wave speed and the location of the hot-spot will provide an accurate estimate of the distance between a point source and measurement location in the pressure rise equation.

The upper-limit knock intensity and its correlation to the measured value can be extended to different engine geometries. The effect of the engine bore size and the shape of engine head could be a critical factor because knock occurs close to TDC timing, when the volume is at the minimum. This will lead to further understandings into the physics of engine knock.

The coefficients to determine the Wiebe function parameters in the cyclic variation model could be extended to different engine geometries. A deeper understanding on the Wiebe function parameter $\Delta\theta$ and its accurate prediction will be critical enhancing the accuracy of the universal cyclic variation model. A correlation between the universal cyclic variation model and the geometries of engine can be used to predict the cyclic variability for any engine geometries.

References

1. Bradley, D., Kalghatgi, G., Golombok, M. and Yeo, J., "Heat release rates due to autoignition, and their relationship to knock intensity in spark ignition engines," Symposium (International) on Combustion, 1996.
2. Rothrock, A.M., Spencer, R.C. and Miller, C.D., "A high-speed motion-picture study of normal combustion, knock and preignition in a spark-ignition engines," NACA Annual Report NACA-TR-704, 1941.
3. Leppard, W.R., "Individual-Cylinder Knock Occurence and Intensity in Multicylinder Engines," SAE Technical Paper 820074, 1982, doi:10.4271/820074.
4. Blunsdon, C.A. and Dent, J.C., "The Simulation of Autoignition and Knock in a Spark Ignition Engine with Disk Geometry," 1994, doi:10.4271/940524.
5. Eckert, P., Kong, S.-C. and Reitz, R.D., "Modeling Autoignition and Engine Knock Under Spark Ignition Conditions," SAE Technical Paper 2003-01-0011, 2003, doi:10.4271/2003-01-0011.
6. Liang, L., Reitz, R.D., Iyer, C.O. and Yi, J., "Modeling Knock in Spark-Ignition Engines Using a G-equation Combustion Model Incorporating Detailed Chemical Kinetics," SAE Technical Paper 2007-01-0165, 2007, doi:10.4271/2007-01-0165.
7. Soltau, J.P., "Cylinder Pressure Variations in Petrol Engines," *Proceedings of the Institution of Mechanical Engineers: Automobile Division* **14**(99-117), 1960, doi:10.1243/PIME_AUTO_1960_000_014_02.
8. Young, M.B., "Cyclic Dispersion in the Homogeneous-Charge Spark-Ignition Engine—A Literature Survey," SAE Technical Paper 810020, 1981, doi:10.4271/810020.
9. Ozdor, N., Dulger, M. and Sher, E., "Cyclic Variability in Spark Ignition Engines A Literature Survey," SAE Technical Paper 940987, 1994, doi:10.4271/940987.
10. Karim, G.A., "An Examination of the Nature of the Random Cyclic Pressure Variations in a Spark-Ignition Engine," *Journal of the Institute of Petroleum* **53**(519):112-120, 1967, doi:0020-3068.
11. Winsor, R.E. and Patterson, D.J., "Mixture Turbulence - A Key to Cyclic Combustion Variation," SAE Technical Paper 10.4271/730086, 1973, doi:10.4271/730086.
12. Brown, A.G., Stone, C.R. and Beckwith, P., "Cycle-by-Cycle Variations in Spark Ignition Engine Combustion - Part I: Flame Speed and Combustion Measurements and a Simplified Turbulent Combustion Model," SAE Technical Paper 960612, 1996, doi:10.4271/960612.
13. Stone, C.R., Brown, A.G. and Beckwith, P., "Cycle-by-Cycle Variations in Spark Ignition Engine Combustion - Part II: Modelling of Flame Kernel Displacements as a Cause of Cycle-by-Cycle Variations," SAE Technical Paper 960613, 1996, doi:10.4271/960613.

14. Kalghatgi, G.T., "Spark Ignition, Early Flame Development and Cyclic Variation in I.C. Engines," SAE Technical Paper 870163, 1987, doi:10.4271/870163.
15. Draper, C.S., "The physical effects of detonation in a closed cylindrical chamber," *National Advisory Committee for Aeronautics*, 1935.
16. Eng, J.A., "Characterization of Pressure Waves in HCCI Combustion," 2002, doi:10.4271/2002-01-2859.
17. Castagné, M., Dumas, J.P., Henriot, S., Lafossas, F.A. et al., "New Knock Localization Methodology for SI Engines," SAE Technical Paper 2003-01-1118, 2003, doi:10.4271/2003-01-1118.
18. Lee, J.-H., Hwang, S.-H., Lim, J.-S., Jeon, D.-C. et al., "A New Knock-Detection Method using Cylinder Pressure, Block Vibration and Sound Pressure Signals from a SI Engine," SAE Technical Paper 981436, 1998, doi:10.4271/981436.
19. Worret, R., Bernhardt, S., Schwarz, F. and Spicher, U., "Application of Different Cylinder Pressure Based Knock Detection Methods in Spark Ignition Engines," SAE Technical Paper 2002-01-1668, 2002, doi:10.4271/2002-01-1668.
20. Brunt, M.F.J., Pond, C.R. and Biundo, J., "Gasoline Engine Knock Analysis using Cylinder Pressure Data," SAE Technical Paper 980896, 1998, doi:10.4271/980896.
21. Scholl, D., Barash, T., Russ, S. and Stockhausen, W., "Spectrogram Analysis of Accelerometer-Based Spark Knock Detection Waveforms," SAE Technical Paper 972020, 1997, doi:10.4271/972020.
22. Bertola, A., Stadler, J., Walter, T., Wolfer, P. et al., "Pressure Sensors - Pressure Indication During Knocking Conditions," Kistler technical report.
23. Hettinger, A. and Kulzer, A., "A New Method to Detect Knocking Zones," *SAE Int. J. Engines* **2**(1):645-665, 2009, doi:10.4271/2009-01-0698.
24. Shahlari, A.J. and Ghandhi, J.B., "A Comparison of Engine Knock Metrics," SAE Technical Paper 2012-32-0007, 2012, doi:10.4271/2012-32-0007.
25. Borg, J.M. and Alkidas, A.C., "Cylinder-pressure-based methods for sensing spark-ignition engine knock," *International journal of vehicle design* **45**(1):222-241, 2007.
26. Sjöberg, M. and Dec, J.E., "Smoothing HCCI Heat-Release Rates Using Partial Fuel Stratification with Two-Stage Ignition Fuels," SAE Technical Paper 2006-01-0629, 2006, doi:10.4271/2006-01-0629.
27. Choi, S., Lim, J., Ki, M., Min, K. et al., "Analysis of Cyclic Variation and the Effect of Fuel Stratification on Combustion Stabilityin a Port Fuel Injection (PFI) CAI Engine," SAE Technical Paper 2009-01-0670, 2009, doi:10.4271/2009-01-0670.
28. Maurya, R.K. and Agarwal, A.K., "Experimental study of combustion and emission characteristics of ethanol fuelled port injected homogeneous charge compression ignition (HCCI) combustion engine," *Applied Energy* **88**(4):1169-1180, 2011.

29. Chun, K.M. and Kim, K.W., "Measurement and analysis of knock in a SI engine using the cylinder pressure and block vibration signals," SAE Technical Paper 940146, 1994, doi:10.4271/940146.
30. Ando, H., Takemura, J. and Koujina, E., "A Knock Anticipating Strategy Basing on the Real-Time Combustion Mode Analysis," SAE Technical Paper 890882, 1989, doi:10.4271/890882.
31. Najt, P.M., "Evaluating Threshold Knock with a Semi-Empirical Model—Initial Results," SAE Technical Paper 872149, 1987, doi:10.4271/872149.
32. Cowart, J.S., Haghgooie, M., Newman, C.E., Davis, G.C. et al., "The Intensity of Knock in an Internal Combustion Engine: An Experimental and Modeling Study," SAE Technical Paper 922327, 1992, doi:10.4271/922327.
33. Bradley, D. and Kalghatgi, G., "Influence of autoignition delay time characteristics of different fuels on pressure waves and knock in reciprocating engines," *Combustion and flame* **156**(12):2307-2318, 2009.
34. Chun, K.M., "Characterization of knock and prediction of its onset in a spark-ignition engine," thesis, Massachusetts Institute of Technology, 1988.
35. Borg, J.M. and Alkidas, A.C., "Investigation of the Effects of Autoignition on the Heat Release Histories of a Knocking SI Engine Using Wiebe Functions," SAE Technical Paper 2008-01-1088, 2008, doi:10.4271/2008-01-1088.
36. Karim, G.A. and Gao, J., "A Predictive Model for Knock in Spark Ignition Engines," SAE Techincal Paper 922366, 1992, doi:10.4271/922366.
37. Richard, S., Bougrine, S., Font, G., Lafossas, F.-A. et al., "On the reduction of a 3D CFD combustion model to build a physical 0D model for simulating heat release, knock and pollutants in si engines," *Oil & Gas Science and Technology-Revue de l'IFP* **64**(3):223-242, 2009, doi:10.2516/ogst/2008055.
38. Hurle, I., Price, R., Sugden, T. and Thomas, A., "Sound emission from open turbulent premixed flames," *Proceedings of the Royal Society of London. Series A. Mathematical and Physical Sciences* **303**(1475):409-427, 1968.
39. Yelvington, P.E. and Green, W.H., "Prediction of the Knock Limit and Viable Operating Range for a Homogeneous-Charge Compression-Ignition (HCCI) Engine," SAE Technical Paper 2003-01-1092, 2003, doi:10.4271/2003-01-1092.
40. Goryntsev, D., Klein, M. and Janicka, J., "Large eddy simulation of cycle-to-cycle variations in a realistic direct injection SI engine," 8th Int. Congress: Engine Combustion Process, Munich, Germany, 2007.
41. Syrimis, M., Shigahara, K. and Assanis, D.N., "Correlation Between Knock Intensity and Heat Transfer Under Light and Heavy Knocking Conditions in a Spark Ignition Engine," SAE Technical Paper 960495, 1996, doi:10.4271/960495.
42. Wayne, W.S., Clark, N.N. and Atkinson, C.M., "Numerical Prediction of Knock in a Bi-Fuel Engine," SAE Technical Paper 982533, 1998, doi:10.4271/982533.
43. Kalghatgi, G.T. and Bradley, D., "Pre-ignition and 'super-knock'in turbo-charged spark-ignition engines," *International Journal of Engine Research* **13**(4):399-414, 2012.

44. Bradley, D., Morley, C., Gu, X.J. and Emerson, D.R., "Amplified Pressure Waves During Autoignition: Relevance to CAI Engines," SAE Technical Paper 2002-01-2868, 2002, doi:10.4271/2002-01-2868.
45. Taylor, G., "The formation of a blast wave by a very intense explosion. I. Theoretical discussion," *Proceedings of the Royal Society of London. Series A, Mathematical and Physical Sciences* 159-174, 1950.
46. Livengood, J.C. and Wu, P.C., "Correlation of Autoignition Phenomena in Internal Combustion Engines and Rapid Compression Machines," Fifth Symposium on Combustion, Combustion in Engines and Combustion Kinetics 1954.
47. Douaud, A.M. and Eyzat, P., "Four-Octane-Number Method for Predicting the Anti-Knock Behavior of Fuels and Engines," SAE Technical Paper 780080, 1978, doi:10.4271/780080.
48. Elmqvist, C., Lindström, F., Ångström, H.-E., Grandin, B. et al., "Optimizing Engine Concepts by Using a Simple Model for Knock Prediction," SAE Technical Paper 2003-01-3123, 2003, doi:10.4271/2003-01-3123.
49. Hu, H. and Keck, J., "Autoignition of Adiabatically Compressed Combustible Gas Mixtures," SAE Technical Paper 872110, 1987, doi:10.4271/872110.
50. Brecq, G. and Le Corre, O., "Modeling of In-cylinder Pressure Oscillations under Knocking Conditions: Introduction to Pressure Envelope Curve," 2005, doi:10.4271/2005-01-1126.
51. di Gaeta, A., Giglio, V., Police, G., Reale, F. et al., "Modeling Pressure Oscillations under Knocking Conditions: A Partial Differential Wave Equation Approach," SAE Technical Paper 2010-01-2185, 2010, doi:10.4271/2010-01-2185.
52. Bozza, F., Fontana, G., Galloni, E. and Torella, E., "3D-1D Analyses of the Turbulent Flow Field, Burning Speed and Knock Occurrence in a Turbocharged SI Engine," SAE Technical Paper 2007-24-0029, 2007, doi:10.4271/2007-24-0029.
53. Teraji, A., Tsuda, T., Noda, T., Kubo, M. et al., "Development of a Novel Flame Propagation Model (UCFM: Universal Coherent Flamelet Model) for SI Engines and Its Application to Knocking Prediction," SAE Technical Paper 2005-01-0199, 2005, doi:10.4271/2005-01-0199.
54. Yavuz, I., Celik, I. and McMillian, M.H., "Knock Prediction in Reciprocating Gas-Engines Using Detailed Chemical Kinetics," SAE Technical Paper 2001-01-1012, 2001, doi:10.4271/2001-01-1012.
55. Lafossas, F.A., Castagne, M., Dumas, J.P. and Henriot, S., "Development and Validation of a Knock Model in Spark Ignition Engines Using a CFD code," SAE Technical Paper 2002-01-2701, 2002, doi:10.4271/2002-01-2701.
56. Lee, Y., Pae, S., Min, K. and Kim, E., "Prediction of knock onset and the autoignition site in spark-ignition engines," *Proceedings of the Institution of Mechanical Engineers, Part D: Journal of Automobile Engineering* **214**(7):751-763, 2000.
57. Heywood, J.B., "Internal Combustion Engine Fundamentals," McGraw-Hill, 0-07-100499-8:1988.

58. Tabaczynski, R.J., Trinker, F.H. and Shannon, B.A., "Further refinement and validation of a turbulent flame propagation model for spark-ignition engines," *Combustion and Flame* **39**(2):111-121, 1980.
59. Grünefeld, G., Beushausen, V., Andresen, P. and Hentschel, W., "A Major Origin of Cyclic Energy Conversion Variations in SI Engines: Cycle-by-Cycle Variations of the Equivalence Ratio and Residual Gas of the Initial Charge," SAE Technical Paper 941880, 1994, doi:10.4271/941880.
60. Johansson, B., Neij, H., Aid,n, M. and Juhlin, G., "Investigations of the Influence of Mixture Preparation on Cyclic Variations in a SI-Engine, Using Laser Induced Fluorescence," SAE Technical Paper 950108, 1995, doi:10.4271/950108.
61. Metghalchi, M. and Keck, J.C., "Burning velocities of mixtures of air with methanol, isooctane, and indolene at high pressure and temperature," *Combustion and flame* **48**(191-210), 1982.
62. Kuroda, H., Nakajima, Y., Sugihara, K., Takagi, Y. et al., "The Fast Burn with Heavy EGR, New Approach for Low NOx and Improved Fuel Economy," SAE Technical Paper 780006, 1978, doi:10.4271/780006.
63. Goryntsev, D., Sadiki, A. and Janicka, J., "Cycle-to-Cycle Variations Based Unsteady Effects on Spray Combustion in Internal Combustion Engines by Using LES," SAE Technical Paper 2012-01-0399, 2012, doi:10.4271/2012-01-0399.
64. Blizard, N.C. and Keck, J.C., "Experimental and Theoretical Investigation of Turbulent Burning Model for Internal Combustion Engines," SAE Technical Paper 740191, 1974, doi:10.4271/740191.
65. Barton, R.K., Lestz, S.S. and Meyer, W.E., "An Empirical Model for Correlating Cycle-by-Cycle Cylinder Gas Motion and Combustion Variations of a Spark Ignition Engine," SAE Technical Paper 710163, 1971, doi:10.4271/710163.
66. Brehob, D.D. and Newman, C.E., "Monte Carlo Simulation of Cycle by Cycle Variability," SAE Technical Paper 922165, 1992, doi:10.4271/922165.
67. Enaux, B., Granet, V., Vermorel, O., Lacour, C. et al., "LES study of cycle-to-cycle variations in a spark ignition engine," *Proceedings of the Combustion Institute* **33**(3115-3122), 2011, doi:10.1016/j.proci.2010.07.038.
68. Goryntsev, D., Sadiki, A., Klein, M. and Janicka, J., "Large eddy simulation based analysis of the effects of cycle-to-cycle variations on air–fuel mixing in realistic DISI IC-engines," *Proceedings of the Combustion Institute* **32**(2):2759-2766, 2009.
69. Goryntsev, D., Stein, O., Klein, M. and Janicka, J., "Characterization of cyclic fluctuations of the in-cylinder flow field of a direct injection si engine using large eddy simulation," 7th Int. Congress: Engine Combustion Process, Munich, Germany, 2005.
70. Goryntsev, D., Sadiki, A. and Janicka, J., "Cycle-to-Cycle Variations Based Unsteady Effects on Spray Combustion in Internal Combustion Engines by Using LES," SAE Technical Paper 2012-01-0399, 2012, doi:10.4271/2012-01-0399.
71. Dai, W., Trigui, N. and Lu, Y., "Modeling of Cyclic Variations in Spark-Ignition Engines," SAE Technical Paper 2000-01-2036, 2000, doi:10.4271/2000-01-2036.

72. Bozza, F., Siano, D. and Torella, E., "Cycle-by-Cycle Analysis, Knock Modeling and Spark-Advance Setting of a "Downsized" Spark-Ignition Turbocharged Engine," *SAE Int. J. Engines* **2**(2):381-389, 2009, doi:10.4271/2009-24-0020.
73. Ghojel, J., "Review of the development and applications of the Wiebe function: a tribute to the contribution of Ivan Wiebe to engine research," *International Journal of Engine Research* **11**(4):297-312, 2010.
74. Eichinger, K.A., "Autoignition Study in a Marine Engine," Master of Science thesis, Mechanical Engineering, University of Wisconsin-Madison, 2010.
75. Erer, K.S., "Adaptive usage of the Butterworth digital filter," *Journal of biomechanics* **40**(13):2934-2943, 2007.
76. Woltring, H.J., "Smoothing and differentiation techniques applied to 3-D data," *Three-dimensional analysis of human movement* 79-99, 1995.
77. Yun, H.J. and Mirsky, W., "Schlieren-Streak Measurements of Instantaneous Exhaust Gas Velocities from a Spark-Ignition Engine," SAE Technical Paper 741015, 1974, doi:10.4271/741015.
78. Ghandhi, J.B., "Heat Release Analysis," Encyclopedia of Automotive Engineering Wiley, 2012.
79. Marvin Jr, C.F., "Combustion time in the engine cylinder and its effect on engine performance," *NACA Technical Report* **276**, 1928.
80. Rassweiler, G.M. and Withrow, L., "Motion Pictures of Engine Flames Correlated with Pressure Cards," SAE Technical Paper 380139, 1938, doi:10.4271/380139.
81. Brunt, M.F.J. and Emtage, A.L., "Evaluation of Burn Rate Routines and Analysis Errors," SAE Technical Paper 970037, 1997, doi:10.4271/970037.
82. Spicher, U., Spiegel, L., Reggelin, B. and Heuser, G., "Investigation into the Applicability of an Optical Fiber Sensor for Knock Detection and Knock Control System," SAE Technical Paper 922370, 1992, doi:10.4271/922370.
83. Ogink, R., "Approximation of Detailed-Chemistry Modeling by a Simplified HCCI Combustion Model," SAE Technical Paper 2005-24-037, 2005, doi:10.4271/2005-24-037.
84. Töpfer, G., Reissing, J., Weimar, H.-J. and Spicher, U., "Optical Investigation of Knocking Location on SI-Engines with Direct-Injection," SAE Technical Paper 2000-01-0252, 2000, doi:10.4271/2000-01-0252.
85. Goodwin, D.G., "An Open-Source, Extensible Software Suite for CVD Process Simulation," Chemical Vapor Deposition XVI and EUROCVD 14. Electrochemical Society, 2003.
86. Katsumata, M., Morikawa, K. and Tanabe, M., "Behavior of Shock Wave and Pressure Wave of SI Knocking with Super Rapid Compression Machine," SAE Technical Paper 2011-01-1875, 2011, doi:10.4271/2011-01-1875.